ISSN 0234-5366

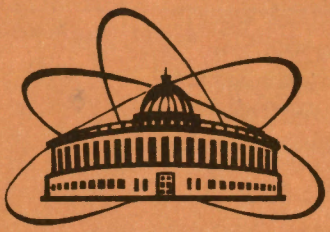

ОБЪЕДИНЕННЫЙ
ИНСТИТУТ
ЯДЕРНЫХ
ИССЛЕДОВАНИЙ

JOINT INSTITUTE
FOR NUCLEAR
RESEARCH

6[57]-92

КРАТКИЕ СООБЩЕНИЯ ОИЯИ

JINR RAPID COMMUNICATIONS

ДУБНА

Объединенный институт ядерных исследований
Joint Institute for Nuclear Research

№6[57]-92

КРАТКИЕ СООБЩЕНИЯ ОИЯИ
JINR RAPID COMMUNICATIONS

сборник
collection

Дубна 1992

ОГЛАВЛЕНИЕ
CONTENTS

Краткие сообщения ОИЯИ № 6[57]-92 *JINR Rapid Communications No.6[57]-92*
УДК 539.12.01.

LEFT-RIGHT COMPONENTS OF BOSONIC FIELD AND ELECTROWEAK THEORY

D.V.Fursaev, V.G.Kadyshevsky

It is shown that the notion of «chirality» in the theory with fundamental mass has a more universal meaning and is applicable not only to fermion but also to boson fields. In the framework of this approach the Higgs sector of the standard model should include apart from the «left» isotopic doublets of scalar fields the «right» scalar singlets as well. Possible experimental consequences of this proposal are shortly discussed.

The investigation has been performed at the Laboratory of Theoretical Physics, JINR.

Левые и правые компоненты бозонного поля и электрослабая теория

Д.В.Фурсаев, В.Г.Кадышевский

Показано, что в теории с фундаментальной массой понятие «киральности» имеет более универсальный смысл и применимо не только к фермионным, но и к бозонным полям. В рамках этого подхода хиггсовский сектор стандартной модели помимо «левых» изотопических дублетов скалярных полей должен включать также «правые» скалярные синглеты. Кратко обсуждаются возможные экспериментальные следствия этого предположения.

Работа выполнена в Лаборатории теоретической физики ОИЯИ.

1. In the Glashow — Salam — Weinberg standard model of electroweak interactions based on the $SU(2)\otimes U(1)$ gauge group, the Higgs scalar, like left and right chiral projections of quarks and leptons, is an $SU(2)$ doublet. However, the notion of chirality doesn't have meaning when applied to boson fields. So the model seems to us to be inconsistent in this point.

We would like to draw attention to the existence of such a formulation of quantum field theory (QFT) when the quantum number «chirality» has a more general and universal meaning than just the eigenvalue of the γ^5 matrix. The new notion of chirality is being spread now not only to fermion fields but to bosonic ones, too. It gives us an opportunity to extend the Higgs sector of the standard model by introducing into consideration separately

«left» H_L and «right» H_R scalar fields. Possible experimental consequences are shortly discussed.

II. The formulation of QFT [1—5] mentioned here contains a new high energy scale M that has the simple geometrical meaning. This is the curvature radius of the De Sitter p-space

$$p_0^2 - \mathbf{p}^2 - p_5^2 = -M^2 \tag{1}$$

replacing the Minkowski p-space in the theory. The low energy-momentum region corresponding to the standard theory is identified with the flat limit of the surface (1)

$$|p_0|, |\mathbf{p}| \ll M, \quad |p_5| \cong M. \tag{2}$$

In the coordinate representation (1) is replaced by a free 5-dimensional equation (the so-called «fundamental equation»)

$$\left[\frac{\partial^2}{\partial x_\mu \partial x^\mu} - \frac{\partial^2}{(\partial x^5)^2} - M^2\right]\varphi(x, x^5) = 0 \tag{3}$$

to be universal for the fields of any tensor type. However, for the spinor ones $\psi(x, x_5)$, besides (3), the 5-dimensional Dirac equation is also fulfilled

$$(\partial_L \Gamma^L + M)\psi(x, x^5) = 0, \tag{4}$$

where Γ^K are five 4×4 matrices with anticommutation relations $\{\Gamma^K, \Gamma^L\} = 2g^{KL}$; $K, L = 0, 1, 2, 3, 5$, diag $g = (+1, -1, -1, -1, -1)$, $\Gamma^5 = i\gamma^5$. All information about the fields $\varphi(x, x^5)$ and $\psi(x, x^5)$ and their interactions is contained in the initial data $(\varphi(x, 0), \partial\varphi/\partial x^5\ (x, 0))$ and $\psi(x, 0)$ for which an adequate Lagrange formalism has been constructed in [1—2]. We consider the corresponding field theory naturally including a new universal constant M as a basis for describing high energy processes under $E \gtrsim M$ beyond the scope of standard model.

When passing to the standard theory as $M \to \infty$, equation (4) turns into

$$(\partial_5 \Gamma^5 + M)\,\psi(x, x^5) = 0 \tag{5}$$

and $\psi(x, x^5)$ reads

$$\psi(x, x^5) = \frac{1 + \gamma^5}{2}\psi(x, 0)\, e^{-iMx^5} + \frac{1 - \gamma^5}{2}\psi(x, 0)\, e^{iMx^5}. \tag{6}$$

Thus, the ordinary «left» and «right» spinor fields corresponding to different eigenvalues of the γ^5 matrix are amplitudes of the phase multipliers $e^{\pm iMx^5}$.

An analogous definition of chiral fields can be introduced in the bosonic case if the asymptotics of solutions of Eq. (5), when $M \to \infty$, is written in the form like (6). For this purpose let us put

$$\begin{aligned} \frac{1}{2}\left(\varphi(x, x^5) + i\frac{\partial}{\partial x^5}\varphi(x, x^5)\right) &\equiv \varphi_1(x, x^5), \\ \frac{1}{2}\left(\varphi(x, x^5) - i\frac{\partial}{\partial x^5}\varphi(x, x^5)\right) &\equiv \varphi_2(x, x^5) \end{aligned} \tag{7}$$

and introduce the doublet $\Phi(x, x^5)^T = (\varphi_1(x, x^5), \varphi_2(x, x^5))$. Then, from (3) it follows that

$$\frac{\partial}{\partial x^5}\Phi(x, x^5) = i\left[\sigma^3\left(M - \frac{\Box}{2M}\right) - i\sigma^2\frac{\Box}{2M}\right]\Phi(x, x^5), \tag{8}$$

where $\Box = \dfrac{\partial^2}{\partial x_\mu \partial x^\mu}$ and σ^2, σ^3 are the Pauli matrices. Thus, if $M \to \infty$,

$$\Phi(x, x^5) = \frac{1 + \sigma^3}{2}\Phi(x, 0)\, e^{-iMx^5} + \frac{1 - \sigma^3}{2}\Phi(x, 0)\, e^{-iMx^5}. \tag{9}$$

One can see, comparing (6) and (9), that σ^3 plays the role of the γ^5 matrix, and the components $\varphi_1(x, x^5)$ and $\varphi_2(x, x^5)$ of the doublet $\Phi(x, x^5)$ can be considered as scalar «left» and «right» fields analogous to left and right chiral projections ψ_L and ψ_R of the spinor field.

III. Following the Glashow — Salam — Weinberg model we place left scalar fields into isotopic doublets and consider right spinors and scalars as isosinglets. It is natural to identify left scalar doublets with Higgs fields and assign to them the proper value of hypercharge $Y = 1$. The occurrence of right scalar singlets is beyond the scope of the standard model. Meanwhile two essentially different cases are possible — charged and uncharged fields.

Let us discuss the properties of charged right singlets marked by H_R^+ and H_R^- according to the sign of their charge. First of all particles of that type could be clearly observed in experiments at electron-positron colliders in the processes $e^+e^- \to \gamma \to H_R^+H_R^-$ or $e^+e^- \to Z_0 \to H_R^+H_R^-$. For example, the cross-section of the first process beyond the threshold is about 1/4 of the section of the process $e^+e^- \to \gamma \to \mu^+\mu^-$ [6]. So far as charged scalar particles were not yet observed, their mass must not be less than half the neutral vector boson mass. Interactions of $H_R^\pm$ with quarks and leptons and also with vector W-bosons appear sufficiently weak as the corresponding interaction terms are absent in the Lagrangian of the theory.

The prediction of uncharged right scalar particles H_R^0 also seems interesting. From the Gell - Mann - Nishidgima relation one can infer that such particles have zero hypercharge and very weakly interact with the other matter. They resemble in this respect right neutrinos ν_R with which they can be coupled in the Yukawa manner

$$f\bar{\nu}_R^c \nu_R H_R^0 + \text{h.c.}, \tag{10}$$

where f is a constant and $\bar{\nu}_R^c$ is the spinor charge conjugated to ν_R. If H_R^0 gets nonzero vacuum expectation value, these interactions give rise to Majorana masses of right neutrinos and lepton number nonconservation. The corresponding Goldstone boson was called the majoron [7]. This circumstance is used in a number of generalizations of the standard electroweak model, in the Glashow work [8], for example, where a suggested model describes both the solar neutrino deficit and the existence of the so-called 17-keV neutrino revealed by Simpson [9].

References

1. Kadyshevsky V.G., Mateev M.D. — Nuovo Cimento, 1985, 87A, No.3, p.324.
2. Chizov M.V. et al. — Nuovo Cimento, 1985, 87A, No.3, p.350; 1985, 87A, No.4, p.373.
3. Kadyshevsky V.G. — JINR Preprint P2-84-753, Dubna, 1984 (in Russian).
4. Ibadov R.M., Kadyshevsky V.G. — JINR Preprint P2-86-830, Dubna, 1986 (in Russian).
5. Kadyshevsky V.G., Fursaev D.V. - Dokl. AN. SSSR, 1989, No.4, p.856.
6. Donoghue J.F., Ling Fong Li. — Phys. Rev., 1979, D9, p.945.
7. Chikashige Y., Mohapatra R.N., Peccei R.D. — Phys.Lett., 1981, 98B, p.265.
8. Glashow S.L. — Preprint HUTP-90/A075.
9. Simpson I.J. — Phys.Rev.Lett., 1985, 54, p.1891.

Received on October 15, 1992.

УДК 539.12.172

RETARDATION EFFECTS IN $ed \to e'np$ REACTION

V.V.Burov, A.A.Goy*, S.Eh.Sus'kov*

Electrodisintegration of the deuteron near pion threshold with allowance for retardation effects in meson exchange currents is studied. It is shown that retardation effects should be taken into account at large transfer momenta ($t > 10\,\text{fm}^{-2}$). The radial dependence of the matrix elements for $d \to {}^1S_0$-transition has been investigated. It is found that the inclusion of meson exchange currents with allowance for retardation effects is important at $r = 1—1.5$ fm, when $t < 30\,\text{fm}^{-2}$.

The investigation has been performed at the Laboratory of Theoretical Physics, JINR.

Эффекты запаздывания в $ed \to e'np$-реакции

В.В.Буров, А.А.Гой, С.Э.Суськов

Исследован электроразвал дейтрона на пороге пионообразования с учетом эффектов запаздывания в мезонных обменных токах. Показана необходимость учета эффектов запаздывания в области больших импульсов передачи ($t > 10$ фм$^{-2}$). Рассмотрена радиальная зависимость матричных элементов для $d \to {}^1S_0$-перехода. Установлено, что вклад мезонных обменных токов с учетом эффектов запаздывания наиболее существенен при $r = 1—1.5$ фм для $t < 30$ фм$^{-2}$.

Работа выполнена в Лаборатории теоретической физики ОИЯИ.

1. Introduction

Magnetic $M1$-transition in the $ed \to e'np$ reaction with inclusion of meson exchange currents has been studied earlier in refs. [1—7]. Detailed calculations have been made with allowance for seagull and meson currents (fig.1(a), (b)). However, the investigations of the retardation effects have not been done yet. The reason is the lack of experimental results at large momentum transfer. In this case the traditional set of meson exchange currents (see fig. 1) was quite enough to get the correct information on the differential cross section in a small region of transfer momenta.

*Far-East State University, Vladivostok, Russia

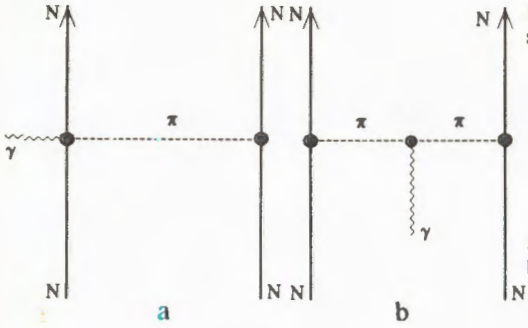

Fig.1. Diagrams of seagull (a) and meson (b) currents

Fig.2. Diagrams of recoil (a) renormalization (b) currents

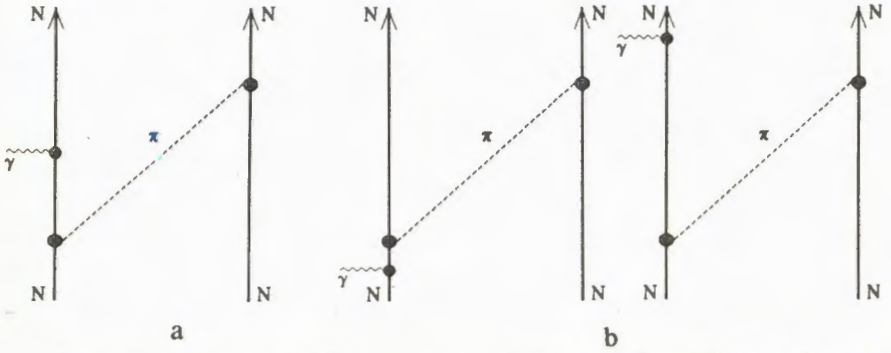

At present the available experimental data on the differential cross section are known up to about 1 GeV that allow one to investigate the electrodisintegration near threshold at short distances where the relativistic contributions have to be important.

The retardation of meson exchange currents is one of significant relativistic effects, whose investigation has been done. In ref. [8] the retardation current was studied for the elastic *e-d* scattering. It was shown that the inclusion of retardation meson exchange current into the structure function $B(q^2)$ has a considerable effect at large transfer momenta. Moreover, for the structure function $A(q^2)$ the contribution of retardation effects worsens the agreement with experimental data thus compelling one to take account of other effects, for instance, quark degrees of freedom. That situation provokes the investigation of the deuteron structure when all the contributions of meson exchange currents are taken into account including retardation effects.

In the present paper, the electrodisintegration of the deuteron with allowance for retardation effect has been investigated.

Moreover, the radial dependence of the matrix elements for $d \to {}^1S_0$-transition with allowance for retardation effect has been studied. It was founded earlier in ref. [7] that the meson exchange currents (fig.1) dominate

if the relative distance between two nucleons is between 1 and 1.4 fm for $t \leq 30$ fm^{-2}. In our work the influence of retardation effects is studied, which is necessary to get a realistic picture of the radial dependence at high momentum transfers.

2. Model

According to ref. [6] the differential cross section for the $d \to {}^1S_0$-transition has the form

$$\frac{d^2\sigma}{d\Omega d\omega} = \frac{16}{3}\alpha^2 \frac{k_f^2}{\mathbf{q}^2}\frac{KM}{t^2}\sin^2\frac{1}{2}\theta((k_i + k_f)^2 - 2k_i k_f \cos^2\frac{1}{2}\theta)|\langle {}^1S_0||T_1^{\mathrm{Mag}}||d\rangle|^2, \quad (1)$$

$k_{i(f)}$ is the initial (final) momentum of the electron, $\mathbf{q}$ is the vector of momentum transfer, t stands for the four momentum transfer. The magnetic multipole T_1^{Mag} is expressed through the isovector current operator $\mathbf{J}$ as follows

$$T_1^{\mathrm{Mag}}(q) = \int j_1(qx)\mathbf{Y}^M_{111}(\Omega_x)\,\mathbf{J}dx. \quad (2)$$

The expression for the isovector retardation current is derived in the framework of the S-matrix method for $M1$ - transition due to π exchange. We have the following equation:

$$\mathbf{J}^R = \mathbf{J}^A + \mathbf{J}^B \quad (3)$$

with

$$\mathbf{J}^A = -iG_M^v(t)\frac{f^2}{32\pi M^2 m_\pi^2}\frac{1}{\omega^4}\left(i(\tau_1 \times \tau_2)_3 + \tau_3^2\right) \times$$

$$\times \left(\sigma_1 \cdot \mathbf{k}_2\right)\left(\sigma_1 \times \mathbf{q}\right)\left(\mathbf{q}\cdot\mathbf{k}_2\right)\left(\sigma_2\cdot\mathbf{k}_2\right), \quad (4)$$

$$\mathbf{J}^B = -F_1^v(t)\frac{f^2}{32\pi M^2 m_\pi^2}\frac{1}{\omega^4}\left(i(\tau_1\times\tau_2)_3 + \tau_3^2\right)\mathbf{k}_2\left(\sigma_1\cdot\mathbf{k}_2\right)\left(\mathbf{q}\cdot\mathbf{k}_2\right)\left(\sigma_2\cdot\mathbf{k}_2\right). \quad (5)$$

Here $f^2/4\pi = 0.08$, M is the nucleon mass, m_π denotes the pion mass, $\mathbf{k}_{1(2)} = \mathbf{p}'_{1,2} - \mathbf{p}_{1,2}$ ($\mathbf{p}_{1,2}$, $\mathbf{p}'_{1,2}$ are the initial and final momenta of two nucleons), ω is the pion energy,

$$G_M^v(t) = \frac{4.706}{1 + \dfrac{t}{18.23\ \text{fm}^{-2}}}, \tag{6}$$

$$F_1^v(t) = \frac{1}{\left(1 + \dfrac{t}{18.23\ \text{fm}^{-2}}\right)^2} \frac{1}{1 + \dfrac{t}{4M^2}} \left(1 + 4.706 \frac{t}{4M^2}\right) \tag{7}$$

(see [6]). The matrix elements for seagull and meson currents have been derived in ref. [6]. In this paper we have determined the matrix element for the retardation current. The retardation matrix element for $d \to {}^1S_0$-transition has the following form

$$\langle {}^1S_0 \| T_{1,R}^{\text{Mag}} \| d \rangle = i \frac{q}{\sqrt{2\pi}} \int_0^\infty \eta(r, t) dt. \tag{8}$$

Here

$$\eta(r, t) = G_M^v(t) \frac{f^2}{80\pi^3 M^2 m_\pi^2} u_0(r) \{ j_1 (\tfrac{1}{2} qr) (\tfrac{1}{\sqrt{2}} u(r) 19 I_1(r) +$$

$$+ w(r) \frac{1}{10} (-13 I_1(r) - 8 I_3(r))) + j_3(\tfrac{1}{2} qr) (\tfrac{1}{\sqrt{2}} u(r) 11 I_3(r) +$$

$$+ W(r) \frac{1}{10} (7 I_1(r) - 28 I_3(r)))\}, \tag{9}$$

where $u(r)$, $w(r)$, $u_0(r)$ are wave functions of S, D states of the deuteron and ${}^1S_0$-final state, respectively. The radial functions $I_l(r)$ are given by

$$I_l(r) = \int_0^\infty k^5 j_l(kr) \frac{K_\pi^2(k)}{(k^2 + m_\pi^2)^2} dk. \tag{10}$$

Kinematical quantities are related in the following way

$$q = \sqrt{\frac{((M_n + M_p + E_{np})^2 - M_d^2 + t)^2}{4M_d^2}} + t, \tag{11}$$

where M_n, M_p, M_d are the neutron, proton and deuteron mass, respectively. For $r \to \infty$, we have

$$u_0(r) \to \frac{1}{K} \sin(Kr + \delta_0). \tag{12}$$

The momentum K is related to the relative energy of np system E_{np} as follows

$$E_{np} = \frac{K^2}{M}. \tag{13}$$

Note that the result (8) is independent of J^B.

To determine the realistic properties of a two-nucleon system, the inner structure of nuclei at short distances has to be taken into account. In this case the bare πNN vertex has to be parametrized by the vertex form factor $K_\pi(k)$. We shall investigate two parametrization forms of the vertex form factor. The first one is of a monopole form. According to ref. [6] we have

$$K_\pi(k) = \frac{\Lambda_\pi^2 - m_\pi^2}{\Lambda_\pi^2 + k^2}. \tag{14}$$

The second parametrization ensures the monopole behavior at small k^2 that is usually used in the low-energy reactions, and the $(k^2)^{-3}$ decrease at large k^2 assigned by quantum chromodynamics [10] is given by

$$K_\pi(k) = \frac{1}{(1 + \frac{k^2}{\Lambda_{1,\pi}^2})(1 + \frac{k^4}{\Lambda_{2,\pi}^4})}. \tag{15}$$

We shall investigate different values of the cut-off parameters related to the rms of the nucleon: 0.48 fm and 0.7 fm. Here $\Lambda_\pi = 1.25$ GeV or 0.85 GeV, respectively. A detailed analysis of rms was done in ref. [6]. The cut-off parameters $\Lambda_{1,\pi} = 0.99$ GeV, $\Lambda_{2,\pi} = 2.58$ GeV were determined in ref. [10]. The calculations with the vertex form factor (15) were made with the following renormalization of the coupling constant f:

$$f = f\left(1 - \frac{m_\pi^2}{\Lambda_\pi^2}\right). \tag{16}$$

3. Results and Discussion

Calculations of the differential cross section have been done with the relative energy of np system $E_{np} = 1.5$ MeV and scattering angle $\theta = 155°$ with the use of wave functions of the Paris potential. The results for the differential cross section with allowance for meson exchange currents (figs.1,2) are shown in fig.3.

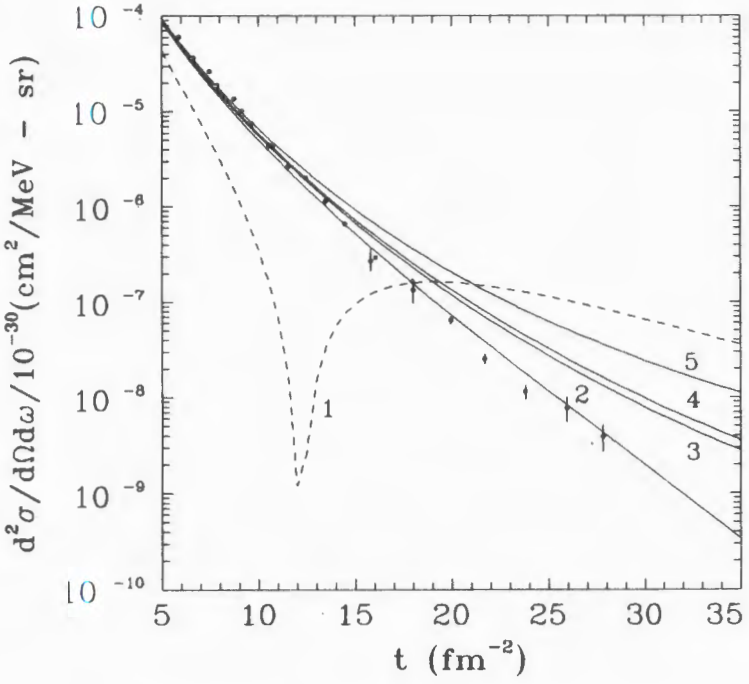

Fig.3. Differential cross section. The dashed line 1 is the impulse approximation, 2 is the calculation with the vertex form factor (14), and $\Lambda_\pi = 0.85$ GeV, 3,4 are the calculations with the vertex form factor (15), $\Lambda_\pi = 0.85$ GeV and $\Lambda_\pi = 1.25$ GeV, respectively, 5 is the calculation with the vertex form factor (14) and $\Lambda_\pi = 1.25$ GeV. The experimental data from [11], [12]

It is seen that the results are very sensitive to the parametrization form of the vertex form factor and cut-off parameters. First of all we note that the calculation with monopole parametrization form (14) and cut-off parameter $\Lambda_\pi = 1.25$ GeV (curve 5) destroys the agreement with experimental results in the region of $t > 10$ fm^{-2}.

The inclusion of $\Lambda_\pi = 0.85$ GeV, curve 2, leads to a more positive result which is not in contradiction with the experimental data.

Curves 3,4 (see (16)) show the calculations of the same differential cross section but with the rapid-decreasing vertex form factor (15). Here, in contrast with the monopole vertex form factor, we get results in contradiction with the experimental data in the region of $t > 13$ fm^{-2}.

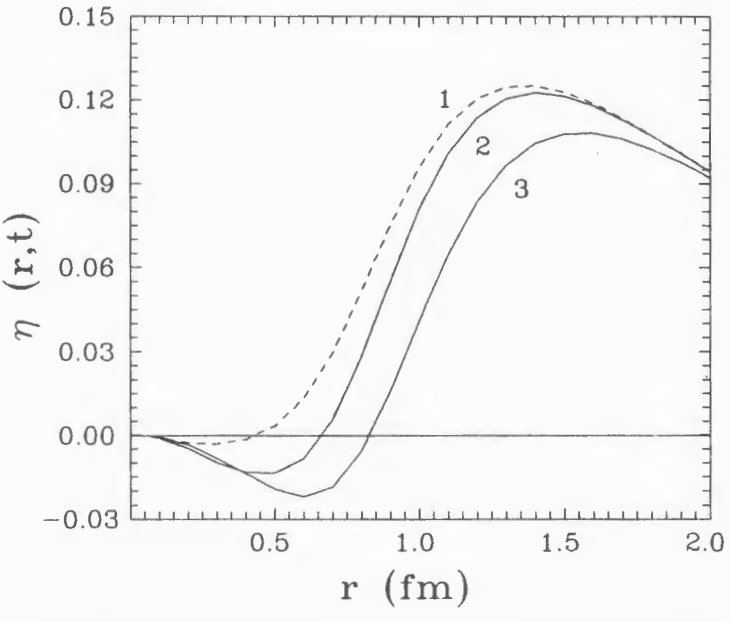

Fig.4. The dashed line 1 is the calculation for point particles. 2 is the inclusion of MEC with allowance for retardation effects (S+M+R) and $\Lambda_\pi = 1.25$ GeV. 3 is the inclusion of MEC with allowance for retardation effects (S+M+R), with $\Lambda_\pi = 0.85$ GeV. The calculations were made with the vertex form factor (14) and $t = 0$ fm^{-2}

Now let us consider the radial dependence of the matrix elements on the momentum t. Figures 4,5 show the calculations of the radial functions $\eta(r, t)$ for the vertex form factor (14) with $\Lambda_\pi = 1.25$ GeV and $\Lambda_\pi = 0.85$ GeV for momenta transfer $t = 0$ fm^{-2} and $t = 30$ fm^{-2}.

It is seen that if $t = 0$ fm^{-2}, the retardation effects are absent (fig.4 curve 2,3). In this case curves 2 and 3 are absolutely identical with the calculation without retardation current. The total result dominates in the range of relative distances of about 1.4 fm for $\Lambda_\pi = 1.25$ GeV and 1.5 fm for $\Lambda_\pi = 0.85$ GeV.

However, the retardation effects are more manifest in the calculations at large transfer momenta.

Comparing the result obtained with allowance for retardation effects, fig.5 (curves 3,5),with the analogous calculation with the use of the seagull

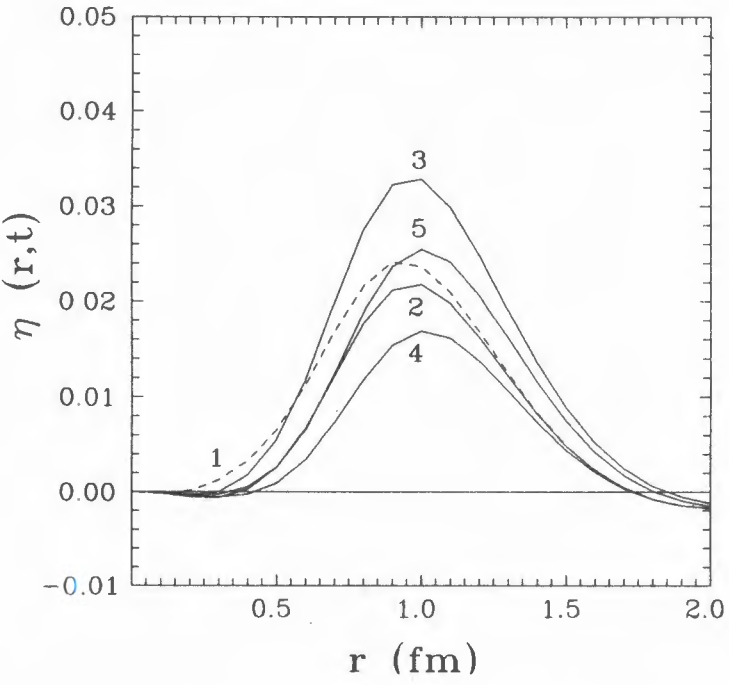

Fig.5. The dashed line 1 is the calculation for point particles. 2 is the inclusion of MEC (S+M), 3 is the inclusion of MEC with allowance for retardation effects (S+M+R) and $\Lambda_\pi = 1.25$ GeV. Calculations 4,5 are the same as 2, 3, but for $\Lambda_\pi = 0.85$ GeV. The calculations were made with the vertex form factor (14) and $t = 30$ fm^{-2}

and meson currents, curves 2 and 4, we see, that retardation effects give a very considerable contribution at $t = 30$ fm^{-2}. Here, the considered set of meson exchange currents dominates in the range of about 1 fm, which is not in contradiction with the previous result of ref. [7].

4. Conclusion

The investigation of the electrodisintegration of the deuteron near threshold with allowance for retardation effects in MEC allows us to make the following conclusions.

1. The inclusion of retardation effects leads to noticeable discrepancies with experimental data at large transfer momenta ($t > 10\ \text{fm}^{-2}$).

2. The calculations are very sensitive to the value of cut-off parameters and strongly depend on the vertex form factors.

3. The meson exchange currents dominate when the relative distance between two nucleons is of about 1—1.5 fm, when $t < 30\ \text{fm}^{-2}$.

4. Generally speaking, the calculations of the differential cross section with allowance for retardation effects at large transfer momenta force us to take account of other degrees of freedom.

References

1. Hockert J., Riska D.O., Gari M., Huffman A. — Nucl.Phys., 1973, A217, p.14.
2. Lock J.A., Foldy L.L. — Annals of Physics, 1975, 93, p.276.
3. Fabian W., Arenhovel H. — Nucl.Phys., 1976, A258, p.461.
4. Sommer B. — Nucl. Phys., 1978, A308, p.263.
5. Leidemann W., Arenhovel H. — Nucl. Phys., 1983, A393, p.385.
6. Mathiot J.F. — Nucl.Phys., 1984, A412, p.201.
7. Mathiot J.F. — Phys. Lett., 1987, 187, p.235.
8. Burov V.V., Dostovalov V.N., Sus'kov S.Eh. — Czechoslovak Journal of Physics, 1991, 41, p.1139.
9. Gari M., Hyuga H. — Z.Phys. A-Atoms and Nuclei, 1976, 277, p.291.
10. Gari M., Kaulfuss U. — Phys.Lett., 1984, 136B, p.139.
11. Bernheim M. et. al. — Phys. Rev. Lett., 1981, 46, p.402.
12. Auffret S. et al. — Phys. Rev. Lett., 1985,55,p.1362.

Received on October 5, 1992.

УДК 539.12.01

ANOTHER POSSIBILITY OF CONSERVED-VECTOR-CURRENT HYPOTHESIS VERIFICATION

A.Z.Dubničková, S.Dubnička, M.P.Rekalo*

Based on the conserved-vector-current (CVC) hypothesis and a four-ρ-resonance unitary and analytic VMD model of the pion electromagnetic form factor, the behaviour of a total cross section and energy distribution of the final state pions of $\bar{\nu}_e e^- \to \pi^- \pi^0$ process are predicted theoretically for the first time. An experimental confirmation of the latter could provide another reliable method of CVC-hypothesis verification for all energies above the two-pion threshold.

The investigation has been performed at the Laboratory of Theoretical Physics, JINR.

Другая возможность проверки гипотезы сохранения векторного тока

А.З.Дубничкова, С.Дубничка, М.П.Рекало

На основе гипотезы сохранения векторного тока (СВТ) и унитарной и аналитической ВМД-модели с четырьмя ρ-резонансами для описания электромагнитного формфактора пиона впервые теоретически предсказывается поведение полного сечения и энергетическое распределение пионов в конечном состоянии и процессе $\bar{\nu}_e e^- \to \pi^- \pi^0$. Экспериментальная проверка предсказанного представляет другой метод проверки СВТ-гипотезы для всех энергий выше двухпионного порога.

Работа выполнена в Лаборатории теоретической физики ОИЯИ.

In the V-A theory of weak interactions [1] the hadronic charged weak current J_μ^W is a compound of vector V_μ and axial-vector A_μ currents. In the second half of the fifties the conserved-vector-current (CVC) hypothesis

$$\partial_\mu V_\mu = 0 \qquad (1)$$

was postulated [2,3] in order to explain an approximate numerical equality of the muon decay constant G^μ and the neutron decay vector constant $G^{(V)}$. Later on the CVC-hypothesis manifested to be very powerful. Here we

*Kharkov Institute of Physics and Technology, Kharkov, Ukraine

notice only the relation between a matrix element $\langle \pi^0 | V_\mu | \pi^+ \rangle$ and a matrix element $\langle \pi^+ | J_\mu^E | \pi^+ \rangle$ of the electromagnetic (e.m.) current J_μ^E following directly from (1), which finally leads to the relation

$$F_\pi^W(s) = \sqrt{2}\, F_\pi^{E,I=1}(s) \tag{2}$$

between the weak pion form factor (ff) $F_\pi^W(s)$ of a virtual W^--boson transition $(W^-)^* \to \pi^-\pi^0$ and the pure isovector e.m. pion form factor $F_\pi^{E,I=1}(s)$ of a virtual photon $\gamma^* \to \pi^+\pi^-$ transition, where $\sqrt{2}$ is a Clebsch-Gordan coefficient of the SU(2) isotopic group. The relation (2) has shown to be very useful. There are neither data on $F_\pi^W(s)$ nor an accomplished theory, nor a phenomenology giving a reliable behaviour of the weak pion ff. On the other hand, the behaviour of the e.m. pion ff is understood from the experimental (for a compilation see [4]) and phenomenological points of view [5,6] quite well. So, the relation (2) already in an early stage allowed [2,3] to predict a probability of the pion beta-decay $\pi^+ \to \pi^0 e^+ \nu_e$. Its experimental confirmation [7] is now presented as one of the brilliant demonstrations of a general validity of the CVC-hypothesis in the weak interaction theory. However, there is a release of a negligible amount of energy in the pion beta-decay and in fact one is authorized to speak about a CVC-hypothesis verification only in surroundings of $s \approx 0$.

To validate experimentally the CVC-hypothesis outside this restricted region, we propose here to investigate the weak $\bar{\nu}_e e^- \to \pi^-\pi^0$ process. Its threshold energy is $E_\nu^{(0)} \approx 2m_\pi^2/m_e \approx 76.7$ GeV and so, it is already attainable experimentally on existing accelerators.

The differential cross-section of the weak $\bar{\nu}_e e^- \to \pi^-\pi^0$ reaction in the c.m. system is given by the expression

$$\frac{d\sigma}{d\Omega} = \frac{1}{(2s_{\bar{\nu}}+1)(2s_e+1)} \frac{1}{64\pi^2 s} \frac{k}{p} \sum_{s_{\bar{\nu}}, s_e} |M|^2, \tag{3}$$

where $s \geq 4m_\pi^2$ is the c.m. energy squared, $k = ((s-4m_\pi^2)/4)^{1/2}$ is the length of a 3-dimensional momentum of produced pions, $p = (s/4)^{1/2}$ is the length of a 3-dimensional neutrino-momentum and $s_{\bar{\nu}}$ and s_e are spins of the antineutrino and electron, respectively. The matrix element M in the lowest order of a perturbation expansion can be calculated from the Feynman diagram presented in Fig.1a, that for $s << m_W^2$ is reduced to a contact diagram presented in Fig.1b.

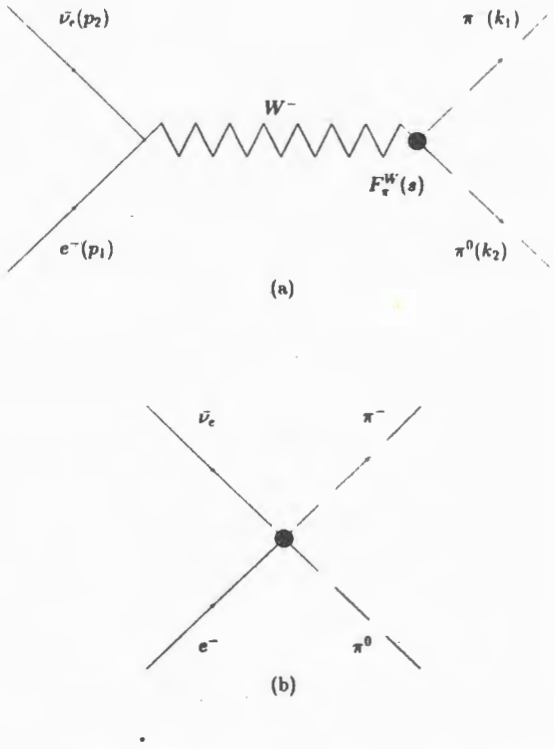

Fig. 1. The lowest order perturbation expansion Feynman diagram giving a dominant contribution to the weak $\bar{\nu}_e e^- \to \pi^-\pi^0$ process

It takes the form

$$M = \frac{G}{\sqrt{2}}\bar{\nu}_e(p_2)\gamma_\mu(1+\gamma_5)e(p_1)\,(k_1-k_2)^\mu F_\pi^W(s), \tag{4}$$

where $G = 1.1663\cdot 10^{-5}\ \mathrm{GeV}^{-2}$ is the weak interaction Fermi constant. The expression (4) leads to

$$\frac{d\sigma}{d\Omega} = \frac{G^2}{128\pi^2}\, s\beta_\pi^3\, |F_\pi^W(s)|^2 \sin^2\theta, \tag{5}$$

where $\beta_\pi = (1 - 4m_\pi^2/s)^{1/2}$ is the velocity of produced pions and θ is the scattering angle in the c.m. system. To predict a behavior of $\sigma_{\mathrm{tot}}(E_\nu^{\mathrm{lab}})$, first

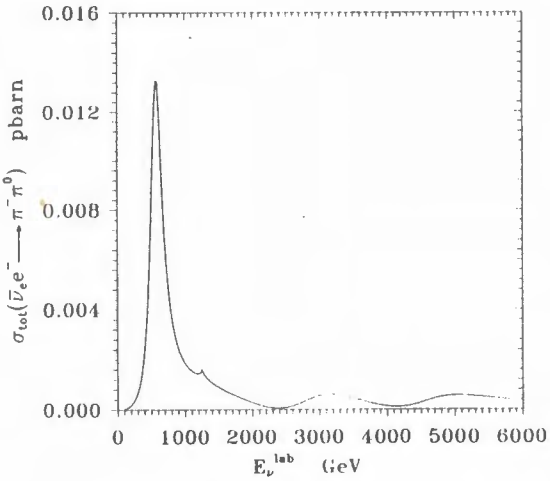

Fig.2. The predicted by (6) behaviour of the total cross-section of the $\bar{\nu}_e e^- \to \pi^- \pi^0$ process at the laboratory system

we multiply (5) by $d\Omega = \sin\theta\, d\theta\, d\varphi$, then integrate over angles θ and φ and finally substitute the expression (2) (generally valid for $-\infty < s < +\infty$) and the relation $s = m_e^2 + 2m_e E_\nu^{lab}$. As a result, one gets

$$\sigma_{tot}(E_\nu^{lab}) = \frac{G^2}{24\pi}(m_e^2 + 2m_e E_\nu^{lab})\beta_\pi^3 \, |F_\pi^{E,I=1}(E_\nu^{lab})|^2 \qquad (6)$$

from which, by using four-ρ-resonance unitary and analytic VMD model [6] of the pion e.m. ff, the behaviour of $\sigma_{tot}(E_\nu^{lab})$ in the laboratory system as shown in Fig.2 is predicted.

Besides the $\sigma_{tot}(E_\nu^{lab})$ it is interesting also to predict an energy distribution of the pions created in the weak $\bar{\nu}_e e^- \to \pi^- \pi^0$ process to be given by $d\sigma/dE_\pi^{lab}$. The latter is obtained from (5), first by integration over the φ angle and then by substitution of the relations

$$d\cos\theta = -\frac{m_e}{k^{c.m.}\, p^{c.m.}} dE_\pi^{lab}; \quad s \approx 2m_e E_\nu^{lab};$$
$$\sin^2\theta = 1 - \frac{(E_\pi^{c.m.} E_e^{c.m.} - m_e E_\pi^{lab})^2}{(k^{c.m.})^2 (p^{c.m.})^2} dE_\pi^{lab}, \qquad (7)$$

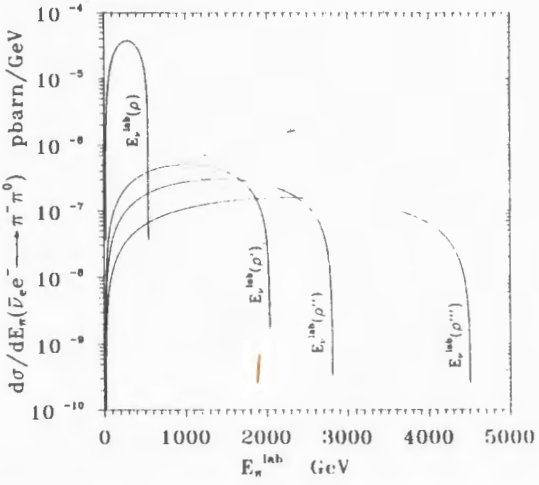

Fig.3. The predicted behaviour of the energy distribution of pions as given by (8)

where

$$E_\pi^{c.m.} \approx E_e^{c.m.} \approx p^{c.m.} \approx \sqrt{\frac{m_e}{2} E_\nu^{lab}} \quad \text{and} \quad k^{c.m.} \approx \sqrt{\frac{m_e}{2}(E_\nu^{lab} - E_\nu^{(0)})}.$$

Consequently, one gets the expression

$$\frac{d\sigma}{dE_\pi^{lab}} = \frac{m_e G^2}{8\pi} \left(\frac{E_\nu^{lab} - E_\nu^{(0)}}{E_\nu^{lab}} \right) \left\{ 1 - \frac{(E_\nu^{lab} - 2E_\pi^{lab})^2}{E_\nu^{lab}(E_\nu^{lab} - E_\nu^{(0)})} \right\} |F_\pi^{E,I=1}(E_\nu^{lab})|^2 \tag{8}$$

from which the energy distribution of the final state pions of the reaction $\bar{\nu}_e e^- \to \pi^- \pi^0$ at four different energies corresponding just to $\rho(770)$, $\rho'(1450)$, $\rho''(1700)$, $\rho'''(2150)$ resonances is calculated. The results are graphically presented in Fig.3.

The experimental approval of our predictions for $\sigma_{tot}(E_\nu^{lab})$ and $d\sigma/dE_\pi^{lab}$ could validate the CVC-hypothesis for all investigated energies above the two-pion threshold.

References

1. Bernstein J. — Elementary Particles and Their Currents, Freeman, San Francisco, 1968.
2. Gernstein S.S., Zeldowich Ya.B. — ZhETP, 1955, 29, p.698.
3. Feynman R.P., Gell-Mann M. — Phys.Rev., 1958, 109, p.193.
4. Dubničková A.Z., Dubnička S., Khasin B.I., Mäsiar P. — Czech. J.Phys., 1987, B37, p.815.
5. Dubnička S., Furdík I., Meshcheryakov V.A. — JINR Preprint, E2-88-521, Dubna, 1988.
6. Biagini M.E., Dubnička S., Etim E., Kolář P. — Nuovo Cim., 1991, A104, p.363.
7. Review of Particle Properties, Phys.Lett., 1990, B239, April.

Received on October 16, 1992.

УДК 539.12.01

PROTON-PROTON BREMSSTRAHLUNG AND NARROW DIPROTON RESONANCES

S.B.Gerasimov, A.S.Khrykin

The possibility is suggested and discussed of using the bremsstrahlung reaction in proton-proton interactions as a new tool for searching and investigating the narrow diproton resonances.

The investigation has been performed at the Laboratory of Nuclear Problems, JINR.

Протон-протонное тормозное излучение и узкие дипротонные резонансы

С.Б.Герасимов, А.С.Хрыкин

Предлагается и обсуждается возможность использования реакции тормозного излучения в протон-протонном взаимодействии в качестве нового способа для поиска и исследования узких дипротонных резонансов.

Работа выполнена в Лаборатории ядерных проблем ОИЯИ.

1. Introduction and Motivation

The discovery of the dibaryon (and, possibly, multibaryon) resonances would, undoubtedly, be of great importance for many parts of hadron physics including nuclear physics. Although the evidences for dibaryon resonances have repeatedly been reported in many experiments, the situation cannot be regarded as a well-determined. The current status of this problem [1,2,3] advances its unambiguous solution to the level of main tasks of the nucleon-nucleon interaction physics at intermediate energies.

Among the available dibaryon candidates, the group of narrow resonances with masses M_B in the range $2m_p < M_B < 2m_p + m_\pi$ presents special interest. In this paper, we suggest discussing the novel means of searching and investigating the dibaryon resonances of that type. Our main purpose is to show the utility and expediency of the proton-proton bremsstrahlung to search for the narrow diproton resonances.

As the starting arguments in favour of this proposal the following remarks appear to be pertinent:

- The common feature of all dibaryon candidates is the small value of their coupling to the NN-channel. The direct confirmation of this salient feature is provided by the recent experiment on searching for narrow resonances in pp-scattering with a small step of the incident proton energy variation [4]. Therefore, the use of the inelastic NN-channels appears to be a more perspective way of inquiring into dibaryon resonances [5].
- The decay modes of resonances with masses $M_B < 2m_p + m_\pi$ are pp- and $pp\gamma$-channels. The experimental indications of radiative decay channels were obtained in reactions including atomic nuclei [5,6]. However, from the point of view of simplicity and reliability of data interpretation, the radiative processes in the «elementary» NN-interaction would have undoubted advantages. Among all inelastic NN-reactions the bremsstrahlung is the simplest one. The experience accumulated in the experimental and theoretical investigation of $NN \to NN\gamma$ reactions is very useful for estimation of the resonance-to-background ratio in indicated reactions.
- For some spatial or internal quantum numbers the decay $B \to pp$ may be forbidden or suppressed by the rigorous (Pauli principle) or approximate (isospin, etc.) selection rules. The radiative channel of the resonance production $pp \to \gamma B$ and subsequent decay $B \to \gamma pp$ will then be the unique or principal channel if the proton energy is below the pion production threshold. The use of the double bremsstrahlung reaction in the region of the assumed resonances (the coincidence measurement) allows favourable possibilities to determine the quantum numbers of the explored resonances at the advantageous signal to background conditions (i.e., background from the ordinary, bremsstrahlung mechanism is expected to be strongly reduced) and with the minimal free parameters to be determined experimentally.

2. The Model of «External» Radiation of Soft Photons Near the Resonance

Firstly, we consider the bremsstrahlung reaction near the resonance with quantum numbers allowing «elastic» decay channel $B \to pp$ when $\Gamma_{tot} \cong \Gamma(B \to pp)$. We refer to this case as the «external» bremsstrahlung because in this case the dominant radiation mechanism is described by the pole diagrams in Fig.1 (a—e) and is determined by the electromagnetic characteristics and resonant interaction amplitude of the colliding particles. As far as the quantum numbers of a resonance are regarded as unknown, it is impossible to calculate the radiative amplitude taking into account

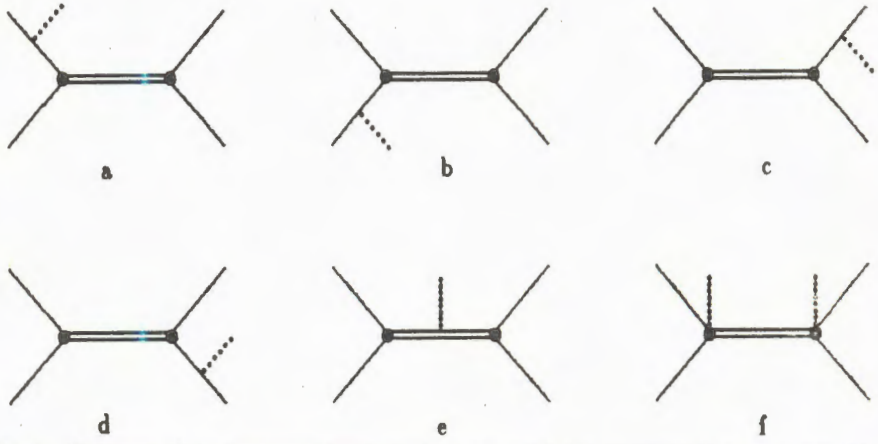

Fig.1. Diagrams of the bremsstrahlung reaction. The solid line corresponds to nucleons; the double line, to dinucleon resonance; the doted line, to photon

consistently all spin dependent characteristics of particles (magnetic moment, etc.) and the interaction, and therefore, we have to confine ourselves to retaining only the «charge» (convection) part of the corresponding electromagnetic currents. However, as it has been shown for the case of the ordinary, nonresonant bremsstrahlung [8], the neglect of the magnetic moments is justified at relatively low photon energies. The inclusion of only the convection current results in obtaining the lower bound of the considered cross section. The presence of the narrow resonance will, obviously, produce the characteristic, narrow γ-line in the emitted photon spectrum. The position and shape of this line are mainly determined by kinematics of the initial stage of the quasi-two-particle reaction $pp \to \gamma B \to \gamma X$ through the resonance mass M_B and width Γ_{tot}. Our approximation (allowing for charge/convection current only) and dominance of the contribution to the cross section from the initial particle radiation permit us to give the general expression for the inclusive photon distribution in an arbitrary reaction $a + b \to \gamma + R \to \gamma + X$ near the resonance R with mass M_R, spin J_R and partial width $\Gamma_{ab} \equiv \Gamma(R \to ab)$ for any charge $Z_{a(b)}$ (in units of e) and masses $M_{a(b)}$ of the colliding particles:

$$\frac{d^2\sigma}{d\omega d\Omega_k}(ab \to \gamma R \to \gamma X) = \frac{\alpha}{4\pi^2}\,\frac{1}{\omega}\,F_{ab}(p,\theta)\,\frac{p'W'}{pW}\,\sigma^{BW}(s'), \qquad (1)$$

where

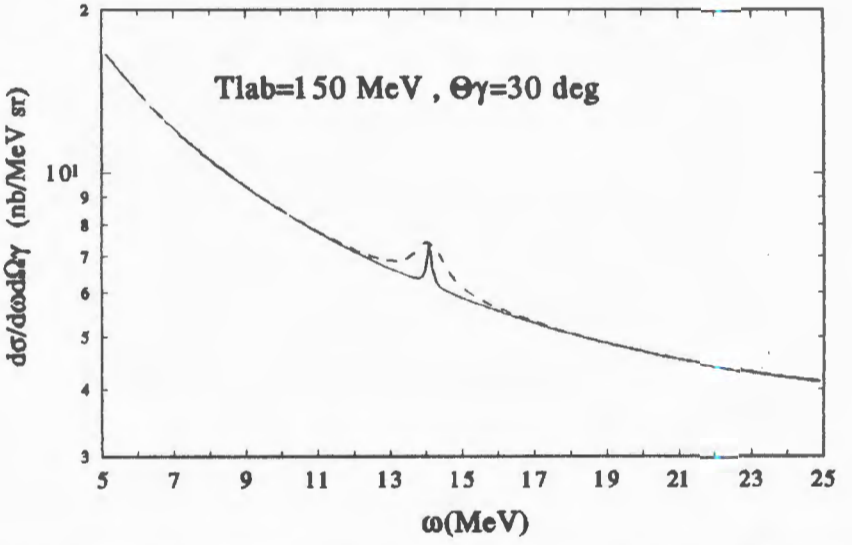

Fig.2. Differential cross section for $pp \to \gamma X$ reaction («external» radiation). The solid curve corresponds to $\Gamma_{tot} = 0{,}150$ MeV; the dashed curve, to $\Gamma_{tot} = 1.0$ MeV

$$F_{ab}(p,\theta) = \frac{[Z_a\beta_a - Z_b\beta_b + (Z_a + Z_b)\beta_a\beta_b\cos\theta\,]^2 \sin^2\theta}{(1-\beta_a\cos\theta)^2\,(1+\beta_b\cos\theta)^2}, \qquad (2)$$

$$\sigma^{BW}(s') = \frac{4\pi}{p'^2}\,\frac{2J_R+1}{(2J_a+1)\,(2J_b+1)}\,\frac{M_R^2\Gamma_{ab}\Gamma_{tot}}{(s'-M_R^2)^2 + M_R^2\Gamma_{tot}^2}, \qquad (3)$$

$$p = \frac{(s-(M_a+M_b)^2)^{1/2}\,(s-(M_a-M_b)^2)^{1/2}}{4s^{1/2}}, \qquad (4)$$

$$\beta_{a(b)} = \frac{p}{E_{a(b)}} = \frac{2ps^{1/2}}{s + M_{a(b)}^2 - M_{b(a)}^2}, \qquad (5)$$

$s \equiv W^2 = (p_a + p_b)^2$, $s' \equiv W'^2 = (p_a + p_b - k)^2 = s - 2\omega\sqrt{s}$, $p \leftrightarrow p'(s \leftrightarrow s')$, $\cos\theta \equiv \hat{\mathbf{p}}_a\,\hat{\mathbf{k}}$, $J_{a(b)}$ — spin of the particle $a(b)$, $\alpha = 1/137$, ω — photon

energy in c.m.s. For $a \to N$ and $b \to N$ in various charge states, we obtain from Eq. (2) in the leading nonrelativistic appraximation:

$$F_{NN}(p, \theta) = \begin{cases} 4\frac{p^4}{m^4} \sin^2\theta \cos^2\theta & (a \leftrightarrow p, b \leftrightarrow p) \\ \frac{p^2}{m^2} \sin^2\theta & (a \leftrightarrow p, b \leftrightarrow n), \\ 4\frac{p^2}{m^2} \sin^2\theta & (a \leftrightarrow p, b \leftrightarrow \bar{p}) \end{cases} \quad (6)$$

where m is a nucleon mass. For the illustrative purposes, and to estimate the possible signal-to-background ratio the $pp \to \gamma X$ reaction cross section is presented in Fig.2 at some fixed values of the initial proton kinetic energy T_{lab}, and photon angle θ_γ. Rather arbitrary, we take $\Gamma_{tot} \cong \Gamma(B \to pp) = 0.15 \div 1$ MeV, $J_B = 0$ and $M_B = 1936$ MeV for the assumed resonance parameters. It should be noted that for $J_B \neq 0$ the height of the resonant peak must be increased $(2J_B + 1)$ times.

3. The Case for «Internal» Bremsstrahlung Near the Resonance

For the radiative processes, like the nuclear photodisintegration or meson photoproduction [9] or considered here bremsstrahlung reaction, the case when the dinucleon resonance decay into the NN-channel is either forbidden or hindered presents special interest. It is easily seen that the Pauli principle forbids the parity-odd (even) spin-singlet and parity-even (odd) triplet NN-states with the isospin $I = 1$ $(I = 0)$. For any of the possible spin values of the NN-system the following combinations of the total angular momentum J and parity P are forbidden:

$$J^P = \begin{cases} 1^+, 3^+, 5^+ \ldots, & \text{if } I = 1 \quad (7a) \\ 0^\pm, 2^-, 4^- \ldots, & \text{if } I = 0 \quad (7b) \end{cases}$$

For the pp-state the validity of the selection rule (7a) takes place regardless requirements of the isospin symmetry. Thus, if the diproton resonance has J^P from the set values (7a), then $\Gamma_{tot} \cong \Gamma(B \to pp\gamma)$ for $M_B < 2m_p + m_\pi$. Therefore, because of $\Gamma(B \to pp) \cong 0$, the photon emission processes entering into the resonance excitation and decay vertices will, in place of the pole diagrams in Fig.1 (a-e), be described by the diagrams as is shown in Fig.1 (f). This «internal» radiation mechanism must be accompanied by es-

sential change of the intrinsic motion of constituents composing the resonating hadronic system. We shall describe such radiative transition with the help of the effective Lagrangian $\mathfrak{L}_{\text{eff}} = \mathfrak{L}(F_{\mu\nu}, P_{\rho\sigma\ldots}, \overline{\Psi}, \Psi_c)$ involving the electromagnetic field tensor $F_{\mu\nu}$ and the fields $B_{\rho\sigma\ldots}$, $\overline{\Psi}$, Ψ_c representing the dibaryon resonance and initial or final nucleons (Ψ_c being the charge-conjugated field operator that is introduced for the baryon number conservation in appropriate vertices). To write down even the simplest form of the Lagrangian we need to know the quantum numbers (spins and parities) of the dinucleon resonance and the nucleon pair in the continuum. Taking into account the relative proximity of M_B and invariant mass of nucleons to the threshold value $W_{\text{thr}} = 2m_p$, we take, in accordance with Eq.(7a), the simplest assignment $J^P = 1^+$ for the B-resonance and $J^P = 0^+$ for the pp-pair in the continuum. Electromagnetic vertices entering into the diagram in Fig.1(f) have then the conventional form of the magnetic dipole transition, and we obtain for the cross section of the resonance reaction $pp \to \gamma B \to \gamma\gamma pp$, expressed through two free parameters (M_B and width $\Gamma_{\text{tot}} = \Gamma(B \to pp\gamma)$ and reduced to the non-relativistic limit, the following form:

$$\frac{d\sigma(pp \to \gamma B \to \gamma\gamma pp)}{d\omega_1 d\Omega_{k_1} d\omega_2 d\Omega_{k_2}} = \frac{9}{64\pi} \frac{\sqrt{m(\Delta w - \omega_1 - \omega_2)}}{|\mathbf{p}|} F_2 |D^{BW}|^2$$

$$F_2 = (1 + \cos^2(\hat{\mathbf{k}}_1 \hat{\mathbf{k}}_2)) \frac{\omega_1^3 \omega_2^3 M_B^2 \Gamma_{\text{tot}}^2}{m \Delta_B^9 C^2} \tag{8}$$

$$|D^{BW}|^2 = |D_1|^2 + |D_2|^2 + 2\text{Re}(D_1^* D_2)$$

$$D_j = (W^2 - 2\omega_j W - M_B^2 + i M_B \Gamma_{\text{tot}})^{-1}, \quad j = 1, 2,$$

where $\Delta_W = W - 2m$, $\Delta_B = M_B - 2m$, $\Gamma_{\text{rad}} = \Gamma_{\text{tot}} = \Gamma(B \to \gamma pp)$, the numerical constant $C \cong 0.1016$ being determined after the integration over the final state phase volume in the decay $B \to pp\gamma$, while we express unknown coupling constant in the effective Lagrangian through also unknown but measurable Γ_{rad}.

At the first stage of investigation of this reaction one could confine oneself in searching for the narrow γ-line at $\omega = \omega_{\text{res}} = (W^2 - M_B^2)/2W$, which would give evidence for very existence of the resonance with mass M_B. In Fig.3, the dependence is shown of the cross section $\frac{d^2\sigma}{d\omega d\Omega_k}(pp \to \gamma X)$ on the energy of a detected photon. This is obtained by integration of the reso-

Fig.3. Differential cross section for $pp \to \gamma X$ reaction («internal» radiation). The solid curve corresponds to $\Gamma_{tot} = 0.1$ keV; the dashed curve, to $\Gamma_{tot} = 1.0$ keV.

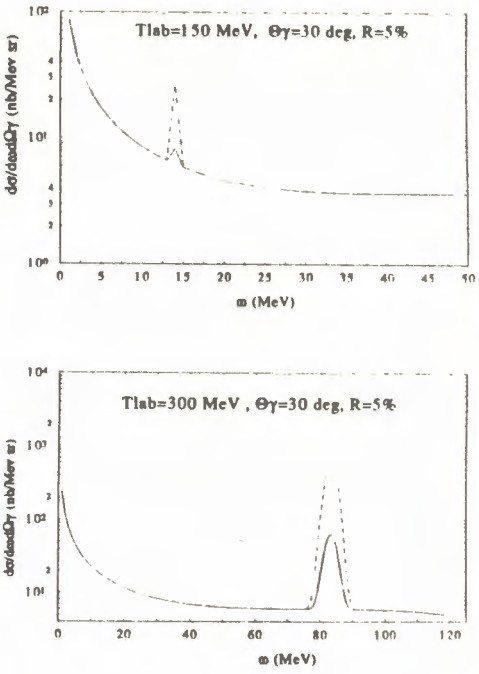

nance cross section, Eq.8, over variables of one photon. Numerical values around the resonance peak correspond to $M_B = 1936$ MeV, $\Gamma_{rad} = 01 \div 1$ keV and the Gaussian function of the experimental energy resolution with $R_\gamma = \Delta\omega/\omega = 5\%$. The smooth, «background» curve corresponds to the calculation of the *pp*-bremsstrahlung from Ref. [8].

4. Conclusion

Our estimates reveal utility of the bremsstrahlung reaction as a means of finding out and especially of further investigation of the narrow diproton resonance. We treat them as very promising and opening good perspectives. The model calculations of the radiative widths of the diproton resonances give rather crude estimations in the range 0.1÷1 keV [10,11] for the case when $\Gamma_{tot} \cong \Gamma(B \to pp\gamma)$. We believe that with a fairly simple experimental set-up one could find a more stringent upper bound limit on $\Gamma(B \to pp\gamma)$ as compared with the model estimates. If unambiguous confirmation of the narrow diproton resonances is gained, the *pp*-bremsstrahlung opens new and, seemingly, unique possibilities of their further study, e.g. the determination of the quantum numbers by using the polarized beams (targets), measuring the photon-angle-correlations in the double bremsstrahlung near resonance, supplement studying of the final particle distributions in the bremsstrahlung reactions (this aspect of the problem is discussed, within more general context, in Ref. [12]), etc.

Acknowledgements

The authors express their gratitude to A.B.Govorkov, S.N.Ershov, V.I.Komarov and Yu.A.Troyan for useful discussions of this work, V.L.Lyuboshits and M.I.Podgoretsky for acquainting them with the results of Ref. [12] befor publishing.

References

1. Loher M.P. et al. — Adv.Nucl.Phys., 1986, v.17, p.17.
2. Strakovskij I.I. — Sov.J.Part.Nucl., 1991, v.22, p.296.
3. Tatischeff B. et al. — In: Relativistic Nuclear Physics and Quantum Chromodynamics, Proc.of the Xth Int. Seminar on High Energy Physics Problems, Dubna, Russia, 24-29 September 1990, Eds. A.M.Baldin, V.V.Burov and L.P.Kaptari, World Scientific, Singapore, 1991, p.177.
4. Troyan Yu.A. et al. — Sov.Yad.Phys., 1991, v.54, p.1301.
5. Troyan Yu.A. et al. — JINR Rapid Commun., Dubna, 1985, p. 13.
6. Besliu C. et al. — JINR preprint D1-85-433, Dubna, 1985.
7. Abdinov O.B. et al. — JINR preprint P1-88-102, Dubna, 1988.
8. Herrmann V. et al. — Phys.Rev., 1991, C43, P.394.
9. Fil'kov L.V. — Sov.Yad.Phys., 1988, v.47, p.687.
10. Kaidalov A.B. — Preprint ITEP 86-128, M., 1986.
11. Pokrovsky Yu.E. — Sov.J.ZhETF, 1988, v.94, p.55.
12. Lyuboshits V.L., Podgoretsky M.I. — JINR preprint P2-92-154, Dubna, 1992. Sov.J.Nucl.Phys. (in press).

Received on September 29, 1992.

УДК 539.165.3 + 539.166.3

ON BETA DECAY OF THE ISOTOPE ^{183}Tl PRODUCED BY THE ^{147}Sm + ^{40}Ca REACTION

A. Bouldjedri[1], R.Béraud[1], R.Duffait[1], A.Astier[1], A.Emsallem[1], N.Redon[1], A.Barnéoud[2], J.Blachot[2], J.Genevey[2], A.Gizon[2], J.Inchaouh[2], Yu.A.Lazarev, Yu.Ts.Oganessian, I.V.Shirokovsky, I.N.Izosimov[3]

Beta decay of the ground state of a very neutron-deficient isotope ^{183}Tl was investigated. The ^{183}Tl was produced via the ^{147}Sm(^{40}Ca, $p3n$) reaction on the SARA cyclotron at ISN, Grenoble. Gamma lines resulting from the deexcitation of ^{183}Hg levels were observed and the half-life of ^{183}Tl was determined to be 5 ± 2 s. The known isotope ^{184}Tl was also produced and clearly identified in these experiments.

The investigations have been carried out in the framework of the JINR — IN2P3 collaboration.

О бета-распаде изотопа ^{183}Tl, образующегося в реакции ^{147}Sm + ^{40}Ca

А.Боулджедри и др.

На циклотроне SARA в Гренобле исследовался β-распад основного состояния очень нейтронодефицитного изотопа ^{183}Tl, для получения которого использовалась ядерная реакция ^{147}Sm(^{40}Ca, $p3n$). Наблюдались γ-линии, соответствующие девозбуждению уровней ^{183}Hg. Период полураспада ^{183}Tl определен равным 5 ± 2 с. В экспериментах был получен и идентифицирован также известный изотоп ^{184}Tl.

Работа выполнена в рамках соглашения между ОИЯИ и Национальным институтом физики ядра и физики частиц, Франция.

1. Introduction

During the last two decades, extensive experiments were performed to study very neutron-deficient nuclides located near the closed $Z = 82$ shell (see, e.g., Refs. [1—12]). These experiments aimed at identifying new

[1]Institut de Physique Nucléaire de Lyon, IN2P3-CNRS et Université Claude Bernard, 43 Bd du 11 Novembre 1918, F-69622 Villeurbanne Cedex, France

[2]Institut des Sciences Nucléaires, IN2P3-CNRS et Université Joseph Fourier, 53 Avenue des Martyrs, F-38026 Grenoble Cedex, France

[3]V.G.Khlopin Radium Institute, 1 Roentgen St., 197022 St.Petersburg, Russia

isotopes, searching for the ground-state proton radioactivity and probing the limits of stability of proton-rich nuclei, studying peculiarities of α-decay in this region of nuclei, characterizing nuclear isomerism which appears to be a widespread phenomenon here, and at exploring also a variety of other aspects of nuclear structure and decay.

Our interest in studying the above nuclei is motivated mainly by findings of the recent experiments performed at Dubna where a new region of $EC(\beta^+)$-delayed fission has been revealed [13—15]. In fact, the phenomenon of $EC(\beta^+)$-delayed fission was shown to occur far outside its traditional actinide nest: it was discovered for the ultra neutron-deficient nuclei of mercury and lead. Here, a prime example of $EC(\beta^+)$-delayed fission is the fission activity of $T_{1/2} = 0.97^{+0.09}_{-0.08}$ s repeatedly detected in the $^{144}Sm + ^{40}Ca$ reaction and assigned to the $^{180}Tl \xrightarrow[0.97\ s]{EC(\beta^+)} {}^{180}Hg$ decay chain [13—15]. Another striking case of $EC(\beta^+)$-delayed fission, with $T_{1/2} \cong 0.3$ s, has been revealed in the $^{151,153}Eu + ^{40}Ca$ and $^{147}Sm + ^{45}Sc$ reactions and attributed to the decay chain $^{188}Bi \xrightarrow[0.3\ s]{EC(\beta^+)} {}^{188}Pb$ [13—15]. A quantitative analysis of the results on $EC(\beta^+)$-delayed fission will give a unique information on fission barrier heights of the cold nuclei lying extremely far off the β-stability line [13,16]. This information cannot be obtained by any traditional means. However, for this analysis it is very important to perform detailed experimental studies on the radioactive properties and structure of nuclei in this region, especially on their β decay characteristics [17].

At present, the lightest identified even-A isotope of thallium is ^{182}Tl ($T_{1/2} \approx 3$ s) known to undergo mainly $EC(\beta^+)$ decay [11,12]. For odd-A thallium isotopes, a systematic occurrence of the $1/2^+$ ground state and of a low-lying $9/2^-$ isomeric state was observed [3,7]. The first identification of the lightest odd-A thallium isotopes, ^{179}Tl, ^{181}Tl and ^{183}Tl, was based on α decay of an $9/2^-$ isomeric state [4,6,18]. The ground states of ^{179}Tl and ^{181}Tl have also been identified [6,12,18].

In this paper, we report on our experimental results concerning β decay of ^{183}Tl, which, according to systematics [3,7,18], is expected to be the main ground-state decay mode of this nucleus. The β decay of ^{183}Tl could be identified since the low-lying levels in ^{183}Hg have already been known from α-decay studies of ^{187}Pb [5], where two excited states, at 67 keV and at 275 keV, were observed, with probable spins and parities being ($3/2^-$ or $5/2^-$) and ($1/2^-$ or $3/2^-$), respectively. Then β decay of a $1/2^+$ state of ^{183}Tl can feed at least the higher level, thus providing the three γ transitions: 67 keV, 208 keV, and 275 keV.

2. Experimental

Our experiments were performed at the SARA cyclotron in Grenoble. A self-supporting metallic Sm target (2.1 mg/cm^2) containing 96.5% of ^{147}Sm was irradiated by a ^{40}Ca beam with a typical intensity of $2 \cdot 10^{11}$ pps. Reaction products recoiling out of the target were stopped in 1.4-bar pressurized helium and transported on NaCl (or $PbCl_2$) aerosols through a 1-mm diameter 12-m long capillary to a programmable tape-transport system used to carry the collected activity to a low-background counting position. The tape-transport system allowed us to make also a suitable selection of collection and counting time intervals. Measurements including γ multianalysis (counting periods 8×1 s), $\gamma-X$ and $\gamma-\gamma$ coincidences were performed. Further details concerning the experimental setup are given in Ref. [19].

Two beam energies were used in the present work, 196 MeV and 210 MeV at the middle of the target. We note that prior to our work, Toth et al. [8,9] employed the ^{147}Sm + ^{40}Ca reaction to produce very proton-rich isotopes of lead. In their experiments, the α activity of ^{183m}Tl was observed at bombarding energies of 194 MeV and 212 MeV, while there was no evidence for its production at 222 MeV. Thus, the beam energies used in the present work should provide an optimum yield of ^{183}Tl and ^{184}Tl via the (^{40}Ca,$p3n$) and (^{40}Ca,$p2n$) channels.This energy range selection was corroborated also by our statistical-model calculations made with the ALICE code [20].

3. Results and Discussion

*At 196 MeV

The γ spectra measured at the bombarding energy of 196 MeV give a firm evidence of the ^{184}Tl production. Two γ transitions in ^{184}Hg, 286 keV and 367 keV, known from in-beam spectroscopy studies [21] as well as from β-decay studies of ^{184}Tl [22] are clearly observed here (see Fig.1). An analysis of Hg $KX-\gamma$ coincidence data supports the assignment of these γ lines to $EC(\beta^+)$-decay of ^{184}Tl. Besides, an analysis of the time distribution of Hg KX-rays gives a half-life value of 10.0 ± 0.7 s, in a good agreement with $T_{1/2} = 11 \pm 1$ s known for ^{184}Tl [22,23]; this means also that, at the given bombarding energy, the yield of lighter (and presumably shorter-living) isotopes of Tl is low compared to that of ^{184}Tl. As the γ lines of 208 keV and, probably, 275 keV are seen in the lower spectrum on Fig.1, it indicates a production of ^{183}Tl; however, no clear coincidences between Hg KX-rays and these γ-events were obtained at this bombarding energy.

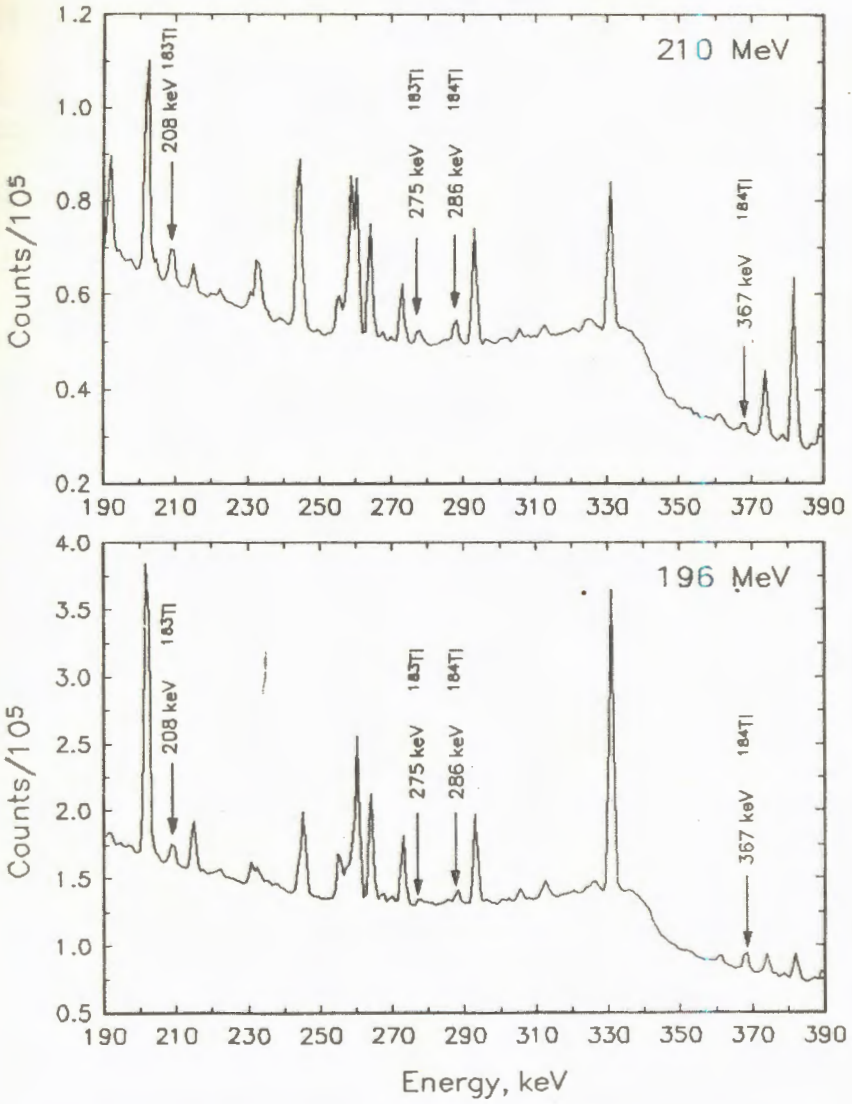

Fig.1. Comparison of the γ spectra measured at the ^{40}Ca beam energies of 210 MeV (upper spectrum) and 196 MeV (lower spectrum)

•At 210 MeV

As it could be expected, here the relative intensity of the 208 keV and 275 keV γ-lines has increased compared to that of the 367 keV γ-line of

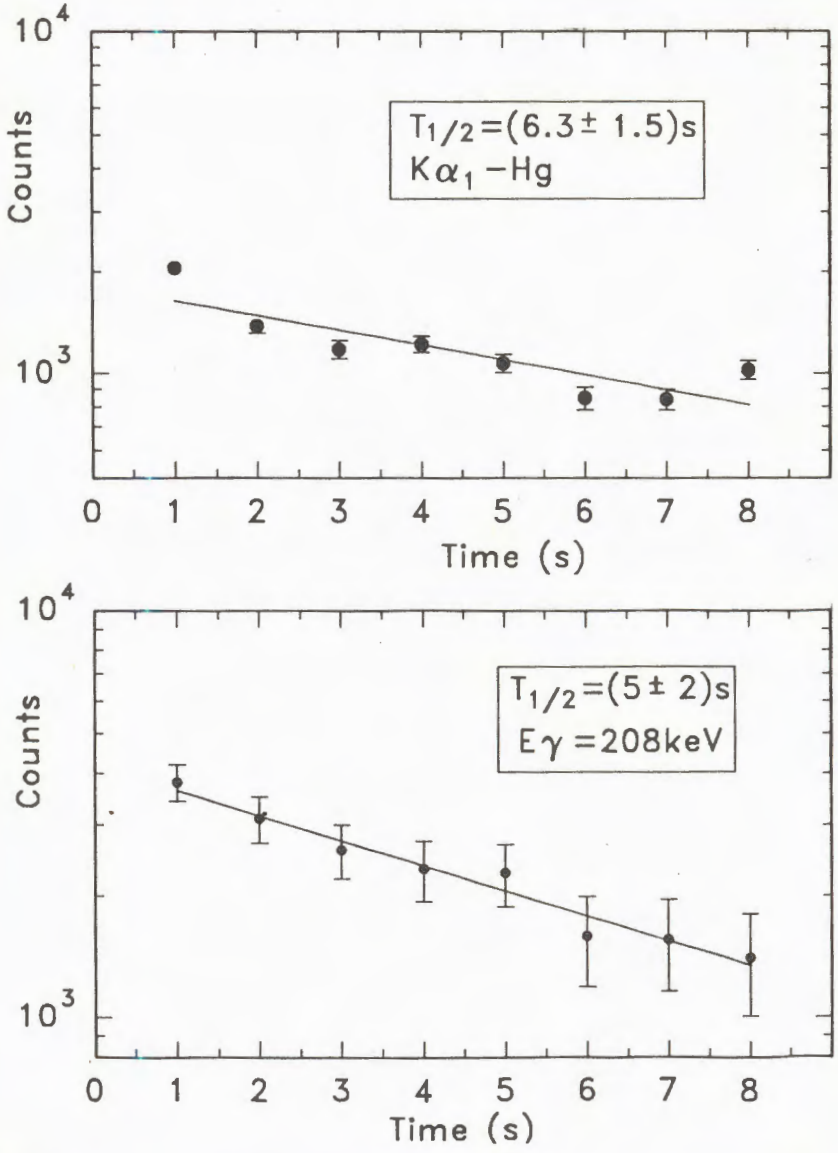

Fig.2. Decay curves of the $K_{\alpha 1}$–Hg X-rays and of the 208 keV γ-rays measured at the ^{40}Ca beam energy of 210 MeV

^{184}Tl (see Fig.1). A time analysis of the 208 keV γ-line and that of Hg KX-rays gives half-life values of 5 ± 2 s and 6.3 ± 1.5 s, respectively (Fig.2). These values are in agreement with the «gross» theory predictions of Taka-

hashi et al. [24] for ^{183}Tl and also with the $T_{1/2}$ value of 6.9 ± 1.4 s obtained for ^{183}Tl in a parallel investigation [12] performed by using a mass-separator facility and 1 GeV proton-induced spallation reactions on uranium and thorium targets.

To conclude, the ^{183}Tl isotope with $T_{1/2} = 5 \pm 2$ s was clearly produced in the ^{147}Sm(^{40}Ca,$p3n$) reaction and characterized via measuring its ground-state β decay. Yet the isotope of principal interest for us is the still unknown ^{180}Tl — the precursor of the $EC(\beta^+)$-delayed fission of ^{180}Hg — which can be produced by the ^{144}Sm(^{40}Ca, $p3n$) reaction. The sensitivity of the experiment to identify ^{180}Tl can be essentially improved by involving the detection of α particles and $\alpha-X$ coincidences. Whereas for ^{182}Tl and ^{184}Tl the α-decay branches are quite small, $b_\alpha < 5\%$ [11,12] and $b_\alpha \approx 2\%$ [23], respectively, ^{180}Tl is expected to show comparable branches for α and $EC(\beta^+)$ decays. Again, to increase the selectivity of the ^{180}Tl experiment, it is highly desirable to use a mass-separation technique, e.g., the IGISOL technique [25]. However, when applying this technique to heavy-ion-induced fusion-evaporation reactions, a serious difficulty arises due to the so-called «plasma effect» which causes a dramatic reduction of the efficiency [26]. A way out of this difficult situation can be provided by taking advantage of a huge difference between the angular distribution of beam particles and that of evaporation residues (EVRs) after passing a moderately thick target of a few mg/cm^2. This «shadow» method with a beam stop previously used by Sprouse et al. [27] for laser spectroscopy studies was applied in our recent IGISOL experiments at SARA with the ^{154}Sm + ^{40}Ar (217 MeV) reaction [28]. The beam stop allowed us to catch more than 96% of the ^{40}Ar particles whereas some 40% of EVRs missed the beam stop by virtue of their transverse momenta and could enter the He pressurized IGISOL chamber separated from the target/beam-stop chamber by a thin Havar window. In this way it was possible to decrease the «plasma effect» significantly and thus mass-separate the Hg-Au-Pt isotopes in the 188-189-190 mass chains. It is this combination of the «shadow» method with the IGISOL technique that shall be applied in our forthcoming studies of ^{180}Tl.

References

1. Toth K.S. — In: Future Directions in Studies of Nuclei Far From Stability (J.H.Hamilton et al., eds.). Amsterdam: North-Holland, 1980, p.71.
2. Toth K.S. et al. — In: Proc. Int. School-Seminar on Heavy Ion Physics, Dubna, October 3—12, 1989. JINR Report D7-90-142, Dubna, 1990, p.412.

3. Schmidt A.G. et al. — Phys.Lett., 1977, v.66B, p.133.
4. Schrewe U.J. et al. — Phys.Lett., 1980, v.91B, p.46.
5. Misaelides P. et al. — Z.Phys., 1981, v.A301, p.199.
6. Schneider J.R.H. et al. — Z.Phys., 1983, v.A312, p.21.
7. Coenen E. et al. — Phys.Rev.Lett., 1985, v.54, p.1783.
8. Toth K.S. et al. — Phys.Rev., 1987, v.C35, p.2330.
9. Toth K.S., Moltz D.M., Robertson J.D. — Phys.Rev., 1989, v.C39, p.1150.
10. Sellin P.J. et al. — Z.Phys., 1991, v.A338, p.245.
11. Bouldjedri A. et al. — Z.Phys., 1991, v.A339, p.311.
12. Bolshakov V.A. et al. — In: Proc. Int. Conf. on Exotic Nuclei, Foros, Crimea, USSR, October 1—5, 1991. Singapore: World Scientific, in press.
13. Lazarev Yu.A. et al. — Europhys.Lett., 1987, v.4, p.893.
14. Lazarev Yu.A. et al. — In: Proc. Int. School-Seminar on Heavy Ion Physics, Dubna, October 3—12, 1989. JINR Report D7-90-142, Dubna, 1990, p.208.
15. Lazarev Yu.A. et al. — In: Proc. Int. Conf. NFFS-6 + AMCO-9, Bernkastel-Kues, Germany, July 19—24, 1992. Bristol: IOP, in press.
16. Oganessian Yu.Ts., Lazarev Yu.A. — In: Treatise on Heavy-Ion Science (D.A. Bromley, ed.). N.Y.: Plenum Press, 1985, v.4, pp.1—251.
17. Béraud R. et al. — In: Heavy Ion Physics, Scientific Report 1989-1990, JINR, E7-91-75, Dubna, 1991, p.64.
18. Schneider J.R.H. — Thesis. Report GSI-84-3, Darmstadt, 1984.
19. Plantier A. et al. — Nucl. Instr. Meth. Phys. Res., 1987, v.B26, p.314.
20. Blann M. — Overlaid ALICE, A Statistical Model Computer Code Including Fission and Pre-Equilibrum Models. U.S. ERDA Report No.COO-3494-29, 1976.
21. Rud N. et al. — Phys. Rev.Lett., 1973, v.31, p.1421.
22. Cole J.D. et al. — Phys.Rev.Lett., 1976, v.37, p.1185.
23. Toth K.S. et al. — Phys.Lett., 1976, v.63B, p.150.
24. Takahashi K., Yamada M., Kondoh T. — At. Data Nucl. Data Tables, 1973, v.12, p.101.
25. Astier A. et al. — Nucl. Instr. Meth. Phys. Res., 1992, v.B70, p.233.
26. Äystö J. — Nucl. Instr. Meth. Phys. Res., 1989, v.B40/41, p.489.
27. Sprouse G.D. et al. — Phys.Rev.Lett., 1989, v.63, p.1463.
28. Astier A. et al. — In: Book of Abstracts of the 4th Workshop on Ion Guide Based Isotope Separation, Rydzyna, Poland, September 13—16, 1992.

Received on October 14, 1992

УДК 539.126.4

ГРАФИЧЕСКИЙ ИНТЕРФЕЙС СИСТЕМЫ PPDS НА ОСНОВЕ PAW

В.В.Иванов, Ю.В. Столярский

Описывается программный интерфейс, позволяющий представлять в графической форме результаты экспериментальных измерений и оценки различных характеристик физических реакций, хранящиеся в базе данных REACTIONS системы PPDS. Для визуализации экспериментальных данных используется пакет PAW.

Graphical Interface for PPDS System Based on PAW

V.V. Ivanov, Yu.V.Stolyarsky

The program interface allowing to display graphically experimental measurements results and evaluations of various physical reactions parameters stored in the REACTIONS database of PPDS system is described. PAW package is used for experimental data visualization.

1. Введение

Система баз данных физики частиц PPDS (Particle Physics Data System) [1] является удобным инструментом для сбора, оценки экспериментальных данных и обеспечения их доступности пользователям. Основу PPDS составляет система документальных и фактографических баз данных физики частиц промежуточных и высоких энергий. Документальные базы данных DOCUMENTS [2] и EXPERIMENTS [3] предоставляют исследователю возможность оперативного ретроспективного поиска ссылок на документы, содержащие данные о физике частиц. DOCUMENTS содержит описания публикаций оригинального и обзорного характера. В EXPERIMENTS собрана информация о текущих и завершенных экспериментах. Фактографическая база данных REACTIONS [4] содержит числовой материал результатов экспериментальных измерений и оценки различных характеристик физических реакций, опубликованных в периодической печати и каталогизированных в базе данных DOCUMENTS. Эти данные хранятся в виде таблиц, близких по форме к представлению, принятому в публикациях

Таблица 1[1)]

```
TITLE   AMMOSOV 76                NC 40A, 237
TITLE   RE                    P P --> PI- X
TITLE   P IN GEV   69.000
X-AXIS  PL(P=3,RF=LAB) IN GEV
Y-AXIS  (E(P=3,RF=LAB)/PI)*D(SIG)/D(PL(P=3,RF=LAB)) IN MB
 -0.40000      TO  -0.35000      0.           +-  0.
 -0.35000      TO  -0.30000      1.7000E-02   +-  1.2000E-02
 -0.30000      TO  -0.25000      4.7000E-02   +-  1.8000E-02
 -0.25000      TO  -0.20000      0.11000      +-  2.9000E-02
 -0.20000      TO  -0.15000      0.21100      +-  3.8000E-02
 -0.15000      TO  -0.10000      0.41300      +-  5.0000E-02
 -0.10000      TO  -5.0000E-02   0.77100      +-  6.8000E-02
 -5.0000E-02   TO  0.            0.98300      +-  7.8000E-02
 0.            TO  5.0000E-02    1.2400       +-  8.0000E-02
 5.0000E-02    TO  0.10000       1.7300       +-  0.11000
 0.10000       TO  0.15000       2.4100       +-  0.13000
 0.15000       TO  0.20000       2.6700       +-  0.14000
 0.20000       TO  0.25000       3.4100       +-  0.17000
 0.25000       TO  0.30000       3.5000       +-  0.18000
 0.30000       TO  0.35000       4.0700       +-  0.21000
 0.35000       TO  0.40000       4.2800       +-  0.22000
 0.40000       TO  0.45000       5.0000       +-  0.25000
 0.45000       TO  0.50000       5.0100       +-  0.27000
 END              18
```

[1)] Переменная представлена интервалом значений

(см. табл.1 и 2). Недостатком PPDS является отсутствие удобного графического интерфейса для визуализации указанной информации.

С другой стороны, удобным инструментом для анализа и визуализации экспериментальных данных является пакет PAW (Physical Analysis Workstation) [5], разработанный в CERN и широко используемый в настоящее время во многих физических центрах. PAW представляет собой интерактивную систему, включающую разнообразные средства представления и анализа данных. Большое внимание в PAW уделено реализа-

Таблица 2[1)]

```
TITLE   BREAKSTONE 86              ZP C30, 507
TITLE   THETA(P=3,RF=CM,P=1) IN DEG   50.000
TITLE   RE(Q=P)   P P --> P X
TITLE   RE(Q=K+)   P P --> K+ X
TITLE   RE(Q=PI+)   P P --> PI+ X
X-AXIS  PT(P=3,RF=CM) IN GEV
Y-AXIS  (SIG(Q=P)+SIG(Q=K+))/SIG(Q=PI+)
 1.5900                          0.73000      +-  3.0000E-02
 1.9500                          0.83000      +-  4.0000E-02
 2.3800                          0.72000      +-  6.0000E-02
 2.7600                          0.86000      +-  9.0000E-02
 3.3200                          0.72000      +-  0.12000
END                  5
```

[1)] Переменная представлена отдельными точками

ции удобного пользовательского интерфейса и графическому представлению данных.

Целью данной работы является создание интерфейса, позволяющего использовать возможности системы PAW для графического представления информации, хранящейся в базе данных REACTIONS.

2. Формат представления данных в базе данных REACTIONS

Каждый из документов в базе данных REACTIONS отображается в виде записи, которая содержит библиографическую ссылку, собственно числовые данные — результаты экспериментальных измерений, систематические ошибки и, возможно, оценки различных характеристик физических реакций.

Эти числовые данные хранятся в виде таблиц, содержащих значения исследуемой переменной, соответствующие им измеренные значения (экспериментальные точки) и ошибку измерения. Таблицы 1 и 2 содержат результаты поиска в базе данных REACTIONS, сохраненные с помощью команды DOCU в режиме MODD = 2 [6]. В табл. 1 исследуе-

мая переменная представлена в виде интервала значений (значение 1 ТО значение 2), а в табл. 2 — в виде отдельных точек.

3. Реализация

Описываемые здесь процедуры реализованы в среде VAX VMS 5.4. В системе PPDS при работе с базой данных REACTIONS выбранные по запросу пользователя документы могут быть сохранены с помощью команды DOCUment в файле RD.DOC. Этот файл используется в качестве исходного для извлечения интересующих пользователя таблиц и подготовки вспомогательных файлов, с которыми в дальнейшем работает PAW. Реализовано это в процедуре EXTR, которая читает файл RD.DOC, выбирает помеченные пользователем таблицы, создает файл PPDS.KUMAC и вспомогательные файлы DAT001.RD ... DAT00n.RD (n равно числу помеченных таблиц, в данной реализации до 10). Пользователь помечает интересующие его таблицы, помещая в режиме редактирования символ «*» в первый байт строки, предшествующей началу таблицы в файле RD.DOC (см. табл. 3).

Полученный в результате выполнения процедуры EXTR файл PPDS.KUMAC содержит макрокоманды «001» ... «00n» (по числу ото-

Таблица 3[1)]

```
*       .           .
TITLE   BREAKSTONE 86              ZP C30, 507
TITLE   THETA(P=3,RF=CM,P=1) IN DEG   50.000
TITLE   RE(Q=P)    P P --> P X
TITLE   RE(Q=K+)    P P --> K+ X
TITLE   RE(Q=PI+)    P P --> PI+ X
X-AXIS  PT(P=3,RF=CM) IN GEV
Y-AXIS  (SIG(Q=P)+SIG(Q=K+))/SIG(Q=PI+)
 1.5900                          0.73000      +-   3.0000E-02
 1.9500                          0.83000      +-   4.0000E-02
 2.3800                          0.72000      +-   6.0000E-02
 2.7600                          0.86000      +-   9.0000E-02
 3.3200                          0.72000      +-   0.12000
 END                 5
```

[1)] Таблица, помеченная для выборки в файле RD.DOC

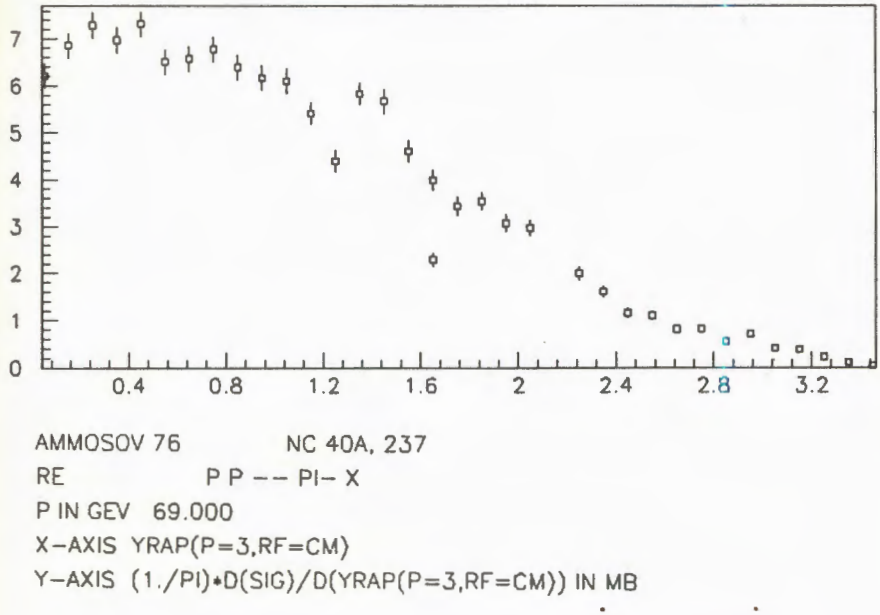

Рис.1. Изображение, полученное с помощью команды exec PPDS#00n

бранных для графического отображения таблиц).Для визуализации отобранных таблиц можно воспользоваться графическим терминалом VAX либо перенести файлы PPDS.KUMAC и DAT001.RD ... DAT00n.RD на дискету и затем работать с PAW на персональном компьютере [7]. В ответ на приглашение PAW следует ввести команду

PAW> exec PPDS#00n

(n — порядковый номер помеченной таблицы) для получения графического изображения в виде, представленном на рис. 1. Для отображения таблицы на весь экран (рис.2) следует использовать параметр макрокоманды Zoom:

PAW> exec PPDS#00n Zoom

Изображение на рис.1 содержит все подписи к таблице, включая названия осей. На рис.2 подписи отсутствуют, так как в большинстве случаев (например, при использовании рисунка в качестве иллюстрации для статьи) пользователь вряд ли будет удовлетворен их качеством. Поэтому ему предлагается, используя возможности PAW, выбрать более

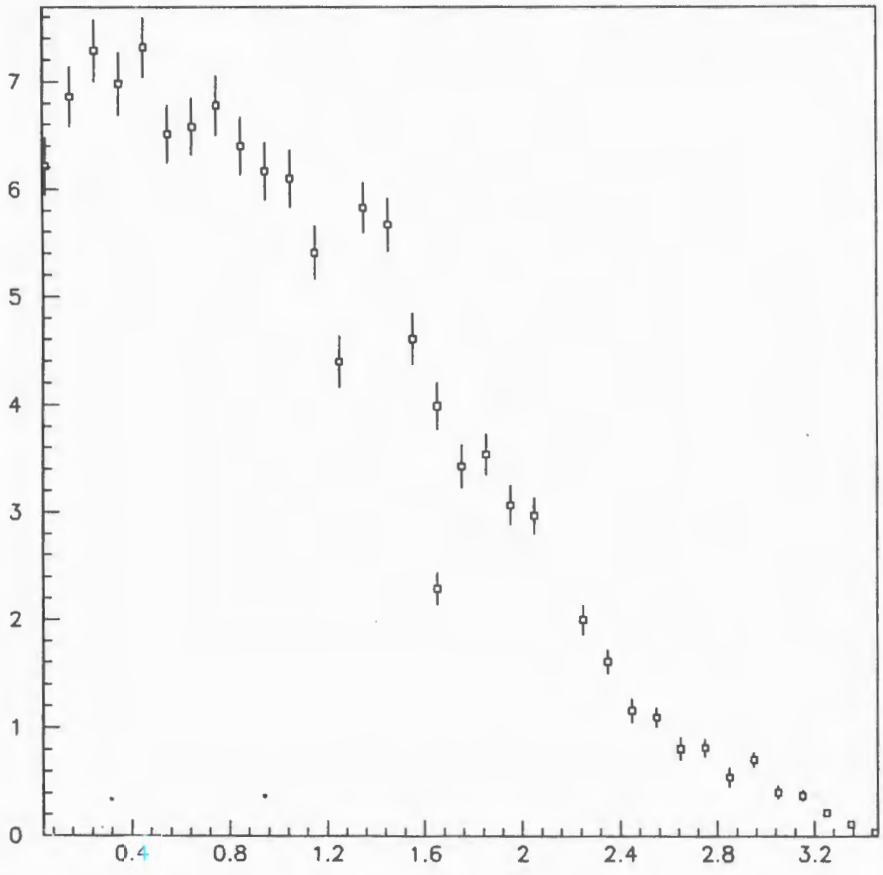

Рис.2. Изображение, полученное с помощью команды exec PPDS#00n Zoom

подходящие фонты, размеры шрифтов, аббревиатуры и т.п. и внести соответствующие изменения в файл PPDS.KUMAC.

4. Заключение

Предлагаемый интерфейс повышает эффективность работы исследователя с системой PPDS, предоставляя ему возможность графического отображения и визуальной оценки в интерактивном режиме результатов экспериментальных измерений, содержащихся в базе данных REACTIONS.

Литература

1. Rosenfeld A.H. — Ann. Rev. Nucl. Sci.,1975, vol.25., p.555.
2. Yost G.D. et al. — A Guide to Data in Elementary Particle Physics, LBL-90, 1986.
3. Wohl C.G. et al. — Current Experiments in Elementary Particle Physics, LBL-91, 1987.
4. Fox G., Read B., Rittenberg A. — Reaction Data File Encoding Manual. Particle Data Group (LBL, Tech., Durham, RAL), 1978.
5. Brun R. et al. PAW — Physics Analysis Workstation. The Complete Reference. CERN, Switzerland, 1991.
6. Richards D.R. — BDMS User's Manual, LBL-4683,1978.
7. Ivanov V.V., Khasanov A.M., Pal'chik V.V. — JINR Preprint E11-92-248, Dubna, 1992.

Рукопись поступила 22 сентября 1992 года.

Краткие сообщения ОИЯИ 6[57]-92 *JINR Rapid Communications No.6[57]-92*
УДК 524.8 + 530.145

«КВАНТОВОЕ» ВРЕМЯ В КОСМОЛОГИИ ФРИДМАНА

В.Н. Первушин

Предлагается альтернативное определение «наблюдаемого» времени в космологии Фридмана исходя из условия сохранения «квантовой» энергии Вселенной, которая вычисляется проекцией полного действия ОТО на решения уравнений связи. Физическим следствием такого определения времени может быть периодическая структура Вселенной.

Работа выполнена в Лаборатории теоретической физики ОИЯИ.

«Quantum» Time in the Friedmann Cosmology

V.N. Pervushin

The alternative definition of the «observable» time in the Friedmann cosmology is supposed. This definition is based on the conservation law of the «quantum» energy of the Universe, which is determined by the projection of the total action of the Einstein theory onto the explicit solutions of the constraint equation. The physical consequence of this definition of the time can be the periodic structure of the Universe.

The investigation has been performed at the Laboratory of Theoretical Physics, JINR.

1. Определение наблюдаемого времени является одним из центральных моментов космологии Фридмана. В настоящей заметке мы хотели бы обратить внимание на возможность его альтернативного определения — введения нового времени «квантового наблюдателя». Будем исходить из построения гамильтониана ОТО на решениях уравнений связи [1] в приближении замкнутой Вселенной Фридмана.

2. Рассмотрим теорию Эйнштейна в приближении изотропного замкнутого пространства. Действие теории с учетом полных производных имеет вид

$$W = V_0(r_0)\left\{\int_0^T dt\left[(\dot{\mu}P - \alpha\mathcal{H} - \frac{\dot{P}}{2}\right]\right\} \quad \left(\dot{P} = \frac{dP}{dt}\right), \tag{1}$$

$$\mathcal{H} = a^3\left[-\frac{1}{2}\frac{P^2}{\kappa_3^2\dot{a}^6} + T_0^0 - \frac{1}{2\kappa_3^2 a^2 r_0^2}\right] \quad \left(\kappa_3^2 = \frac{\kappa^2}{6}\right), \tag{2}$$

где μ есть логарифмическая шкала пространства ($\mu = \ln a$), P — ее канонический импульс, $V_0(r_0) = 2\pi^2 r_0^3$ — объем пространства постоянной кривизны, T_0^0 — однородная часть плотности энергии материи, α — шкала времени.

Классическая теория (1) описывается тремя уравнениями на α, P, μ:

$$\mathcal{H} = 0, \ \frac{1}{\alpha}\dot{\mu} = -\frac{\kappa_3^2 P}{a^3}, \ \frac{1}{\alpha}\dot{P} = -\frac{d}{d\mu}\mathcal{H}, \tag{3}$$

инвариатными относительно репараметризации времени $t \to t'(t)$. Первое из них — связь первого рода, а третье тождественно первым двум. Данные уравнения позволяют однозначно определить инвариат теории — собственное время

$$dT_F = \alpha_{\pm} dt = -\frac{d\mu a^3}{\kappa_3^2 P_{(\pm)}}, \ P_{(\pm)} = \mp\frac{a^3}{\kappa_3}\left[2T_0^0 - \frac{1}{\kappa_3^2 a^2 r_0^2}\right], \tag{4}$$

являющееся наблюдаемым временем в космологии Фридмана, относительно которого описывается эволюция шкалы t.

3. Имеются два противоположных подхода к квантованию теории (1): а) общепринятый [2], когда все компоненты метрики α, a трактуются динамическими полями и связи первого рода налагаются на волновую функцию, в результате чего возникает уравнение Уиллера — Де Витта, $\mathcal{H}\Psi = 0$; и б) минимальный [1], когда квантуется лишь действие (1), рассматриваемое на явных решениях связей первого рода

$$W_{(\pm)}^{\text{Min}} = V_0(r_0)\int_0^T dt\left(\dot{\mu}P_{(\pm)} - \frac{\dot{P}_{(\pm)}}{2}\right). \tag{5}$$

С точки зрения принципа соответствия динамике классической теории, предпочтительнее второй метод, где остается граничная динамика шкалы с нетривиальной волновой функцией

$$\Psi^{\text{Min}}(a) = A^{(+)}e^{iW_{(+)}(a)} + A^{(-)}e^{iW_{(-)}(a)}. \tag{6}$$

Отождествляя эту волновую функцию со спектральным представлением

$$W_{(\pm)}^{\text{Min}} = \mp E_{\text{Univ.}} T_Q(a), \ \frac{dE_{\text{Univ}}}{dT_Q} = 0, \tag{7}$$

получим еще одно определение времени «квантового наблюдателя». Отметим, что минимальный подход к квантованию может быть использо-

ван при квантовании модели релятивистской частицы, которая возникает из (1) заменой $\mu \to x^0$, $P_{(\pm)} \to \mp\sqrt{P_i^2 + m^2}$. В этой модели уравнение Фридмана (4) представляет собой преобразование Лоренца при переходе от времени покоя T_F к времени движущегося наблюдателя x^0, которое совпадает с квантовым временем спектрального представления (7).

4. Сравним два времени T_F и T_Q для Вселенной, заполненной «излучением» и «пылью» [3],

$$T_0^0(a) = \frac{1}{V_0(r_0)}\left[\frac{\varepsilon_R}{2r_0 a^4} + \frac{M_d}{a^3}\right]. \tag{8}$$

Решая уравнения (4) и (7), получим следующие выражения для масштаба a и времен T_Q, T_F как параметров от конформного времени η:

$$E_{\text{Univ}} = \frac{\varepsilon_R}{2r_0} + \frac{\kappa_3^2 M_d^2}{4\pi^2 r_0} \equiv \frac{\pi^2}{4_0\kappa_3^2}\left[\tilde{\varepsilon} + \tilde{M}^2\right], \quad \tilde{M} = \frac{\kappa_3^2 M_d}{2\pi^2}, \tag{9}$$

$$T_Q(\eta) = r_0\left(\eta + \frac{\tilde{M}}{\sqrt{\tilde{M}^2 + \tilde{\varepsilon}}}\operatorname{Sin}\eta\right); \quad a(\eta) = \frac{1}{r_0}\left(\tilde{M} - \sqrt{\tilde{M}^2 + \tilde{\varepsilon}}\operatorname{Cos}\eta\right), \tag{10}$$

$$T_F(\eta) = \tilde{M}\eta + \sqrt{\tilde{M}^2 + \tilde{\varepsilon}}\operatorname{Sin}\eta. \tag{11}$$

Если доминирует излучение, $\tilde{M} = 0$, то «квантовое» время T_Q совпадает с конформным ($T_Q = r_0\eta$) и меняется в бесконечных пределах, тогда как $T_F = \sqrt{\tilde{\varepsilon}}\operatorname{Sin}\eta$ меняется в конечном интервале. Если излучение отсутствует, то времена T_F и T_Q совпадают с точностью до коэффициента $\tilde{M}/r_0$, имеющего порядок 1 для параметров нашей Вселенной. Пыль (9) находится в состоянии покоя, и принцип соответствия, т.е. требование, чтобы классическое время совпадало с квантовым временем спектрального представления (7), (8), напоминает условие перенормировки эффективного ньютоновского самодействия массы Вселенной: $\kappa_3^2 M_d^2/2\pi^2 r_0 = M_d$, или $\tilde{M} = r_0$ (т.е. — простейший вариант уравнения Швингера — Дайсона).

Все эти результаты справедливы как для случая плоской Вселенной, так и для пространства Лобачевского. Мы хотим здесь подчеркнуть лишь одно обстоятельство. Если наблюдатель видит «квантовое» время (10), то решение вопроса о критической плотности становится еще болеее неопределенным, поскольку в уравнение для критической плотности вхо-

дит классическая «ненаблюдаемая» постоянная Хаббла, которая может резко отличаться от «наблюдаемой».

В частности, из уравнений (10), (11) видно, что даже в случае бесконечно малой плотности излучения по сравнению с плотностью пыли $\tilde{\varepsilon} = 2\gamma\tilde{M}^2$, $2\gamma << 1$, отношение классической (H_F) и квантовой (H_Q) постоянных Хаббла осциллирует с периодом, не зависящим от γ:

$$\frac{H_F}{H_Q} = \frac{(1 + \cos\eta) - \gamma\cos\eta}{(1 + \cos\eta) + \gamma\cos\eta}. \qquad (12)$$

С другой стороны, открытая недавно крупномасштабная структура Вселенной, для объяснения которой используют осциллирующую постоянную Хаббла [4], может свидетельствовать, в контексте «квантового» определения наблюдаемого времени, о том, что мы живем в замкнутой осциллирующей Вселенной.

Автор хотел бы поблагодарить А.В.Ефремова, А.А.Изместьева, Э.А.Кураева за обсуждения и критические замечания. Автор благодарен Я.А.Смородинскому за постоянный интерес к работе.

Литература

1. Pervushin V.N. — Nuovo Cimento, 1985, vol.8, No.8, p.1;
   Nguyen Suan Han, Pervushin V.N. — Fortsch.Phys. 1989, vol.37, p.611.
2. Faddeev L.D., Popov V.N. — Phys.Lett., 1967, B95, 29;
   Фаддеев Л.Д., Попов В.Н. — УФН, 1973, 11, p.427.
3. Бурланков Д.Е., Дудышев В.М., Кочнев А.А. — ЖЭТФ, 1984, vol.87, с.705.
4. Hill C.T., Steinhardt P.J., Turner M.S. — Preprint FERMI-PUB-90/127T, Batavia, 1990;
   Reasenberg R.D. et al. — Astrophys. J., 1979, vol.234, p.L219-221.

Рукопись поступила 9 октября 1992 года.

УДК 539.12.01.

THE REALIZATION OF NAMBU — JONA-LASINIO TYPE MODEL ON PHYSICAL FIELDS

A.N.Vall*, V.M.Leviant*, A.V.Sinitskaya*

Method of dynamical mapping for the Heisenberg fields onto physical fields in the four fermion interaction Hamiltonian (nonrelativistic variant of NJL model) is used to calculate: energy of physical vacuum, one-particle excitation energy spectrum, wave function and mass of the bound state of two excitations.

Реализация модели Намбу — Йона-Лазинио на физических полях

А.Н.Валл, В.М.Левиант, А.В.Синицкая

Методом динамического отображения гейзенберговских полей на физические поля для гамильтониана с четырехфермионным взаимодействием вычислены: энергия физического вакуума, энергетический спектр одночастичных возбуждений, волновая функция и масса связанного состояния двух возбуждений.

The investigation of the bound-state problem in the frame of quantum field theory may be done by using, at least, two methods. The first one is based on the search for self-consistene solutions of Schwinger — Dyson (SD) equation for the full propagator of interacting particles and Bete — Solpiter (BS) equation for the vertex Green function (see [1] and references there). Another one deals straightly with the state vectors [2,3].

The Nambu and Jona-Lasinio (NJL) model [4] fits from any points of view to study the possibility of producing the bound states. Though originally it was solved by the Green function method, its resemblance to the superconductive type models allows one to use both the first and the second methods.

In the present paper we consider the most simple nonrelativistic variant of NJL model, more closely related to the nonlinear Heisenberg theory [5], to demonstrate the advantages of the second approach. We find the representation for the Heisenberg fields via «physical» fields (dynamical

*Department of Theoretical Physics, Irkutsk State University, Irkutsk, 664003, Russia

mapping [6]) describing the collective degrees of freedom (excitations). These excitations can form bound states, and the momenta of the excitations turn out to be strictly correlated between each other. The exact expression for the wave function of the bound states is written out, but for the energy (mass) of the bound states we obtain nonlinear integral equation, the type of equation for the energy gap. The spectrum of the one-particle excitations and the energy of the ground states have been found as well. As a conclusion we show briefly the correspondence of these two methods.

The physical states, by the definition, are the states upon which a Hamiltonian is diagonal in a weak sense:

$$\langle \mathbf{k}|H|\mathbf{k}'\rangle = \langle \mathbf{k}|\int d^3q B^+(\mathbf{q})B(\mathbf{q})E(\mathbf{q})|\mathbf{k}'\rangle + W_0, \qquad (1)$$

where $B(\mathbf{k})|0\rangle = 0$, $|\mathbf{k}\rangle = B^+(\mathbf{k})|0\rangle$ and

$$[H, B^+(\mathbf{k})]|0\rangle = E(\mathbf{k})|0\rangle$$

and $E(\mathbf{k})$- energy spectrum of physical particles.

Consider now the Hamiltonian of our model:

$$H = \int d^3x \left[\psi^+_\alpha(x)\,\varepsilon(\nabla)\,\psi_\alpha(x) + \frac{\lambda}{4}\chi^+(x)\,\chi(x)\right], \qquad (2)$$

where α is spin index running over 1,2,$\varepsilon(\nabla)$ is energy spectrum of free fermions, defined by the condition

$$\varepsilon(\nabla)\, e^{ikx} = \varepsilon(\mathbf{k})\, e^{ikx}, \qquad (3)$$

and*

$$\chi(x) = \varepsilon_{\alpha\beta}\psi_\alpha(x)\psi_\beta(x),\ \chi^+(x) = \varepsilon_{\alpha\beta}\psi^+_\beta(x)\psi^+_\alpha(x).$$

Let us formulate the problems we want to solve demonstrating the efficiency of the physical field representation.

- i) Connection of the Heisenberg fields ψ with physical ones φ, i.e., dynamical mapping ψ on φ.
- ii) Stability of vacuum and its energy.
- iii) Spectrum of one particle physical state $E(\mathbf{k})$.
- iv) Spectrum and wave function of two-particle state.
- v) Correspondence with the usual approach.

We will give the solutions of the outlined problems following the list.

i) In our case the dynamical mapping has the form:

$$\psi_\alpha(x) = u_0\phi_\alpha(x) + v_0 e^{i\alpha(x)}\,\varepsilon_{\alpha\beta}\phi^+_\beta(x),$$

*$\varepsilon_{12} = -\varepsilon_{21}$, $\varepsilon_{\alpha\beta}\varepsilon_{\alpha\gamma} = \delta_{\beta\gamma}$

$$\psi_\alpha^+(x) = u_0\phi_\alpha^+(x) + v_0 e^{-i\alpha(x)}\varepsilon_{\alpha\beta}\phi_\beta(x), \tag{4}$$

where $u_0^2 + v_0^2 = 1$, with $\phi_\alpha(x)$ defined as

$$\phi_\alpha(x) = \frac{1}{(2\pi)^{3/2}}\int d^3k g(\mathbf{k}) e^{i\mathbf{kx} - iE(\mathbf{k})t} A_\alpha(\mathbf{k}), \tag{5}$$

$$\left\{A_\alpha(\mathbf{k}), A_\beta^+(\mathbf{q})\right\} = \delta_{\alpha\beta\delta}(\mathbf{k} - \mathbf{q}), \tag{6}$$

$E(\mathbf{k})$ is unknown yet excitation spectrum of $A_\alpha^+(\mathbf{k})$. The physical meaning of $g(\mathbf{k})$ is clear enough, it is one-particle wave function and it cannot be calculated in the frames of this model (free parameter).

ii) The vacuum is now defined with respect to the physical fields $A_\alpha^+(\mathbf{k})$:

$$A_\alpha(\mathbf{k})|0\rangle = 0. \tag{7}$$

Consider the action of the Hamiltonian (2) on this vacuum. We have:

$$H|0\rangle = \text{const}_0|0\rangle + \Delta H(2)|0\rangle. \tag{8}$$

$\Delta H(2)$ being expressed in terms of the creation operators $A_\alpha^+(\mathbf{k})$ has the form

$$\Delta H(2) = u_0 v_0 \varepsilon_{\alpha\beta}\int d^3x \phi_\alpha^+(x)\left(\varepsilon(\ ) + \frac{\lambda}{2v^*}\right) e^{i\mathbf{k}_0\mathbf{x}}\phi_\beta^+(x) =$$

$$= \int d^3k \dot{D}(\mathbf{k})\varepsilon_{\alpha\beta}A_\alpha^+\left(\frac{\mathbf{k}_0}{2} - \mathbf{k}\right) A_\beta^+\left(\frac{\mathbf{k}_0}{2} + \mathbf{k}\right), \tag{9}$$

where

$$D(\mathbf{k}) = u_0 v_0 g\left(\mathbf{k} - \frac{\mathbf{k}_0}{2}\right)\bar{g}\left(\mathbf{k} + \frac{\mathbf{k}_0}{2}\right)\left(\varepsilon\left(\mathbf{k} - \frac{\mathbf{k}_0}{2}\right) + \frac{\lambda}{2V^*}\right)$$

$$\frac{1}{V^*} = \frac{1}{(2\pi)^3}\int d^3k |g(\mathbf{k})|^2.$$

Thus, as it follows from (8), the nonexcited state $|0\rangle$ is not an eigenstate of the Hamilonian (2), and the $\Delta H(2)$ term is the source of the nonstationarity of $|0\rangle$. This term describes correlated fermion couple of excitations, moving with the momentum $\mathbf{k}_0$. The physical meaning of the relation (8) is that it points to the existence of energy exchange between the couple and the system of fermions. In order to account this exchange one has to input the term describing the couple into the initial Hamiltonian. So, in the relation

(8) we transfer $\Delta H(2)$ to the left part, thus, redefining the Hamiltonian and taking as a physical Hamiltonian the quantity H_p equal to

$$H_p = :H - \Delta H(2):, \tag{10}$$

where the normal ordering is referred to the Heisenberg fields. If $\Delta H(2) =: \Delta H(2):$ + const, then

$$H_p|0\rangle = H|0\rangle - \Delta H(2)|0\rangle + \text{const}|0\rangle,$$

$$H_p|0\rangle = W_0|0\rangle, \quad W_0 = \text{const}_0 + \text{const}, \tag{11}$$

$$\text{const}_0 = 2\nu_0^2 \frac{V}{V^*}\left(\varepsilon(\mathbf{k}_0) + \frac{\langle \mathbf{k}^2\rangle}{2m} + \frac{\lambda}{2V^*}\right),$$

$$\text{const.} = -\frac{4u_0^4\nu_0^2}{V^*}\int d^2x\, e^{-i\alpha(x)}\varepsilon(\nabla)e^{i\alpha(x)} - 4\frac{V}{V^*}u_0^2\nu_0^2\left(\frac{\langle \mathbf{k}^2\rangle}{2m} + \frac{\lambda}{2V^*}\right). \tag{12}$$

Here V is space volume, and

$$\langle \mathbf{k}^2\rangle = \frac{\int d^3k\mathbf{k}^2|g(\mathbf{k})|^2}{\int d^3k|g(\mathbf{k})|^2}. \tag{13}$$

Consequently, after substitution of the counterterm $\Delta H(2)$ into the Hamiltonian (2) the non-excited state $|0\rangle$ becomes stationary, with the energy W_0.

iii) It is easy to see from (1) that this redefinition of the Hamiltonian does not change the one-particle excitation spectrum $E(\mathbf{k})$, the value of which is readily derived using eqs. (1), (2), (4)—(6)

$$E(\mathbf{k}) = |g(\mathbf{k})|^2\left(u_0^2\varepsilon(\mathbf{k}) - \nu_0^2\varepsilon(\mathbf{k} - \mathbf{k}_0) - \lambda\frac{\nu_0^2}{V^*}\right). \tag{14}$$

iv) Let us now find how the Hamiltonian H_p acts on a state composed of two excitations with momenta $\mathbf{k}$ and $\mathbf{q}$

$$H_pA_\alpha^+(\mathbf{k})A_\beta^+(\mathbf{q})|0\rangle = (W_0 + E(\mathbf{k}) + E(\mathbf{q}))A_\alpha^+(\mathbf{k})A_\beta^+(\mathbf{q})|0\rangle +$$

$$+\lambda\frac{g(\mathbf{k})g(\mathbf{q})}{(2\pi)^3}\int d^3x e^{i(\mathbf{k}+\mathbf{q})\mathbf{x}}\phi_\alpha^+(x)\phi_\beta^+(x)0\rangle. \tag{15}$$

If the excitations do not interact with each other, the last term in the sum (15) should vanish. Then, this two-particle excitation will be an eigenstate of the Hamiltonian H_p with the energy being equal to the sum of both exci-

tation energies. That is the case for two excitations with a total spin 1 (symmetrical over $\alpha\beta$). Putting $\mathbf{k} = -\mathbf{q}$ in equation (15) we have:

$$H_p\hat{A}(\mathbf{k})|0\rangle = (W_0 + E(\mathbf{k}) + E(-\mathbf{k}))\hat{A}(\mathbf{k})|0\rangle + \\ + \lambda \frac{|g(\mathbf{k})|^2}{(2\pi)^3} \int d^3q |g(\mathbf{q})|^2 \hat{A}^+(\mathbf{q})|0\rangle,$$

$$\hat{A}^+(\mathbf{k}) = \varepsilon_{\alpha\beta} A^+_\alpha(\mathbf{k}) A^+_\beta(-\mathbf{k}). \tag{16}$$

Taking the wave packet $\hat{A}^+$:

$$\hat{A}^+ = \int d^3k G(\mathbf{k}) \varepsilon_{\alpha\beta} A^+_\alpha(\mathbf{k}) A^+_\beta(-\mathbf{k}) \tag{17}$$

and demanding for it to be an eigenstate of the Hamiltonian

$$H_p\hat{A}^+|0\rangle = (W_0 + \mu)\hat{A}^+|0\rangle \tag{18}$$

we come to the equation on the wave function $G(\mathbf{k})$ and the energy of this state μ:

$$\int d^3k \left[G(\mathbf{k}) \left(E(\mathbf{k}) + E(-\mathbf{k}) - \mu\right) + \gamma_0 |g(\mathbf{k})|^2 \right] \hat{A}^+(\mathbf{k})|0\rangle = 0, \tag{19}$$

where

$$\gamma_0 = \frac{\lambda}{(2\pi)^3} \int d^3q |g(\mathbf{q})|^2 G(\mathbf{q}). \tag{20}$$

Hence follows the only solution for $G(\mathbf{k})$:

$$G(\mathbf{k}) = \frac{\gamma_0 |g(\mathbf{k})|^2}{\mu - E(\mathbf{k}) - E(-\mathbf{k})}. \tag{21}$$

Substitution of this solution into the relation (20) leads to the equation for μ:

$$1 = \frac{\lambda}{(2\pi)^3} \int d^3k \frac{|g(\mathbf{k})|^4}{\mu - E(\mathbf{k}) - E(-\mathbf{k})}. \tag{22}$$

Let us rewrite (22) in the form

$$1 = -\frac{\lambda M}{(2\pi)^3} \int d^3k \frac{|g(\mathbf{k})|^2}{\mathbf{k}^2 + \delta^2}. \tag{23}$$

This equation determines δ^2 as a function of λ. We will seek solution of (23) in the form of asymptotic series

$$\delta^2 = a_0 + a\lambda + \frac{c_1}{\lambda} + \frac{c_2}{\lambda^2} + \ldots, \tag{24}$$

$$\mathbf{k}^2 + \delta^2 = \lambda\left(a + \frac{\mathbf{k}^2 a_0}{\lambda} + \frac{c_1}{\lambda^2} + \frac{c_2}{\lambda^3} + \ldots\right).$$

Using the series conversion formulae we can derive

$$\frac{\lambda}{\mathbf{k}^2 + \delta^2} = \frac{1}{a + b\varepsilon + c\varepsilon^2 + \ldots} = \frac{1}{a}\left[1 - \frac{b}{a}\varepsilon + \left(\frac{b^2}{a^2} - \frac{c}{a}\right)\varepsilon^2 + \ldots\right], \tag{25}$$

where $\varepsilon = 1/\lambda$, $b = a_0 + \mathbf{k}^2$, $c = c_1$, ect. Substituting the series expansion (25) into the equation (23), collecting the terms of the same power over λ and equating them to zero, we will obtain the chain of relations defining the coefficients a_0, a, c_1, ect. Straightforward calculations give the following result:

$$a_0 = -\langle \mathbf{k}^2 \rangle, \quad a = -\frac{M}{V^*},$$

$$c_1 = -\frac{m}{V^*}\frac{\int d^3k\,|g(\mathbf{k})|^2(\mathbf{k}^2 - \langle \mathbf{k}^2 \rangle)^2}{\int d^3k\,|g(\mathbf{k})|^2} \equiv -\frac{M}{V^*}\sigma \tag{26}$$

from which we receive the asymptotic series for δ^2 and μ:

$$\delta^2 = -\langle \mathbf{k}^2 \rangle - \frac{M}{V^*}\lambda - \frac{V^*}{M}\cdot\frac{\sigma}{\lambda} + \ldots,$$

$$\mu = -\frac{\delta^2}{M} + 2E(0), \quad 2E(0) = \left(\frac{\mathbf{k}_0^2}{2m} + \frac{\lambda}{V^*}\right)\cdot\left(\frac{m}{M} - 1\right). \tag{27}$$

The magnitude of M is determined from the vacuum energy W_0 minimization condition over the rotation parameters u_0, v_0 and $\alpha(x)$.

From the relations (26) and (27) it is easy to see that the non-perturbative and singular with respect to the coupling constant λ contributions into the energy are defined by the dispersion σ over momentum distribution $|g(\mathbf{k})|^2$ inside the excitation.

In order to show the correspondence with the Green functions' method we will just write out the Shwinger — Dyson and Bete — Solpiter type equations. The word «type» means that we deal with the physical fields, and to pass to the standard SD and BS equations one has to substitute the Heisenberg fields instead of the physical ones using the inverse dynamical

mapping. It is not necessary for our aim to do that, so we leave it for reader to do.

The Green functions for the physical fields ϕ are, by the definition, the vacuum expectation values of the T products of them. For the total two point Green function we have:

$$G^{P}_{\alpha\beta}(\mathbf{x}, t;0) = \langle 0 | T\left(\phi_{\alpha}(x)\, \phi^{+}_{\beta}(0)\right) | 0\rangle, \tag{28}$$

here we have put the second argument to zero. Its manifest form can be calculated directly, using (5), from which it is easy to find the equation:

$$\left(\frac{\partial}{\partial t} + iE(\nabla)\right) G^{P}_{\alpha\beta}(\mathbf{x}, t;0) = \delta_{\alpha\beta}\Delta^{(4)}(\mathbf{x}, t). \tag{29}$$

The equation for the vertex Green function follows from the Heisenberg equation on $\phi_{\alpha}(x)$ using eq.(29):

$$E(\nabla)G^{P}_{\alpha\beta}(\mathbf{x},t;0) = \langle 0 | T\left(\left[\phi_{\alpha}(\mathbf{x},t),\mathbf{H}\right], \phi^{+}_{\beta}(0) | 0\rangle\right). \tag{30}$$

As has been said above, the usual SD and BS equations follow from (29) and (30) under the transition $\phi \to \psi$.

For the conclusion we would like to point to that the physical fields representation method can be generalized for the relativistic case, and next paper will be devoted to this generalization.

Aknowledgements. The authors are grateful to Profs. D.V.Shirkov, V.N.Pervushin and Yu.L.Kalinovsky for the crucial comments, useful discussions and support.

References

1. Pervushin V.N. et al. — Fortschr.Phys., 1990, 38, 5, p.333; Kalinovsky Yu.L., Kaschluhn L., Pervushin V.N. — Fortschr.Phys., 1990, 38, 5, 353; Kalinovsky Yu.L. et al. — Few-Body Sys., 1991, 10, p.87.
2. Schveber S.S. — An Introduction to Relativistic Quantum Field Theory., Elmsford, N.Y., 1961 (Russian translation, Moscow, 1963).
3. Fujita T., Ogura A., Tomachi T. — Preprint NUP-A-91-11; Fujita T. — Preprint NUP-A-91-12; Tomachi, T.Fujita — Preprint NUP-A-91-10.
4. Nambu Y., Jona-Lasinio G. — Phys. Rev., 1961, 122, p.345; ibid., 1961, 124, p.246. Volkov M.K. — Ann.Phys., (N.Y.), 1984, 157, p.285.
5. Heisenberg W. et al. — Z.Naturforsch., 1959, 14, p.441.
6. Umedzawa H., Matsumoto H., Taticki M. — «Thermo-Field Dynamics and Condensed States», Moscow: Mir, 1985.

Received on October 2, 1991.

УДК 530.1:51-72

ON EMBEDDING OF INTEGRABLE EQUATIONS IN (1 + 1) AND (2 + 1) DIMENSIONS INTO THE GENERALIZED SELF-DUAL YANG — MILLS EQUATIONS

A.D.Popov

The generalization of the self-dual Yang — Mills (SDYM) equations on the spaces of arbitrary even dimension is considered. It is shown that all integrable equations in (1 + 1) dimensions and many integrable equations in (2 + 1) dimensions may be obtained by the reduction of the generalized SDYM equations.

The investigation has been performed at the Laboratory of Theoretical Physics, JINR.

О вложении интегрируемых уравнений в (1 + 1) и (2 + 1) измерениях в обобщенные уравнения автодуальности модели Янга — Миллса

А.Д.Попов

Рассмотрено обобщение уравнений автодуальности модели Янга — Миллса на пространства произвольной четной размерности. Показано, что все интегрируемые уравнения в (1 + 1) измерениях и многие интегрируемые уравнения в (2 + 1) измерениях могут быть получены редукцией обобщенных уравнений автодуальности модели Янга — Миллса.

Работа выполнена в Лаборатории теоретической физики ОИЯИ.

1. It is known, that many integrable equations in (1+1) dimensions may be embedded into the SDYM equations in $d = 4$ dimensions (see, e.g., [1—7]). This is connected with the fact that SDYM equations may be written as a compatibility condition of two linear equations with the spectral parameter $\lambda \in C$ [8]. Imposing symmetries and algebraic constraints to the fields involved permits one to reduce SDYM equations to the Korteweg — de Vries (KdV) equations, generalized nonlinear Schrödinger (NLS) equations, Boussinesq and many others having a zero curvature representation

$$\partial_t U(\lambda) - \partial_x V(\lambda) + [U(\lambda), V(\lambda)] = 0.$$

Here matrices U and V are polynomials of λ of degree not higher than a second, or functions of $\frac{1}{\lambda \pm 1}$ (chiral models, for example). Clearly, the deri-

vative NLS equations, the Landau — Lifshitz equations and many others, having another type of dependence on spectral parameter, can't be embedded into the $d = 4$ SDYM equations. The hierarchies generated by the equations considered in [2,6] (KdV, NLS, AKNS, DNLS and other hierarchies) also are not embedded into them. That is why the SDYM equations in $d = 4$ can't play the role of the universal integrable system.

2. To solve these problems, it was suggested to consider the generalized SDYM equations for $d > 4$. Such equations were considered by Salamon [9], Ward [10], Galperin, Ivanov, Ogievetsky and Sokatchev [11] and by many others. The main progress was made by considering the self-duality equations in $d = 4n$, in which the hierarchies of KdV, NLS, DNLS, AKNS and of other equations may be embedded [2,6].

It is interesting to note that the geometric definition of self-duality in terms of linear systems and complex structure on R^{4n} (see [9—11]) are equivalent to the algebraic definition of self-duality (see, e.g., [12—15]). It was pointed by Strachan [6], how one may embed a number of hierarchies in $(2 + 1)$ dimensions into these equations. But in all these approaches one obtains only the rational dependence on the spectral parameter λ, and it is not clear how to include into consideration the models with the spectral parameter λ that belongs to the surfaces of genus $g \geq 1$. That is why such important equation as Landau — Lifshitz equation [16] is out of consideration.

We shall show a way to overcome this difficulty.

3. Method of solving of SDYM equations in $d = 4$ is connected with the ideas of the twistor theory [17]. The SDYM equations in $d = 4k$ are connected with the twistor theory for $4k$-dimensional hyper-Kähler manifolds [9—11,18]. Further generalization of the twistor theory (and of the self-duality equations) was considered in [19].

So for any Riemannian even-dimensional manifold M^{2n} we may consider a bundle $j(M^{2n})$ of the Riemannian almost complex structure with fibers $F = SO(2n)/U(n)$. The idea of the papers [19] is that we may choose as a twistor manifold a submanifold Z in $j(M^{2n})$ with fibres $B \subset SO(2n)/U(n)$. In these papers the case of $B = G/H$ and, in particular, of $B = CP^1 = Sp(1)/U(1)$ is considered as an example. But as B we may also choose the Riemannian surfaces of genus $g \geq 1$, and, in particular, the elliptic curves. They are embedded into the fibres $SO(2n)/U(n)$ with $n \geq 3$ over the $2n$-dimensional Riemannian manifold. We may use this fact.

Let us consider the flat case of R^{2n} and $j(R^{2n}) \cong R^{2n} \times F$. We have a bundle $j(R^{2n}) \to F$, where $F = SO(2n)/U(n)$. This is a canonical universal

complex bundle, geometry of which is well known (see, e.g., [20]). The fibre C^n_J over a point $J \in F$ is identified with the complex vector space (R^{2n}, J) of dimension n. Let us consider for simplicity one coordinate patch on F. Coordinates on it we may identify with the antisymmetric $n \times n$ matrices $J = (J^a_b)$, $a, b, \ldots = 1, \ldots n$. These matrices parametrise a complex structure on the fibres of the bundle $j(R^{2n}) \to F$ over the point J, and define the antiholomorphic vector fields $\partial/\partial\bar{z}^a(J)$ on R^{2n} and $\bar{\partial}_J$-operator:

$$\bar{\partial}_J = d\bar{z}^a(J)\frac{\partial}{\partial\bar{z}^a(J)}, \quad \frac{\partial}{\partial\bar{z}^a(J)} = \frac{\partial}{\partial\bar{z}^a} + J^b_a\frac{\partial}{\partial z^b}, \tag{1}$$

where $z^a = x^a + iy^a$, (x^a, y^a) are coordinates in R^{2n}, and z^a are coordinates on C^n_0. Clearly, $\bar{\partial}^2_J = 0$.

Consider the trivial Hermitian vector bundle E over the Euclidean space R^{2n}, associated with the principal G-bundle over R^{2n}, with connection which components are identified with the Yang — Mills (YM) potentials $A_1, \ldots, A_{2n}$. We shall denote by ψ the sections of the bundle $\tilde{E}$, which is the pull-back of the bundle E over R^{2n} to the manifold $j(R^{2n})$. They are functions $\psi(x, J)$ on $j(R^{2n})$ depending on $x \in R^{2n}$, $J \in F$ and taking values in the space of complex representation (e.g., C^N) of the algebra $\mathfrak{G}$.

Connection on a complex bundle E can be used to lift the operators $\bar{\partial}_J$ from R^{2n} to $j(R^{2n})$. We can introduce the structure of the holomorphic vector bundle in $\tilde{E}$ identifying the operator $\bar{\partial}$ on $\tilde{E}$ $(\bar{\partial}^2 = 0)$ with the $(0,1)$-component $\bar{D}$ of the connection on $j(R^{2n})$. In coordinate, a section ψ of the bundle $\tilde{E}$ is holomorphic if

$$(\bar{\partial}_a + J^b_a\partial_b + \bar{B}_a + J^b_a B_b)\,\psi(x, J) = 0, \tag{2}$$

$$\frac{\partial}{\partial\bar{J}^b_a}\psi(x, J) = 0, \tag{3}$$

where $B_1 = 2^{-1/2}(A_1 - iA_2)$, ..., $B_n = 2^{-1/2}(A_{2n-1} - iA_{2n})$, $\bar{J}^b_a$ is a complex conjugation for J^b_a. Condition (3) is equivalent to the choice of complex coordinates on the manifold F and Eqs. (3) may be trivially satisfied for ψ depending on J^b_a and not depending on $\bar{J}^b_a$. The linear equations (2),

defining the holomorphic structure in the bundle $\tilde{E}$, put some restrictions on the gauge fields B_a.

The compatibility condition of Eqs.(2) has a form:

$$F_{\bar{a}\bar{b}} + J_a^c F_{c\bar{b}} - J_b^c F_{c\bar{a}} + J_a^c J_b^d F_{cd} = 0, \tag{4}$$

where

$$F_{ab} = \partial_a B_b - \partial_b B_a + [B_a, B_b], \; F_{c\bar{b}} = \partial_c B_{\bar{b}} - \partial_{\bar{b}} B_c + [B_c, B_{\bar{b}}],$$

$$F_{\bar{a}\bar{b}} = (\overline{F_{ab}}), \; F_{\bar{c}b} = (\overline{F_{c\bar{b}}}).$$

By definition, Eqs.(4) are the generalized self-duality equations for the gauge fields in R^{2n}.

Now everything reduces to the choice of independent components J_a^b. By different choices of J_a^b we shall obtain different linear systems, different self-duality equations and the embeddings of different integrable equations into the generalized self-duality equations (4).

Let us choose, for example, $n = 2k$ and $d = 2n = 4k$. Replace $a, b, \ldots$ by $(\mu i), (\nu j), \ldots$, where $\mu, \nu, \ldots = 1, 2$; $i, j, \ldots = 1, \ldots k$. Put

$$J_{(\mu i)}^{(\nu j)} = \lambda \varepsilon_\mu^\nu \delta_i^j, \tag{5}$$

where $\varepsilon_1^2 = -\varepsilon_2^1 = 1, \lambda \in CP^1$. Then Eqs.(2) are reduced to the equations

$$(\bar{\partial}_{x_i} + \lambda \partial_{y_i} + \overline{C}_i + \lambda D_i)\psi = 0, \; (\bar{\partial}_{y_i} - \lambda \partial_{x_i} + \overline{D}_i - \lambda C_i)\psi = 0, \tag{6}$$

where $\partial_{x_i} \equiv \partial_{1i}$, $\partial_{y_i} \equiv \partial_{2i}$, $C_i \equiv B_{1i}$, $D_i \equiv B_{2i}$, $i = 1, \ldots, k$. Let

$$\partial_{y_i}\psi = -\bar{\partial}_{x_{i+1}}\psi, \; \partial_{x_i}\psi = \bar{\partial}_{y_{i+1}}\psi, \tag{7}$$

and $\partial_{y_i}\psi = D_i = C_i = 0$ when $1 \leq l < i \leq k$. Then linear system (6) is reduced to the systems, considered in [2,6].

Now let

$$J_{(\mu i)}^{(\nu j)} = \delta_\mu^\nu J_i^j. \tag{8}$$

where $J_1^2 = -J_2^1 = \pi^2$, $J_1^3 = -J_3^1 = \pi^3$, ..., $J_1^k = -J_k^1 = \pi^k$, and other J_i^j equal zero. Then we have

$$
\begin{aligned}
&(\bar{\partial}_{\mu 1} + \pi^{A}\partial_{\mu A} + \bar{B}_{\mu 1} + \pi^{A}B_{\mu A})\psi = 0,\\
&(\bar{\partial}_{\mu 2} - \pi^{2}\partial_{\mu 1} + \bar{B}_{\mu 2} - \pi^{2}B_{\mu 1})\psi = 0,\\
&\qquad\cdots\\
&(\bar{\partial}_{\mu k} - \pi^{k}\partial_{\mu 1} + \bar{B}_{\mu k} - \pi^{k}B_{\mu 1})\psi = 0,
\end{aligned}
\tag{9}
$$

where $A = 2, \ldots, k$. Let $\partial_{\mu 1}\psi = \bar{\partial}_{\mu 2}\psi = \ldots = \bar{\partial}_{\mu k}\psi = 0$, $B_{\mu 1} = \bar{B}_{\mu 2} = \ldots = \bar{B}_{\mu k} = 0$. Then Eqs.(9) are reduced to the equations, introduced by Ward [10]:

$$
\begin{aligned}
&(\partial_{t} + \pi^{A}\partial_{1A} + \bar{B}_{11} + \pi^{A}B_{1A})\psi = 0\\
&(\partial_{x} + \pi^{A}\partial_{2A} + \bar{B}_{21} + \pi^{A}B_{2A})\psi = 0
\end{aligned}
\tag{10}
$$

where $\partial_{t} \equiv \bar{\partial}_{11}$, $\partial_{x} \equiv \bar{\partial}_{21}$.

Finally, in (10) let $\pi^{A} = f^{A}(\lambda)$, where f^{A} are functions of $\lambda \in C$. It means that we consider one-dimensional complex submanifold B in the base F of the bundle $j(R^{2n}) \to F$ and the restriction $Z = j(R^{2n})|_{B}$ of this bundle on B. Then Eqs. (10) will define the holomorphic structure in the bundle $\bar{E}$ over the twistor manifold Z.

We may embed the equations of any integrable model in (1 + 1) dimensions in Eqs.(10) if we put $\partial_{\mu A}\psi = 0$, choose the functions $f^{A}(\lambda)$, matrices $B_{\mu A}$, $\bar{B}_{\mu A}$ and a number k ($d = 4k$). For example, the Landau — Lifshitz equations may be obtained as a particular case of Eqs.(10) when $k = 7$.

If we take $\partial_{y} \equiv \partial_{1k}$, $\partial_{2A}\psi = 0$, $\partial_{1i}\psi = 0$ when $i \neq k$, $\partial_{y}\psi \neq 0$ and choose $\pi^{A} = \lambda^{A-1}$, then Eqs.(10) coincide with the equations of the integrable models in (2 + 1) dimensions, introduced in [6]. It is not clear now whether all the integrable equations in (2 + 1) dimensions may be embedded into Eqs.(10) or not. Apparently, this may be done if one will use the infinite dimensional Lie algebras (see, e.g., [5,21]). In any case, all integrable equations in (2 + 1) dimensions and many integrable equations in (2 + 1) dimensions can be obtained upon appropriate reduction of the generalized SDYM equations (4).

References

1. Ward R.S. — Phil. Trans. R. Soc. Lond., 1985, A315, p.451; Lect. Notes Phys., 1987, 280, p.106; Lond. Math. Soc. Lect. Notes Ser., 1990, 156, p.246.

2. Mason L.J., Sparling G.A.J. — Phys. Lett., 1989, A137, p.29.
3. Chakravarty S., Ablowitz M.J., Clarkson P.A. — Phys. Rev. Lett., 1990, 65, p.1085; 2086 E; Ablowitz M.J., Chakravarty S., Takhtajan L.A. — PAM Report, 1991, 108; 1991, 113.
4. Bakas I., Depireux D. — Mod. Phys. Lett., 1991, A6, p.1561.
5. Chakravarty S., Ablowitz M.J. — In: Painleve Transcendents, Ed. by D.Levi and P.Winternitz, Plenum Press, N.Y., 1992, p.331.
6. Strachan I.A.B. — Twistor Newsletters, 1992, 34; Oxford preprint, 1992.
7. Ivanova T.A., Popov A.D. — Phys. Lett. A, in press.
8. Belavin A.A., Zakharov V.E. — Phys. Lett., 1978, B73, p.53.
9. Salamon S. — Invent. Math., 1982, 67, p.143.
10. Ward R.S. — Nucl. Phys., 1984, B236, p.381.
11. Galperin A. et al. — Ann. Phys., 1988, 185, 1 and 22.
12. Corrigan E. et al. — Nucl. Phys., 1983, 214, p.452.
13. Corrigan E., Goddard P., Kent A. — Commun. Math. Phys., 1985, 100, p.1.
14. Galicki K., Poon Y.S. — J. Math. Phys., 1991, 32, p.1263.
15. Popov A.D. — Mod. Phys. Lett., 1992, A7, p.2077.
16. Faddeev L.D., Takhtajan L.A. — Hamiltonian Methods in the Theory of Solitons, Springer, Berlin, 1987; Dubrovin B.A., Krichever I.M., Novikov S.P. — Integrable Systems: Modern Problems in Mathematics. Fundamental Directions, V.4, VINITI, Moscow, 1985.
17. Atiyah M.F. — Classical Geometry of Yang — Mills Fields. Fermi Lectures, Scuola Normale Superiore Pisa, 1979.
18. Hitchin N.J., Karlhede A., Lindstrom U., Rocek A. — Commun. Math. Phys., 1987, 108, p.535.
19. O'Brien N.A., Rawnsley J.H. — Ann. Global Anal. Geom., 1985, v.3., N 1, p.29; Rawnsley J.H. — Lect. Notes Math., 1987, v.1263, p.97; Burstall F.E. — Lond. Math. Soc. Lect. Notes Series., 1990, v.156, p.53; Baston R.J., Eastwood M.G. — The Penrose Transform. Its Interaction with Representation Theory, Clarendon Press, Oxford, 1989.
20. Milnor J.W., Stasheff J.D. — Characteristic Classes, Princeton Univ. Press, Princeton, 1974.
21. Chakravarty S., Kent S., Newman E.T. — J. Math. Phys., 1992, 33, p.382.

Received on October 2, 1992.

УДК 539.171

ELASTIC SCATTERING OF A SECONDARY ^{11}Li BEAM ON ^{28}Si AT 29 MeV/n

F.A.Gareev, S.N.Ershov, G.S.Kazacha, S.M.Lukyanov,
Yu.E.Penionzhkevich, N.K.Skobelev, S.P.Tretyakova
JINR, P.O.Box 79, Dubna, Russia

M.Lewitowicz, C.Borcea, F.Carstoiu, M.G.Saint-Laurent,
A.Kordyasz, R.Anne, P.Roussel-Chomaz
GANIL, BP 5027, F-14021 Caen, France

R.Bimbot, V.Borrel, S.Dogny, D.Guillemaud-Mueller,
A.C.Mueller, F.Pougheon
IPN, F-91406 Orsay, France

Z.Dlouhy, L.Nosek, J.Svanda
Nucl.Phys.Inst., CS-25068 Rez, Chechoslovakia

The elastic scattering of a secondary ^{11}Li beam (29 MeV/n) on a ^{28}Si target has been measured for the first time. To compensate for the low intensity of the secondary beam, an efficient detecting system permitting to obtain reliable experimental data has been used. An attempt has been made to reproduce the data in a phenomenological analysis and with coupled-channel calculations with a double folding optical potentials, with energy and density dependent effective interaction and realistic densities. An unusually large value of the surface diffuseness parameter for the real part is required in the phenomenological optical potential for description of the experimental data. In coupled-channel calculations with the folding optical potential a better description is achieved if a neutron halo of ^{11}Li is taken into account.

The investigation has been performed at the Laboratory of Nuclear Reactions, JINR and GANIL.

Упругое рассеяние вторичного пучка ^{11}Li при 29 МэВ/нуклон на кремнии-28

Ф.А.Гареев и др.

Впервые измерено упругое рассеяние вторичного пучка ^{11}Li (29 МэВ/нуклон) на мишени из ^{28}Si. Для компенсации низкой эффективности вторичного пучка использовалась эффективная детектирующая система, позволявшая получить достоверные экспериментальные данные. Сделана попытка воспроизвести данные с феноменологическим оптическим потенциалом и с использованием потенциала двойной свертки с учетом связанных каналов с энергетической и плотностной зависимостями

эффективного взаимодействия и реалистическими плотностями. Для описания экспериментальных данных феноменологически требуется вводить необычно большое значение параметра поверхностной диффузности реальной части потенциала. В расчетах с использованием связанных каналов с потенциалом двойной свертки лучшее согласие достигается, если брать в учет нейтронное гало в ^{11}Li.

Работа выполнена в Лаборатории ядерных реакций ОИЯИ и ГАНИЛ.

1. Introduction

In recent experiments at GANIL [1], the existing ^{11}Li interaction cross section data [2,21,23] have been complemented by a measurement of the Coulomb dissociation cross section and the neutron angular distribution at an energy of 30 MeV/n. These new data together with measurements of transverse and parallel momentum of ^{9}Li produced in ^{11}Li induced reactions [3,4] have provided further support for the neutron halo hypothesis. Nevertheless, although they give information about the extent of the neutron cloud and the degree of correlation between the two extra-core neutrons, these experiments are unable to provide detailed information about the proton and neutron distributions in ^{11}Li. Such information can, in principle, be obtained from measurements of the elastic-scattering angular distributions. In this way, it should be possible to test various theoretical descriptions of ^{11}Li. The aim of the present experiment was to advance the idea of a «non-destructive» study of ^{11}Li, by measuring its elastic scattering from a ^{28}Si target and to compare it to the elastic scattering of the stable nucleus ^{7}Li.

In the similar measurements performed recently at RIKEN for the ^{9}Li and ^{11}Li nuclei on protons [29] the elastic cross section for the ^{11}Li was found about factor of two smaller than for the ^{9}Li case. However, results of another experiment performed recently at NSCL MSU for the system ^{11}Li + ^{12}C [30] have shown a strong enhancement of the ratio of σ/σ_R for ^{11}Li as compared with the system ^{11}C + ^{12}C. The later observation indicates an enhanced far-side dominance in the angular distribution of the ^{11}Li scattering predicted by Satchler et al. [24]. In the analysis of both the experiments considerable changes in optical potential parameters were necessary to reproduce the ^{11}Li data. In the present work the use of a heavier target should, in principle, enhance the influence of inelastic processes such as break-up and Coulomb excitation of the projectile on the elastic channel.

2. Experimental Method

Secondary beams of 29 MeV/n ^{11}Li (150 pps) and 25.4 MeV/n ^{7}Li (1000 pps) were produced at GANIL in the reaction of a 76 MeV/n ^{18}O pri-

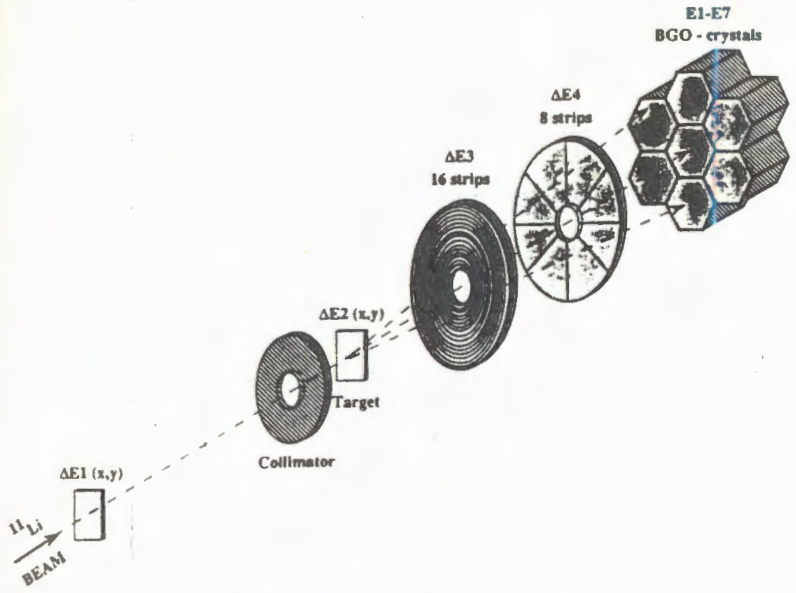

Fig.1. Experimental set-up; see text for details

mary beam bombarding a 360 mg/cm^2 Be + 2900 mg/cm^2 C production target. The outgoing fragments were separated by means of the LISE3 spectrometer [5] and identified by their energy loss and time of flight. The purity of each of the secondary beams was better than 98%. The energy width of the secondary beam was defined by the momentum acceptance of the LISE spectrometer which was set to 2.3% in the case of ^{7}Li and to 9.4% in the case of ^{11}Li. The angular dispersion of the secondary beams was smaller than 0.5°.

A schematic view of the set-up used in the present experiment is shown in figure 1.

To compensate for the low intensity of the secondary beams we choose a detection system with a very high efficiency of registration of scattered particles. At the same time a big angular and energy spread of the secondary beams implied measurements of angle and position on a target for each incoming particle.

The trajectory of each particle was reconstructed by means of two position-sinsitive X-Y silicon detectors ($\Delta E1$, $\Delta E2$), with thickness of 71 mg/cm^2 and 104 mg/cm^2, respectively, placed at the final focal point of the spectrometer. The $\Delta E2$ detector was simultaneously used as an active secondary target. The position resolution of each of detectors was 1 mm.

The incident angle of the particles on the secondary target was measured with the accuracy better than 0.5°. The collimator, 13 mm of diameter placed in front of the target, was used to limit the size of the beam spot. Two circular silicon detectors, one with 16 concentric strips ($\Delta E3$) and other with 8 radial sectors ($\Delta E4$) were used to determine the position and energy loss of scattered particles. The detectors had a 69 mm of outside diameter and a central hole 22 mm of diameter. The distance between the secondary target and the circular detectors was adjusted to cover center-of-mass diffusion angles between 5° and 17° for ^{7}Li and between 5° and 22° for ^{11}Li. A matrix of seven BGO crystals [6] ($E1$-$E7$), used to determine the residual energy of each particle complemented the experimental set-up.

The overall relative energy spread of diffused particles including the energy width of the secondary beam, the intrinsic resolution of the detectors and the energy straggling was about 7% for ^{7}Li and 20% for ^{11}Li ions.

The geometrical efficiency of the system was calculated on the event by event basis taking into account the trajectory of the incident particle and the geometry of the strip detectors. The systematic uncertainties in the measured differential cross section introduced by this procedure are smaller than 10%.

3. Results

Angular distributions of elastic scattering of ^{7}Li and ^{11}Li measured in this experiment are shown in figures 2—7. The error bars indicated for the experimental data correspond to the statistical errors.

The use of the thick target, the angular resolution of $\Delta\theta \approx 1.5°$ and the lack of separation between elastic and inelastic scattering resulted in a flattening of the diffractional structure of the spectra.

The measured distributions for ^{7}Li are in the qualitative agreement with measurements at lower projectile energies [26]. It has a shape typical for scattering of stable nuclei in the Frauenhofer diffraction region — the ratio $\sigma/\sigma_{\text{Ruth.}}$ oscillates and decreases with increasing scattering angle. For the case of ^{11}Li the behaviour of experimental data is rather unusual, the ratio $\sigma/\sigma_{\text{Ruth.}}$ is almost constant in the measured range of angles. The $\sigma/\sigma_{\text{Ruth.}}$ lies for ^{11}Li higher than the one observed in an analogous distribution for the elastic scattering of ^{6}Li [27] and ^{9}Be [28] on ^{28}Si at approximately the same energy of relative motion.

4. Optical Model Analysis

4.1. Phenomenological Optical Potential

The analysis of the elastic scattering was carried out in the framework of the conventional optical model by using the standard Wood—Saxon form:

$$U(r) = V_{\text{Coul}}(r) - Vf_V(r) - iWf_W(r),$$

where $f_V(r)=(1+\exp[(r-R_V)/a_V])^{-1}$, $f_W(r)=(1+\exp[(r-R_W)/a_W])^{-1}$, $R_V = r_V A_T^{1/3}$, $R_W = r_W A_T^{1/3}$ and $V_{\text{Coul}}(r)$ is the Coulomb potential of the uniformly charged sphere. The potential parameters V, W, r_V, r_W, a_V and a_W were fitted to the experimental data using the standard χ^2 method.

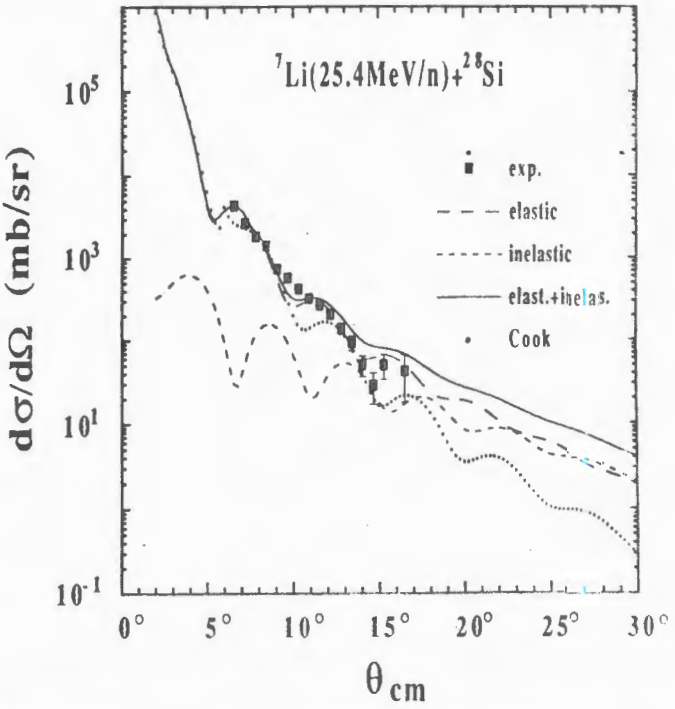

Fig.2. Comparison of the experimental data with theoretical calculations for elastic scattering of ^{7}Li+^{28}Si at energy $E_{^7\text{Li}}$ = 177.8 MeV; long-dashed line — elastic scattering with optical potential «A» from table 1; short-dashed — inelastic cross section; solid — sum of elastic and inelastic cross sections; dotted — elastic cross section with potential from [26]

The theoretical cross sections have been averaged over the angular resolution before comparison to the experimental cross sections.

As the inelastic events have not been resolved by our detection system, we have estimated the inelastic cross section for the excitation of the 2^+, 1.78 MeV state in ^{28}Si and added it incoherently to the elastic one. The estimation of the inelastic cross section was made in the framework of the DWBA. The inelastic form factor was chosen as a derivative of the optical potential:

$$F(r) = \beta_2 R_V \frac{dV(r)}{dr} + i\beta_2 R_W \frac{dW(r)}{dr}$$

with $\beta_2 R_V = \beta_2 R_W = 1.21$ fm [27].

In figure 2 the results of the calculations are compared to the experimental data on the elastic scattering of ^{7}Li. In the calculations the geometric parameters of the optical potential were taken from the global parametrization [26], and the potential depths V and W were adjusted to reproduce the data (see table 1). Theoretical calculations of the elastic scattering are shown by the long dashed line; inelastic one, by the short dashed line; and their sum, by the solid line. For comparison the elastic cross section calculated with parameters from [26] is also shown by the dotted line. From the calculations it follows that the contribution from inelastic processes may be important at the end of the measured angular range and theoretical calculations can describe the experimental data with «standard» optical potentials.

Table 1. Parameters of the optical potentials for the system ^{7}Li + ^{28}Si

	$-V$ MeV	r_V fm	a_V fm	$-W$ MeV	r_W fm	a_W fm	$\langle r_V^2\rangle^{1/2}$ fm	$\langle r_W^2\rangle^{1/2}$ fm	σ_R b	χ^2/N
A	226.8	1.286	0.853	37.26	1.739	0.809	4.38	5.08	1820.	7.0
from [26]	114.2	1.286	0.853	29.75	1.739	0.809	4.38	5.08	1700.	10.4

Table 2. Parameters of the optical potentials for the system ^{11}Li + ^{28}Si

$-V$ MeV	r_V fm	a_V fm	$-W$ MeV	r_W fm	a_W fm	$\langle r_V^2\rangle^{1/2}$ fm	$\langle r_W^2\rangle^{1/2}$ fm	σ_R b	χ^2/N
204.48	0.585	1.737	8.23	2.18	0.425	6.604	5.36	1445.2	1.84

In the case of ^{11}Li the situation is different. The calculations based on the usual nuclear potentials cannot give a reasonable description of the experimental data. As an example, on figure 3 the elastic cross section of ^{11}Li (dotted line) calculated with the optical potential from global paramet-

rization [26] is shown. It is very difficult to give more definite limits for changing the optical potential paramteters based only on the experimental data within a relatively narrow angular range. Therefore, only one example of possible potentials is given in table 2 and the calculated elastic cross section is shown by the long-dashed line in figure 3. The contribution from inelastic scattering, calculated analogously to the ^{7}Li case, is shown by the short-dashed line; and total cross section, by the solid line. The root mean square (rms) radius of the real potential is in our case about 6 fm, and in the strong absorption region the potential has a refractive character. The relatively large value of surface diffuseness of the real part obtained for this potential can reflect the extended density distribution of ^{11}Li. Further important information about the scattering nature may be obtained from a near-side and a far-side decomposition of the elastic cross section [31]. The

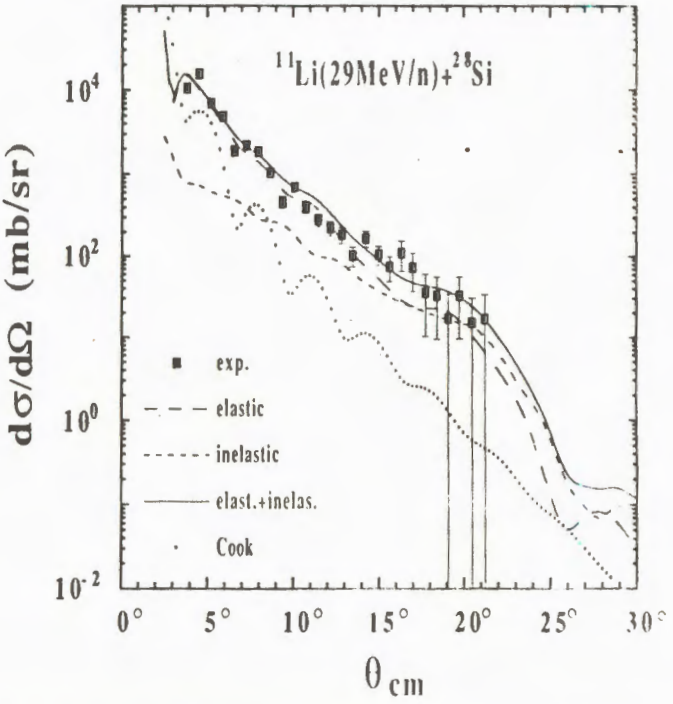

Fig.3. Comparison of the experimental data with theoretical calculations for elastic scattering of ^{11}Li+^{28}Si at energy $E_{^{11}Li}$ = 319 MeV. Long-dashed line — elastic scattering with optical potential from table 2; short-dashed — inelastic cross section; solid — sum of elastic and inelastic cross sections; dotted — elastic cross section with potential from [26]

decomposition for ^{11}Li elastic scattering is shown in Fig.4 where the long-dashed and short-dashed lines give the near-side and far-side contributions, respectively. The crossover point of the near-side and far-side components is close to $\theta \sim 2°$ and the region of diffraction oscillations occupies the angle range up to ~ 8°. At larger angles the far-side component dominates in the elastic cross section. In the case of ^{7}Li scattering the crossover point is near 8° and the region of difraction oscillation spreads up to nearly 20°. Thereby, the smoothness of σ/σ_R in the ^{11}Li case at angles larger than $\theta \geq 10°$ may be connected with a more strong manifestation of nuclear refractive properties in halo nuclei. The elastic cross section for the potential given in table 2 shows the picture of the rainbow scattering [32]. Of course, it does not mean that the rainbow scattering is revealed in ^{11}Li scattering. The appearance of this effect will depend on transparency of nuclear potentials. To give more definite answers, it is necessary to have the experimental data for ^{11}Li scattering in a wider angle interval covered by the exponential fall-off of the elastic cross sections and diffraction oscillations at small angles.

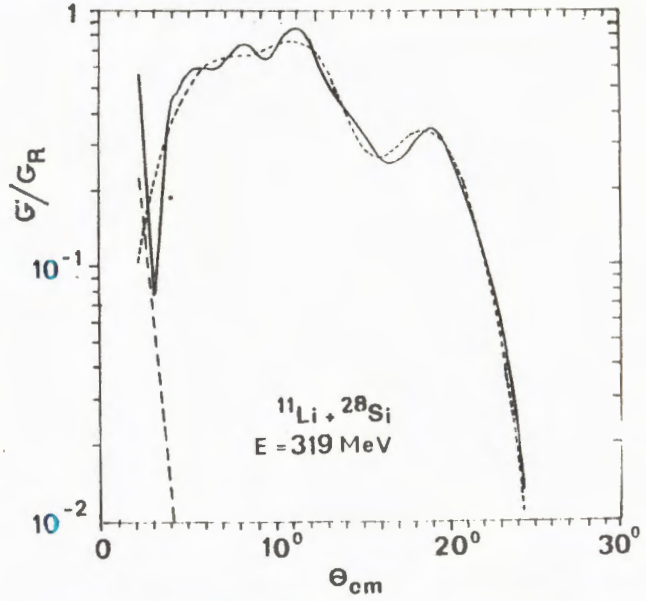

Fig.4. The near-side and far-side decomposition of the elastic scattering ^{11}Li+^{28}Si at energy $E_{^{11}Li}$ = 319 MeV.Solid line, long-dashed and short-dashed are elastic cross section, near-side and far-side contributions, respectively

The contribution of soft modes in ^{11}Li [33] to the elastic cross section is also possible and requires further investigations.

4.2. Double Folding Potential

Simplified coupled channel (CC) calculations were done using the code ECIS [7]. The ^{28}Si was treated as a rigid rotor and couplings involving both excitation and de-excitation between ground state (0^+) and first excited state (2^+) were used. The $B(E2\uparrow)$ value was taken from the compilation [8] and a deformation length of $\delta = 1.15$ fm was used, which gave satisfactory results in a similar CC calculation for ^{6}Li + ^{28}Si at 210 MeV [9].

The bare CC optical potential (the real part) was calculated in the semi-microscopic double folding model [10] using the density and energy dependent effective interaction (DDM3Y) from [11,12]. The geometry of the imaginary part of the optical potential was taken to be the same as for the real part:

$$V_{\text{opt}}(r) = (N_v + iN_w)V_{\text{DDM3Y}}(r).$$

No attempt has been done to fit the normalization constants N_v, N_w but rather they have been fixed by some physical requirements or by analogy with similar systems. The antisymmetrization effects and the density dependence of the effective interaction in the calculation of the folding potential were treated similarly as in reference [12]. The necessary nuclear densities were constructed by standard Hartree-Fock (H.F.) calculation using Skyrme II (SkII) parametrization of the effective interaction [13]. Spherical symmetry and occupation numbers determined by single particle energies were assumed. The nuclear matter rms radii of the resulted densities (r_m) and the rms radii of the corresponding DDM3Y potentials (r_v) are given in table 3. Also the corresponding values for the «halo» density of Bertsch et al. [14] are indicated. The rms radii of the halo density of Bertsch et al. agree with the effective rms matter radius of 3.12 ± 0.16 fm extracted by Tanihata et al. [15] from the measured interaction cross section at high energy. Therefore it is interesting to check this density in the elastic scattering of ^{11}Li at lower energy.

As a test ground for our calculations, the ^{6}Li elastic scattering on ^{28}Si at 154 MeV [16] was taken. Studies [17—19] on elastic scattering of light Li isotopes in a wide range of energy and targets resulted in a strong renormalization (up to 50%) of the effective M3Y interaction in order to explain the data. It was suggested by Sakuragi [19] that this reduction could be explained by projectile break-up effects. The dynamical polarization potential (DPP) induced by projectile break-up process has a repulsive surface contribution to the real optical potential with a strength of about 40% of the

Table 3. The matter density rms radii for Li isotopes and ^{28}Si calculated with the Hartree-Fock method and the Skyrme II potential $\langle r_m^2 \rangle^{1/2}$ and the rms radii of the corresponding DDM3Y folding potentials $\langle r_V^2 \rangle^{1/2}$

	^{6}Li	^{7}Li	^{11}Li	^{28}Si
$\langle r_m^2 \rangle^{1/2}$ [fm]	2.24[a]	2.31[a]	2.68[a] 2.99[b]	3.1a)
$\langle r_V^2 \rangle^{1/2}$ [fm]	4.034[a]	4.083[a]	4.321[a] 4.579[b]	

a) calculated with the standard Hartree-Fock method and the Skyrme II potential [13].
b) calculated with the halo density of Bertsch et al. [14].

Table 4. Effective square radius r_0^2 and total reaction cross sections σ_R for Li isotpes on ^{28}Si

	^{6}Li	^{7}Li	^{8}Li	^{9}Li	^{11}Li
E [MeV/n]	25.7	25.4	25.4	29	29
r_0^2 [fm^2]	1.290[a]	1.285[a]	1.290[a]	1.246[a]	1.305[a]
σ_R [mb]	1577[b]	1672[b]	1768[b]	1771[b]	2001[b]
σ_R [mb]	1521[c]	1583[c]			2064[c] 1402[d]
σ_R [mb]					2947±386[e]

[a] from Saint-Laurent et al. [21],
[b] values calculated for the reactions ^{n}Li+^{28}Si with the formula of Kox et al. [25] and parameters from [21],
[c] calculated with DDM3Y and $N_V = N_W = 1.0$,
[d] calculated with DDM3Y and $N_V = 0.60$, $N_W = 0.18$,
[e] experimental value of Villari et al. [23] at 25.5 MeV/n.

folding potential and a negligible imaginary part, with the effect of decreasing the far-side tail component of the scattering amplitude at large angles. Similar reduction has been found recently in a secondary ^{7}Be beam scattering on ^{12}C at 140 MeV by Yamagata [20]. However, there is no need for such a reduction in the calculations that we performed using DDM3Y effective interaction. The results obtained for ^{6}Li with the normalization $N_V = 1.0$, $N_W = 0.9$ (figure 5) show a reasonable agreement with the data.

In a next step, the same procedure was applied for ^{7}Li data measured in the present experiment. As can be seen in figure 5 the incoherent addtion of elastic and inelastic scattering results in a rather flat diffractional pattern.

The calculated reaction cross sections for ^{6,7}Li are in good agreement with the estimated values based on the semiempirical formula of Kox et al. [25] with the parameters from Saint-Laurent et al [21] (see table 4).

In the same spirit, calculations were performed for ^{11}Li elastic scattering data. In contrast to the ^{7}Li case, the experimental ^{11}Li cross section lies above and decreases slower than the corresponding CC prediction if the CC bare optical potential is calculated with the normalization $N_v = 1.0$, $N_W = 1.0$ (figure 6). The H.F.—SkII density for ^{28}Si and the density of Bertsch et al [14] (solid line) and H.F.—SkII (dashed line) for ^{11}Li were used. While the calculated elastic cross section is rather insensitive to the value of the deformation of the potential over the range of experimental data, the inelastic one depends strongly on this parameter. For example, the ratio $(\sigma_{el} + \sigma_{in})/\sigma_{el}$ doubles at large angles (> 15°) when the deformation length is chaged from 1.15 to 1.48 fm. However, in order to bring the calcu-

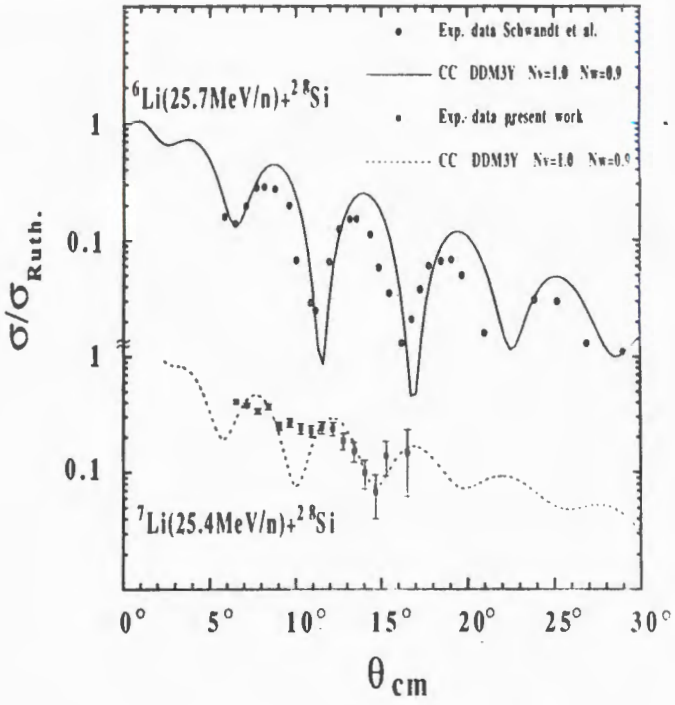

Fig.5. Angular distributions and CC calculation of elastic scattering of light Li isotopes; the bare CC potential is calculated with DDM3Y effective interaction and H.F.-SkII densities; normalization constants are indicated in the figure

lated elastic plus inelastic cross section to the measured one, unreasonably large deformation parameters are needed if the normalization is kept constant at $N_v = 1.0$, $N_W = 1.0$. The calculated reaction cross section for this normalization is about 2 barns for both densities.

Subsequently, one may examine the effect of different choices of ^{11}Li density, as stated above. For the same normalization, the halo density produces a potential with a larger radius (table 3) and the oscillations in the cross section are shifted to smaller angles. As can be seen from figure 6, especially for the large angles the presence of a neutron halo produces a quite different oscillation pattern.

The inability of the presented calculation to reproduce the experimental data leads us to modify the normalization constants. A choice of $N_v = 2.0$, $N_w = 1.0$ gives a reaction cross section of 2 barns, brings the calculated cross

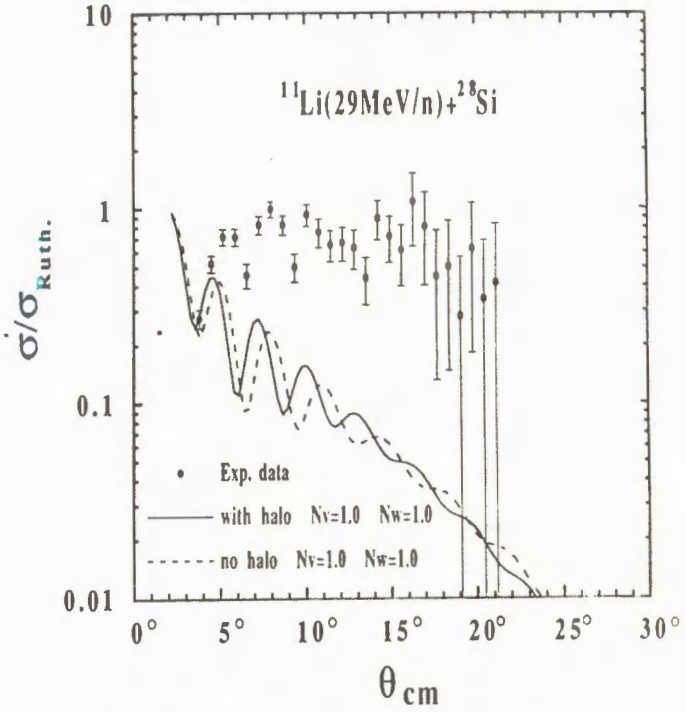

Fig.6. Angular distributions and CC calculation of ^{11}Li elastic scattering; the bare CC double folding potential is calculated with DDM3Y and H.F.–SkII density for ^{28}Si and the halo density of Bertsch et al. [14] for ^{11}Li (solid line) and H.F.–SkII density (dashed line); values of the normalization constants N_v and N_W are indicated in the figure

section over the data, but is unable to reproduce the most prominent oscillations. In order to reproduce the observed oscillations in the data, a reduction in the normalization constants seems to be necessary. The results obtained with $N_v = 0.6$, $N_w = 0.18$ (without neutron halo) and $N_w = 0.27$ (with halo) are shown in figure 7. Different N_w values were taken in order to obtain approximately the same value of the reaction cross section. If the N_w value was equal to 0.18, then the «no halo» calculations give an even smaller reaction cross section, though they come a little closer to the data. While the general trend is reproduced, the reaction cross section drops to a value of 1.4 barn which is quite puzzling in view of the existing data concerning the reaction cross section.

The interaction of ^{11}Li is dominated by the break-up process. In a recent experiment at GANIL [1], the two neutron removal cross section of ^{11}Li on Be (0.47 barn) and Ni (1.3 barn) targets was measured at the same energy as in the present experiment. From these numbers one could esti-

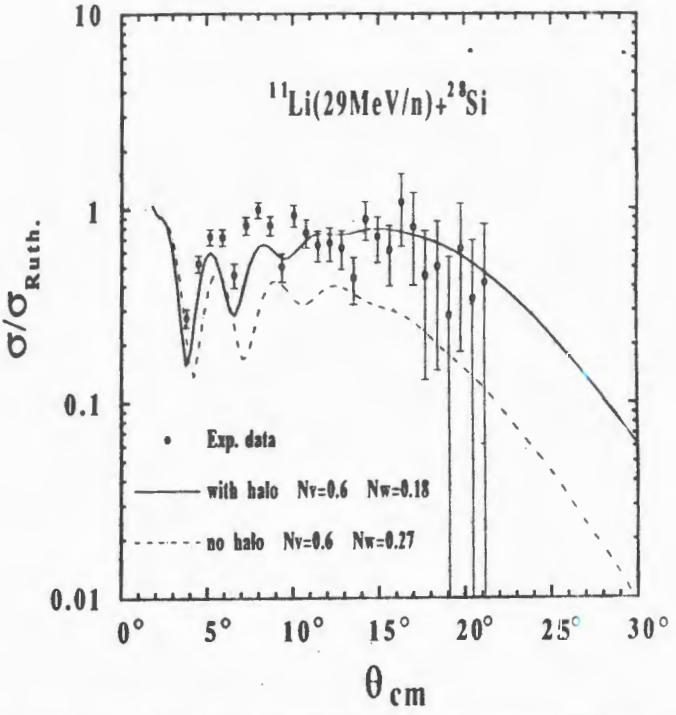

Fig.7. The same as fig.6 but for different normalization constants N_v and N_w; total reaction cross section $\sigma_R = 1.4$ barn in both calculations

mate the break-up cross section for ^{28}Si to be in the range of 0.9—1.0 barn. This is practically one half of the reaction cross section predicted by the formula of Kox et al. [25]. Fukuda et al. [22] have found recently that such empirical formula underpredicts the reaction cross section for halo nuclei by 20—30%. Therefore, a reasonable value of the reaction cross section for ^{11}Li + ^{28}Si at 29 MeV/n could be 2.3—2.5 barns, in relative agreement with the value measured by Villari et al. [23] at 25 MeV/n. The measurement of ^{9}Li transverse [3] and parallel [4] momentum distributions showed that due to the very diffuse structure of ^{11}Li, the break-up process is dominant at large impact parameters, in contrast with a «normal» nucleus like ^{7}Li. In the present experiment this is confirmed by the analysis of the energy spectrum of the diffused ^{11}Li ions. If the scattering of ^{11}Li at low impact parameters (i.e. at diffusion angle larger than about 4°) is accompanied by a break-up of this nucleus ^{11}Li → ^{9}Li + 2n, one should observe in the measured spectum of

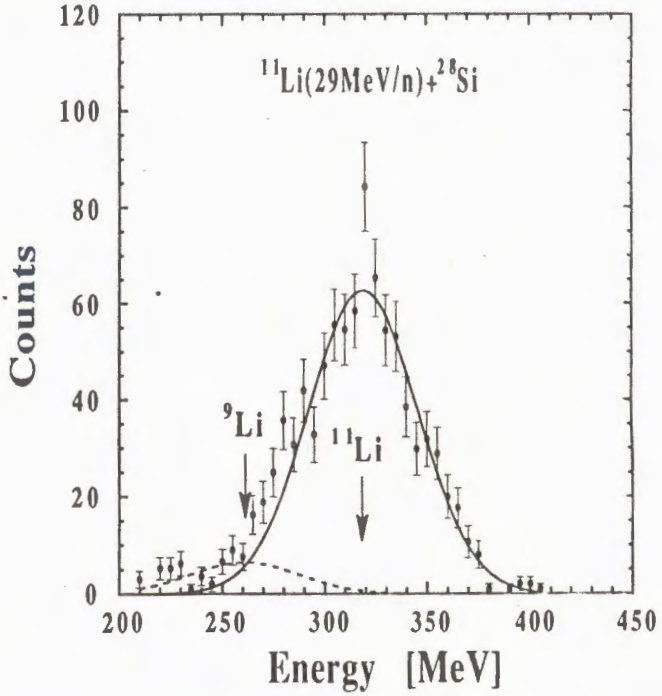

Fig.8. Experimental spectrum of the total energy of scattered ions for the 29 MeV/n ^{11}Li secondary beam; the curves represents a two-gaussian fit centered at the mean energies of ^{9}Li (dashed line) and ^{11}Li (solid line) indicated in the figure by arrows

total energy (sum of energy losses in all detectors), shown in figure 8, a peak corresponding to the 29 MeV/n ^{9}Li ions. A careful mathematical analysis set an upper limit of the contribution of ^{9}Li to 5%. Therefore, the ^{11}Li scattering is influenced by the break-up process only at very small angles, where the optical model amplitude is dominated by the Coulomb scattering. The cross section measured in the angular domain covered by the present experiment is completely insensitive to the break-up process. The loose structure of ^{11}Li is contained in our optical potential through the halo density, which produces only a small shift in the potential radius. A simple renormalization of the potential cannot account for the nonlocal dynamic polarization potential induced by the break-up process. Similar ideas were advanced by Satchler et al. [24]. They suggested that an appropriate normalization of the real folding DDM3Y potential might be equal to 0.57. With this normalization the calculated optical model reaction cross section (1.4 barn) represents approximately the difference between the estimated total reaction cross section and the estimated break-up cross section.

One should also notice that a very similar total reaction cross section (1.45 barn, see table 2) was obtained also in the phenomenological optical model analysis presented in section 4.1.

As can be seen in figure 7 significant differences appear by using different density distributions for ^{11}Li. At practically the same normalization of the effective interaction and at the same total reaction cross section, the halo density reproduces better the data than the no halo density.

5. Conclusions

We have measured for the first time the angular distribution of the elastic scattering of a neutron halo nucleus on the ^{28}Si target. For this purpose, a secondary ^{11}Li beam was used. Despite the rather low intensity, the high efficiency of the detecting system permitted to obtain reliable experimental information. The corresponding angular distribution can be reasonably described by using the phenomenological optical potential and the semimicroscopic double folding model with density and energy dependent effective interaction and realistic densities. However, in the analysis with the phenomenological optical potential the strong modification of the «standard» parameters seems to be necessary for the description of the experimental data. In the semimicroscopic model a strong renormalization of the real part of the optical potential seems to the necessary in order to reproduce the measured angular distributions. At the same time, the important constraint of reproducing the extremely large measured total reaction cross section could not be satisfied. A reason for this discrepancy could be the insensitivity of our data to the break-up process over the measured angular range.

For loosely bound ^{11}Li nucleus, with a very long tail of the neutron density distribution, this process takes place mainly at large impact parameters and the corresponding cross section represents an important fraction of the total reaction cross section. The strong nonlocal dynamical polarization potential induced by this process cannot be simulated by a simple renormalization of the DDM3Y effective interaction.

The results of present experiment confirm conclusions drawn by Kolata et al. [30] on the enhanced refraction and on the importance of a very long absorption in the elastic scattering of ^{11}Li on light targets.

The structure of ^{11}Li enters in the folding potential only through projectile density and the presence of the neutron halo produces relatively small changes in the potential. Nevertheless it seems that the calculations with the halo density reproduce better the experimental data.

Most of the difficulties encountered in the interpretation of the present data come from the lack of separation between elastic and inelastic events which would have required a much better energy resolution for the detected ^{11}Li.

The results of present experiment proved that a measurement of elastic scattering of very exotic nuclei although technically difficult can be performed even at a very low (several hundred particles per second) intensity of a secondary beam. For a complete explanation of the obtained angular and energy distrubiton of diffused ^{11}Li ions particular properties of the ^{11}Li nucleus due to a presence of a neutron halo have to be taken into account. In particular a contribution of soft modes of a giant resonance in ^{11}Li to the elastic cross section is possible and requires further investigations.

Similar experiments performed with higher angular and energy resolution are necessary to confirm and to study the phenomena of neutron halo for other light neutron-rich nuclei as ^{11}Be, ^{14}Be and ^{17}B.

Acknowledgements

We would like to thank Prof. Yu. Oganessian, Dr. N. Alamanos. Dr. R.J. Lombard, Dr. J. Raynal, Dr. K. Terenetsky and Dr. V. Verbitsky for stimulating and fruitful discussions. Furthermore we would like to acknowledge F. Georffroy, R. Hue and A. Latimier for their technical assistance during the experiment. The authors acknowledge the support of the French IN2P3.

References

1. Anne R. et al. — Phys. Lett., 1990, B250, p.19;
   Riisager K. et al. — Nucl. Phys., 1992, A540, p.365.
2. Tanihata I. et al. — Phys. Lett., 1985, 160B, p.380.
3. Kobayashi T. et al. — Proc. Second Int. Conf. on Raioactive Nucl. Beams, Louvain-la-Neuve, Belgium, 19-21 Aug. 1991, ed. Th. Delbar, p.197.

4. Orr N. et al. — To be published;
Morrissey D.J. et al. — Proc. Second Int. Conf. on Radioactive Nuclear Beams, Louvain-la-Neuve, Belgium, 19-21 Aug. 1991, ed. Th. Delbar, p.51.
5. Anne R., Mueller A.C. — Inter. Conf. EMIS-2, Sept. 2-6, 1991, Sendai, Japan, NIM in press and references contained therein.
6. Dlouhy Z. et al. — NIM, in press.
7. Raynal J. — ECIS88, unpublished.
8. Raman S. et al. — At. Data Nucl. Data Tables, 1987, 36, p.1.
9. Nadasen A. et al. — NSCL/MSU Annual Report 1988.
10. Satchler G.R., Love W.G. — Phys. Rep., 1979, 55, p.183.
11. Bertsch G. et al. — Nucl. Phys, 1977, A284, p.399.
12. Kobos A.M. et al. — Nucl. Phys, 1982, A384, p.65;
Kobos A.M. et al. — Nucl. Phys., 1984, A425, p.205;
Brandan M.E., Satchler G.R. — Nucl. Phys., 1988, A487, p.477.
13. Vautherin D., Brink D.M. — Phys. Rev., 1972, C5, p.626.
14. Bertsch G.F., Brown B.A., Sagawa H. — Phys. Rev., 1989, C39, p.1154.
15. Tanihata I. et al. — Phys. Lett., 1988, B206, p.592.
16. Schwandt P. et al. — Phys,. Rev., 1980, C21, p.1656.
17. Satchler G.R. — Phys. Rev., 1980, C22, p.919.
18. Tiede M.A., Trcka D.E., Kemper K.W. — Phys. Rev., 1991, C44, p.1698.
19. Sakuragi Y. — Phys. Rev., 1987, C35, p.2161.
20. Yamagata T. et al. — Phys. Rev., 1989, C39, p.873.
21. Saint-Laurent M-G. — Z. Phys., 1989, A332, p.457.
22. Fukuda M. et al. — Phys. Lett., 1991, B268, p.339.
23. Villari A.C.C. — Phys. Lett., 1991, B268, p.345.
24. Satchler G.R., McVoy K.W., Hussein M.S. — Nucl. Phys., 1991, A522, p.621.
25. Kox S. et al. — Phys. Rev., 1987, C35, p.1678.
26. Cook J. — Nucl. Phys., 1982, A388, p.153.
27. Nadasen A. et al. — Phys. Rev., 1989, C39, p.536.
Nadasen A. et al. — Phys. Rev., 1989, C40, p.1237.
28. Zisman M.S. et al. — Phys. Rev., 1980, C21, p.2398.
29. Moon C.B. et al. — Preprint RIKEN-AF-NP-126, to be published.
30. Kolata J.J. et al. to be published.
31. Fuller R.C. — Phys. Rev., 1975, C12, p.1561.
32. Dem'yanova A.S. et al. — Nucl. Phys., 1989, A501, p.336.
33. Fayans S.A. — Phys. Lett., 1991, B267, p.443.

Received on October 26, 1992.

УДК 539.1.074.8

POSITION-SENSITIVE NEUTRON DETECTOR AS A MODULE OF NEUTRON MULTIDETECTOR SYSTEM

I.D.Alkhazov*, A.V.Daniel*, V.D.Dmitriev*, E.M.Kozulin, A.V.Kuznetsov*, Yu.E.Penionzhkevich, V.A.Rubchenya*

The position-sensitive neutron scintillation detector has been made. The detector consists of two photomultipliers and quartz tube filled with liquid scintillator (∅ 6x100 cm) with n-γ separation properties. The properties of the detector have been measured and calculated by SITHA code. The position resolution is 10 cm and time resolution is 1.4 ns. The neutron efficiency varies between 31% and 26% for neutron energy between 2 and 7 MeV, for neutron energy threshold — 1 MeV, respectively.

The investigation has been performed at Radium Institute (St.Petersburg, Russia) and at the Laboratory of Nuclear Reactions, JINR.

Позиционно-чувствительный нейтронный детектор как модуль нейтронной многодетекторной системы

И.Д.Алхазов и др.

Создан позиционно-чувствительный нейтронный сцинтилляционный детектор. Детектор состоит из двух фотоумножителей и кварцевой трубы, заполненной жидким сцинтиллятором (диам. 6x100 см) с n-γ разделяющими свойствами. Характеристики детектора были измерены и рассчитаны по программе SITHA. Позиционное разрешение составило 10 см при временном разрешении 1,4 нс. Эффективность регистрации нейтронов меняется между 31% и 26% для энергии нейтронов от 2 до 7 МэВ, соответственно для энергетического порога регистрации нейтронов — 1 МэВ.

Работа выполнена в Радиевом институте (Санкт-Петербург, Россия) и в Лаборатории ядерных реакций ОИЯИ.

1. Introduction

In the past few years the interest for neutron multidetector systems in low and medium energy of heavy-ion physics greatly raised. The so-called «Neutron Balls» allow one to measure the neutron multiplicity and don't give information on the angular distribution and the energy spectra of the

*Radium Institute, St.Petersburg, Russia

detected neutrons. One needs multidetector system which gives simultaneously the energy spectra, the angular distribution, the mean multiplicity value (or multiplicity distribution of neutrons). The measurement of these characteristics can be performed by a number of small detectors, such as DEMON project [1]. The number of photomultipliers, however, leads to a sharp increase of the usage of electronics. Besides, a lot of calibration is necessary for their relative normalization. These problems can be reduced by means of large position-sensitive neutron detectors. A few types of such detectors had been studied in [2,3,4]. Each of these detectors is intended to solve a specific task: the detection of high-energy neutrons (up to 200 MeV) at a large solid angle [2], observation of neutron emission from fast moving fragments or from preequilibrium components for deep-inelastic heavy-ion reactions [3], scattering measurements of fast neutrons at small angles [4]. We designed the position-sensitive neutron detectors as the modules of neutron multidetector system [5]. The geometry of this multidetector system can be changed, for example, either near 4π solid angle neutron detector system or «neutron wall» system. The latter can consist of a few layers of position-sensitive neutron detectors for increasing the efficiency of high neutron energy measurements.

2. Construction and Principle of Operation of Position-Sensitive Neutron Detector (PSND)

The neutron detector consists of a quartz tube 100 cm long with 6 cm diameter (thickness of the walls: 2.5 mm) and two photomultipliers PM-30 with 50 mm dia. of photocathode. The tube is filled with liquid scintillator LS-13 [6] (analog of NE-213, with n-γ separation properties). The photomultipliers are coupled directly to the liquid scintillator in order to avoid light attenuation. Between PM and both ends of quartz tube there is a collapsible conjunction which consists of flanges and a special rubber. Tests have shown that this rubber is resistant to the liquid scintillator. The construction of the expansion chamber allows horizontal as well as vertical mounting of the detector. The detector is shielded against light with a titanium envelope. The scheme of the PSND is presented in fig.1.

Principle of time and position determination is shown in fig.2. The position information is obtained from the difference between the light travelling times (τ_L and τ_R) to two PMs at both ends of neutron detector. The position-independent time-of-flight is given by equation (see fig.2), with c — velocity of light, n_r — refractive index of liquid scintillator, t —

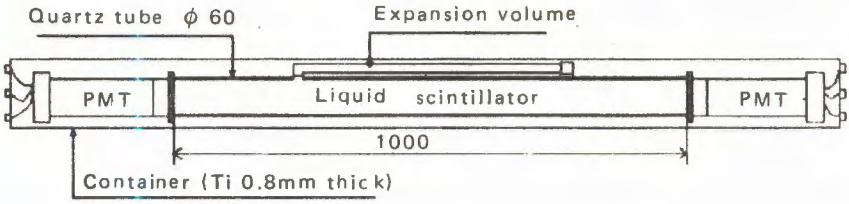

Fig.1. The scheme of position-sensitive neutron detector (PSND)

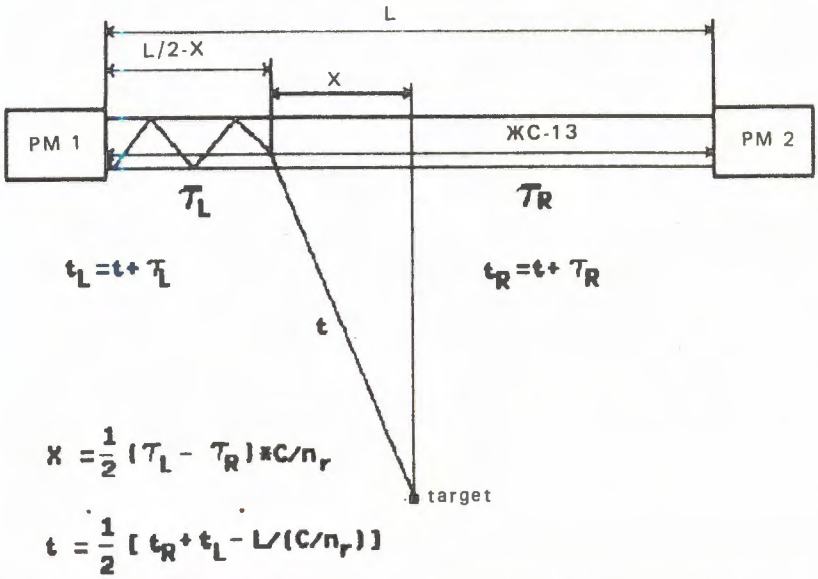

Fig.2. Principle of time and position determination. t — time-of-flight, x — position of an incident neutron, τ_L, τ_R — mean light travelling times, n_r — refractive index of liquid scintillator

time-of-flight, l — the length of detector (1m), τ_L and τ_R — mean light travelling times. The energy of a neutron is calculated by the time-of-flight method.

In figure 3 there is shown the electronic set-up for measurement of detector properties with the ^{252}Cf source and γ-source. The electronic set-up includes two constant fraction discriminators (CFD) and two time-to-pulse-height converters (TAC) for measurements of the times of flight and the difference light travelling times in the scintillator, two fast commutators for

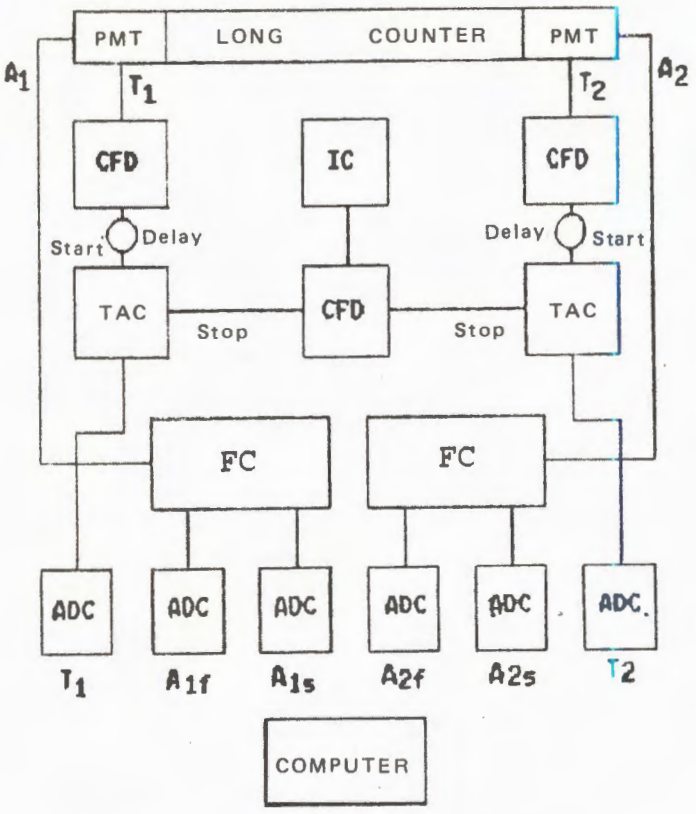

Fig.3. Electronic set-up for testing PSND. PMT — photomultiplier, CFD — constant fraction discriminator, TAC — time-to-pulse-height converter, FC — fast commutator, IC — ionization chamber, ADC — analog-to-digital converter

division of the PMs signal by fast (with time 50 ns) and slow (with time of 300 ns) components and block of coincidence and strobes. Six ADCs (analog-to-digital converters) are connected by the IBM COMPUTER. Ionization chamber with ^{252}Cf source and constant fraction discriminator forms the «stop» signal for the time-of-flight measurements.

In figure 4 there is shown necessary data for obtaining energy and angular information from position-sensitive neutron detector:

1. Half of a sum of times gives us the time-of-flight.

2. Difference of times gives us a position of an incident neutron. Time-of-flight and position give us neutron energy.

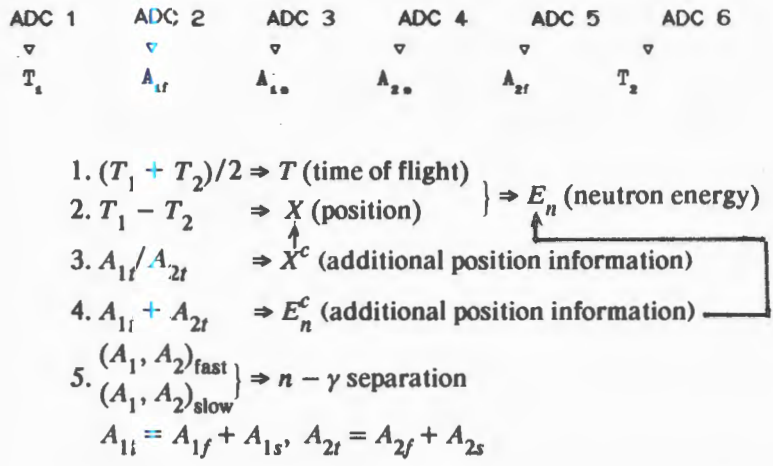

Fig.4. Necessary data for obtaining the energy and angular information from PSND

3. The ratio between the pulse heights of fast signals gives us additional position information.

4. Sum of the pulse heights defines the recoil energy of proton and also gives us additional information on neutron energy.

5. The relation between two fast and slow components of PM charge signal allows one to realize n-γ separation.

Therefore the data from position-sensitive neutron detector include six values and occupy 12 bytes of memory. For the system of neutron detectors we must add yet one byte in order to remember the number of neutron detectors.

In figure 5 there is shown the electronic set-up for serving of two (or more) PSNDs. This scheme explains the logic of work in the case of a few PSND, where the multi-input CDC (charge-to-digital converter 4300B «Le Croy») and the multi-input TDC (time-to-digital converter 4300B+4303 «Le Croy») are used.

3. Calculation Methods

The efficiencies of our set-up irradiated by neutrons with the energies less than 20 MeV and neutrons cross talk have been calculated by the program package SITHA (Simulation Transport Hadron) [7]. This package

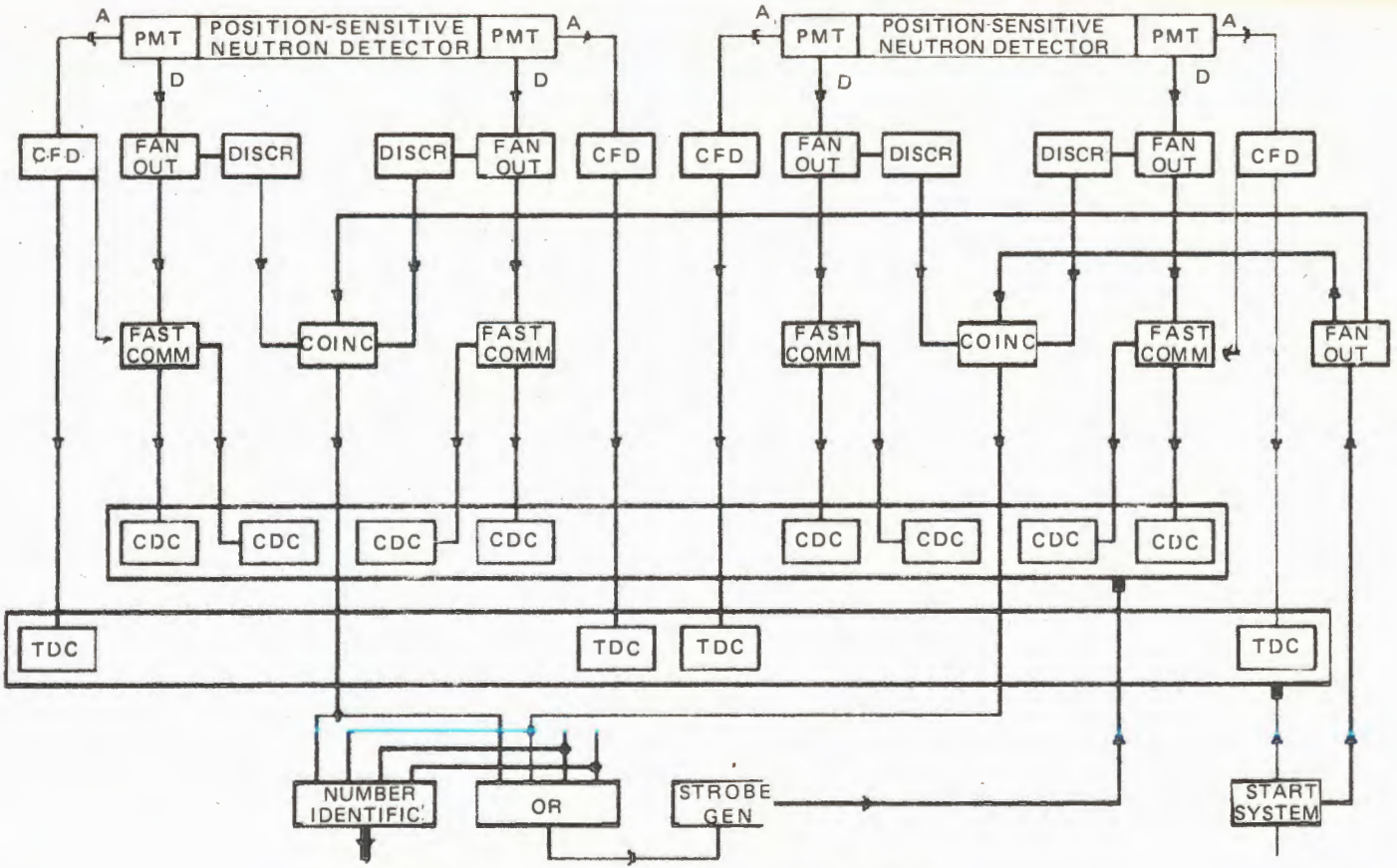

Fig.5. Block-scheme of electronics for serving of two (or more) PSNDs

was created in Radium Institute and its development goes on last years [8]. The package SITHA is used to calculate hadron transport in matter blocks of a complex geometry.

The nucleon and pion transport was carried out for the energy interval from 10 MeV to 10 GeV; and neutron transport, for the energies less than 20 MeV. In the last case multigroup approaches based on the neutron cross section library GR175-V1 [8] are used. The package SITHA includes different modules for calculation of the response function of the neutron detectors based on liquid organic scintillator irradiated by the neutrons with the energies less than 20 MeV. These modules have been carefully tested [9] and we use them for calculations of the characteristics of our long position-sensitive neutron detector.

Light output to protons, alpha particles and recoil nuclei were taken from Dekempeneer et al. [10]. Light attenuation in the long tubes has been taken into account.

4. Results and Discussion

The position resolution is presented in fig.6. The highly collimated ^{252}Cf source was displaced in steps of 10 cm in front of the detector. In the upper part of the figure the difference time (ΔT) between both the ends of the detector is shown. This value (14 ns) is equal to double mean light travelling time along the whole length of the detector. The position resolution depends on the time resolution of the detector. The time resolution has been optimized by the choice of voltage between cathode and the focusing electrodes of PM. The time resolution of the whole detector system including electronics is 1.4 ns. Therefore the position resolution is 10 cm. In the lower part of the figure one can see the position resolution as a function of the neutron energy loss in the scintillator. The energy scale was obtained by means of calibrating of γ-sources and ^{252}Cf source. In the lower energy region the position resolution is mainly determined by the signal-to-noise ratio. This poor resolution may be improved, however, using additional information on the time-amplitude rejection and on the ratio between the pulse height of signals from both PMs.

In fig.7 there is shown the light output versus the position on the detector. The lines are drawn via measured values. For a single PM the pulse height vares three times, but the sum of light output is nearly constant (20%) along the scintillator. The light output variation from single PM may be used for an additional position information. The sum of light output from

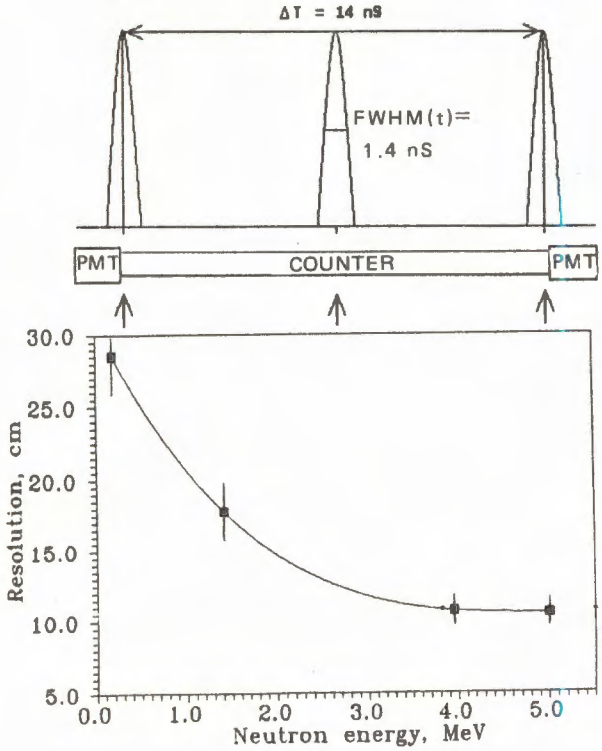

Fig.6. Upper part: the illustration of position resolution. Lower part: position resolution vs. neutron energy loss in the scintillator

both PMs gives an additional energy information which is almost independent of the position.

In figure 8 there is given the time-of-flight spectrum of PSND sector (x = 20—30 cm — position of detector relative to its end) for 0.5 m flight path as measured with a ^{252}Cf source. The quality of the time-of-flight separation between neutrons and γ is demonstrated in this figure. For n-γ pulse-shape discrimination we use the digital integration method: comparison of fast and slow components of PM signal. The combination of the time-of-flight and pulse-shape methodics enables a good n-γ discrimination for neutron energy threshold of 1 MeV.

The absolute neutron efficiency has been measured by means of ^{252}Cf source. The source was displaced at a distance of either 0.5 or 1 m from the

Fig.7. Light output vs.position. □ — photomultiplier 1, ■ — photomultiplier 2, ★ — sum of PM1 and PM2

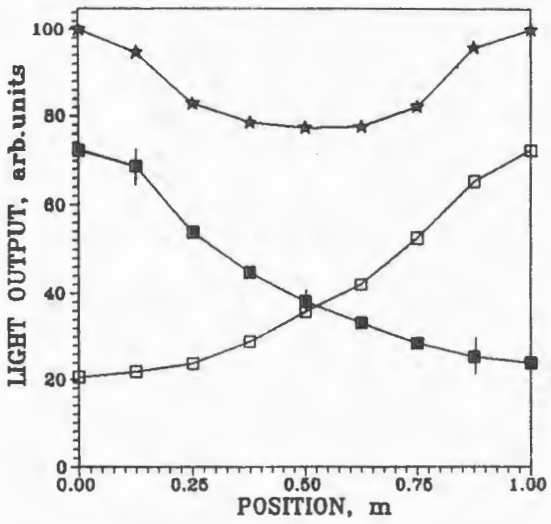

Fig.8. Time-of-flight spectrum for 0.5 m flight path (^{252}Cf). L — path of flight in the middle of detector, x — position of detector relative to its end

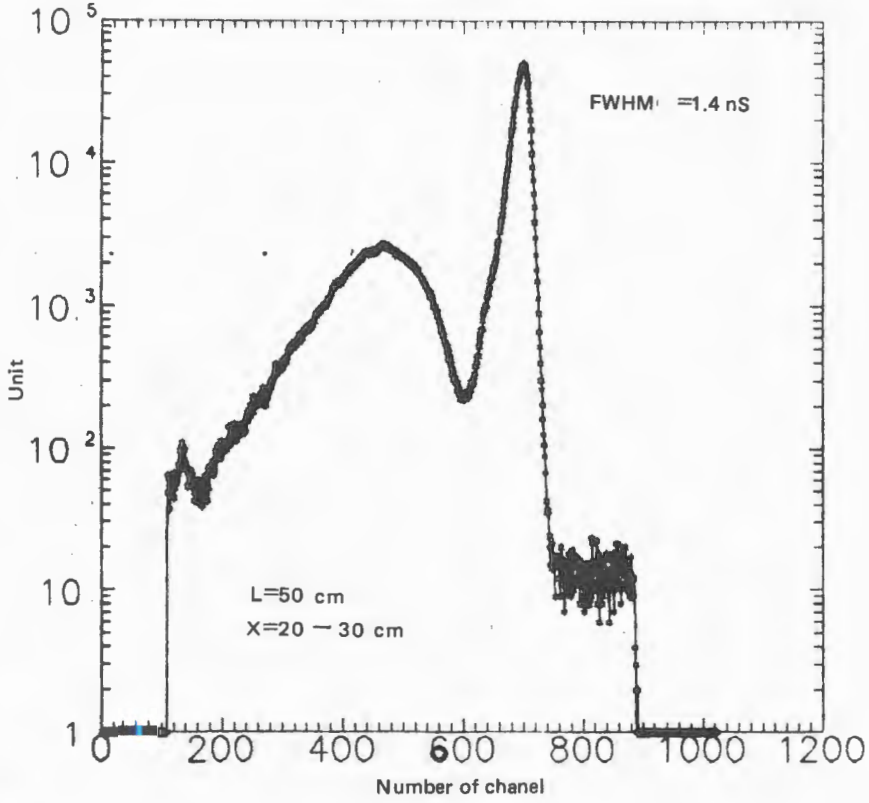

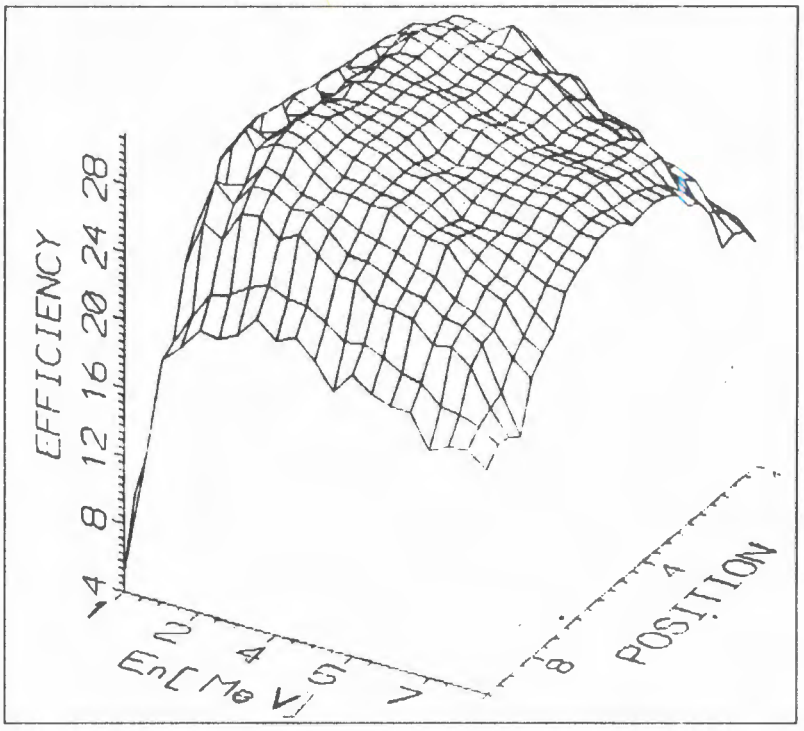

Fig.9. The measured neutron efficiency of PSND as a function of neutron energy and position of detector

center of a detector. The measurements have been made for energy threshold — 1 MeV recoil proton energy in the middle of detector. Ten positioned time-of-flight spectra for various time intervals between signals from PMs have been collected simultaneously. The neutron efficiency registration for different detector sectors (position) as a function of neutron energy has been obtained from neutrons number ratio detected in coincidence with fission fragments and total neutrons number emitted in solid angle of the given detector sector. In figure 9 there is presented the isometric plot of efficiency as a function of neutron energy and position of neutron detector for neutron energy threshold of 1 MeV. This efficiency has been also calculated by code SITHA for the same geometry and different energy threshold of neutron registration. In figure 10 there is shown the comparison between measured neutron efficiency and calculated one for 2 and 7 MeV neutron energy. The calculated and measured values of

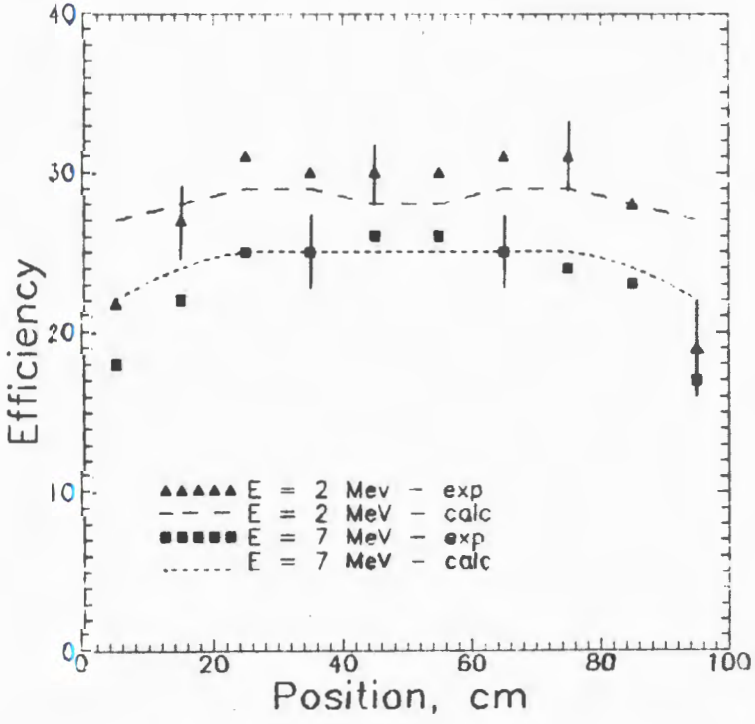

Fig.10. Comparison between measured neutron efficiency and calculated one by SITHA code values (curves) for 2 and 7 MeV neutron energy

efficiency are in good agreement. The efficiency is nearly independent of the position in the region of 80 cm. Therefore the detector may be used over an effective length of 80 cm (± 40 cm regarding the middle of detector). PSND has been tested on measurements of neutron emission from heavy-ion reactions on DEMAS-N set-up of the U-400 accelerator, LNR (JINR, Dubna). ^{20}Ne beam with energy of 144 MeV and current of 100 nA bombarded ^{197}Au target of 200 $\mu g/cm^2$ thickness. Neutron detector was placed parallel to the beam axis at a distance of 0.5 m. Counting rate from each PM was 10^5 per second. The neutrons were detected in coincidence with fragments. The avalanche fragment counter was used for «start» at measuring the energetic neutron spectrum by the time-of-flight method. The time resolution was 1.6 ns; the position resolution, 10 cm, at energy threshold of 1 MeV.

5. Conclusion

The test measurements on ^{252}Cf source, γ-sources and heavy-ion beam have shown that PSND can be used for investigation of the angular distribution and energy spectrum of neutron low energy range (0.5—10 MeV). This detector can also be used as a module of multidetector near 4π solid angle system which allows one to measure simultaneously multiplicity, the angular and energy distribution of neutrons with high efficiency. PSND can be used for construction of «neutron wall» which includes a few (5—10) layers of PSND for measurements in the large solid angle with high efficiency of high-energy neutrons (up to 500 MeV). However, in case of using PSND as a module of multidetector closely packed system there is a «cross talk» effect (this occurs when a detected neutron is scattered by a neighbouring detector). In accordance with investigation of this effect by Desesquelles et al. [11] with the multidetector AMPHORA, the main consequences of the «cross talk» are: an enhancement of the measured multiplicity and a smoothing of the laboratory angular distribution.

We calculated the values of the «cross talk» for various geometry configurations of some position-sensitive neutron detectors by means of simulation using the SITHA code. We began test measurements of this effect using two PSNDs. The preliminary results show that in case when two PSND were placed close to each other (the distance between axes of detector was 12 cm) only 5% of detected neutrons were due to the «cross talk» for neutron energy threshold of 1 MeV of spontaneous fission spectrum of neutrons. Taking into account the importance of distortions connected with the «cross talk» effect we are going to publish experimental and calculated results of this effect in the next article.

We thank Prof. Yu.Oganessian for permanent interest and large support of this work, colleagues S.Voronin and A.Veschikov for help in creation of neutron detector, V.Salamatin, A.Tonchev, G.Chubarian and the team of the U-400 accelerator for assistance in testing PSND on heavy-ion beam at LNR, Dubna.

Reference

1. Nuclear Physics News, 1991, vol.1, no.5, p.15.
2. Hourani E. et al. — Nucl. Inst. and Meth., 1976, v.134, p.513.
3. Netter P. et al. — Nucl. Inst. and Meth., 1981, v.185, p.165.
4. Qi H.Q. et al. — Comm. INDC(CPR)-005/G. 1985, p.1—7.

5. Alkhazov I.D. et al. — In: Scientific Report LNR, JINR 1989—1990 «Heavy Ion Physics», Dubna, 1991, E7-91-75, Dubna, p.182.
6. Afanasiadi L.Sh. et al. — Sov. Jour. «Pribory i Tekhnika». 1986, v.6, p.58.
7. Daniel A.V. — Preprint R1-181, Moscow, 1984.
8. Daniel A.V., Perov V.Yu., Sokol E.A. — JINR Comm. P3-91-320, Dubna, 1991.
9. Daniel A.V., Kozulin E.M., Kuznetsov A.V. — JINR Comm. (to be published), Dubna, 1992.
10. Dekempeneer E. et al. — Nucl. Inst. and Meth., 1987, v. A256, p.489.
11. Desesquelles P. et al. — Nucl. Inst. and Meth., 1991, v.A307, p.366.

Received on October 29, 1992.